

Materials Science inc. Nanomaterials & Polymers

Microspheres/Custard-Apples Copper (II) Chelate Polymer: Characterization, Docking, Antioxidant and Antibacterial Assay

Reena Bagade,^[a] Ratiram Gomaji Chaudhary,^{*[b]} Ajay Potbhare,^[b] Aniruddha Mondal,^[c] Martin Desimone,^[d] Kanhaiya Dadure,^[e] Raghvendra Mishra,^[f] and Harjeet Juneja^[a]

In the present study we have reported fabrication and structural determination of 3D microspheres/custard-apples shaped mesoporous Cu^{II} chelate polymer (CP) from a 1D chelating ligand for enhanced an antioxidant and antibacterial activities. The CP was fabricated from a novel chelating ligand suberoyl bis(2-ethoxybenzamide) (*sbebz*) with copper salt by condensation, while *sbebz* was synthesized from 2-ethoxybenzamide and suberoyl chloride, and was structurally authenticated by ¹HNMR, ¹³CNMR, FT-IR, Mass spectroscopy, XRD, and SEM. As-fabricated CP was characterized by XRD, FT-IR, EDS, UV-DRS, XPS, Raman, SEM, TEM, AFM, BET, and TG for authentication of its structure, shape, size, chemical state, composition, purity, surface behavior, porosity, and thermal stability. SEM revealed nearly monodispersity in microspheres,

while TEM rendered average particles sizes of 10–47 nm. AFM supported nearly homogenized nature of microspheres, while BET rendered a mesoporosity. Further, antioxidant property of CP was examined by using α , α -diphenyl- β -picrylhydrazyl (DPPH) in ethanolic/methanolic solvents, while ascorbic acid was used as a standard medium. Furthermore, the antibacterial activity of both materials was tested against human pathogenic bacteria viz. gram +Ve (*Staphylococcus aureus*, and *Bacillus subtilis*), and gram -Ve (*Escherichia coli* and *Klebsiella pneumoniae*). Moreover, molecular docking of *sbebz* was performed using both genetic (GA) and non-genetic (Non-GA) algorithm techniques, where result demonstrated an excellent docking energy.

Introduction

In recent years, the construction of supramolecular, scaffold, and nano-micro structured coordination polymers is an eye-catching research in the field of coordination chemistry.^[1] The coordination polymers of transition metals (Ag, Au, Pt, Rh, Cu, Fe, Ni, Zr, Co and so forth) with different coordinating agents have increased a considerable interest in the field of catalysis, biological appliances and electrochemical sciences because of

inherent and intriguing architecture, and interlinking phenomena.^[2] Particularly, a chelating based coordination polymer is a thrilling topic due to its high thermal stability, beautiful artistic, spectacular geometry, captivating functional property, supramolecular and heterocyclic ring possession.^[3] A heterocyclic ring possessing compound commonly called as chelate polymer or coordination polymer (CP). Basically, chelate polymer is a new class of material which is architected by a metal connected with multidented chelating ligand in a prolonged network with diverse dimensionality.^[4] An enhanced thermal stability along with mechanical property of CPs is because of its architectural and heterocyclic ring formation.^[5] One of the most thermally stable compounds in the branch of coordination chemistry is chelate polymer compound due to its chelation and heterocyclic ring.^[6] Owing an excellent scaffold structure, thermo-kinetics, optical, biological, and marvelous morphological properties of CPs may be due to the presence of "O" and "N" as prime donor sites.^[7] Basically, an organic ligand with different donor sites are playing a key role in the formation of multiple type of morphologies such as 0D, 1D, 2D & 3D.^[8] Besides this factor, solvent, concentration and temperatures are also playing a key role in assembling the corresponding CP. In this regard, different research groups have paid valuable contribution towards the fabrication of multi-nano-porous dimensional nano-micro structured CPs in the high temperature with using mix-solvents (DMF-CH₂Cl₂, MeCN-CH₂Cl₂, and MeOH-CH₂Cl₂). Still now, hydrothermal method is a

[a] R. Bagade, Prof. H. Juneja

Post Graduate Teaching Department of Chemistry, Rashtrasant Tukdoji Maharaj Nagpur University, Nagpur-440033, India

[b] Prof. R. G. Chaudhary, A. Potbhare

Post Graduate Department of Chemistry, S. K. Porwal College, Kamptee-441001, India

E-mail: chaudhary_rati@yahoo.com

[c] Dr. A. Mondal

CSIR-Central Salt and Marine Chemical Research Institute, Bhavnagar-364002, India

[d] Prof. M. Desimone

Universidad de Buenos Aires, Consejo Nacional de Investigaciones Científicas y Técnicas (CONICET), Instituto de la Química y Metabolismo del Fármaco (IQUIMEFA), Facultad de Farmacia y Bioquímica, Junin 956 Piso 3, (1113) Ciudad Autónoma de Buenos Aires, Argentina

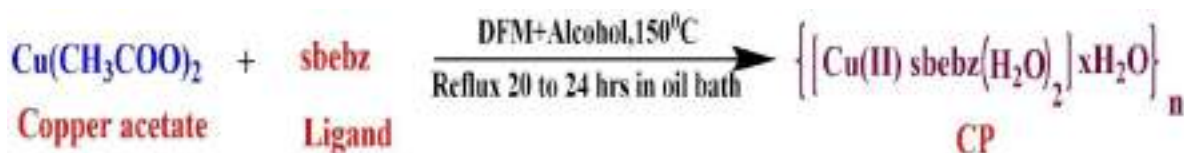
[e] Prof. K. Dadure

Post Graduate Department of Chemistry, J. B. Science College, Wardha-442001, India

[f] R. Mishra

International Inter-University Center for Nanoscience and Nanotechnology, Mahatma University, Kottayam-686560, India

Supporting information for this article is available on the WWW under <https://doi.org/10.1002/slct.201901115>



Scheme 1. The reaction route for fabrication of nanostructured Cu^{II} CP

very effective method for the fabrication of multi-dimensional nano-microscale mesoporous coordination materials.^[9]

Consequently, for fabrication of highly objective, nanoporous, nano-micro structured, scaffold shaped or wanted materials along with good selectivity is an existent task in the field of metal based CP. So far, multiple and huge efforts have been made to construct and fabricate the CP of selective metal/ligand and this is very essential aspect for functional appliances as it is an endogenous oxidative DNA damages, anti-cancerous, anti-bacterial, cell skin destructions and so forth. In general, metal ions acting as the essential elements for cells may become toxic materials at high concentrations. During last few years, antibacterial, anti-cancerous, and antioxidant study of metal organic framework (MOF) and CPs were studied extensively.^[10] Indeed, countless organic ligands having "N" and "O" as a donor centers were fabricated for the development of MOF and CPs. Keeping this issue, we have fabricated a novel biologically active chelating ligand (*sbebz*) having "N" and "O" as a donor sites, and its microstructured mesoporous CP with transition metal *i.e.* copper.

In the present work, we have fabricated Cu^{II} CP with novel chelating ligand (*sbebz*). As-fabricated CP was initially characterized by various electron spectroscopy techniques to find out its structure, shape, size, chemical state, surface behavior, porosity and thermal stability. After structural authentication of CP, it was tested effectively against gram-positive/gram-negative pathogens, and antioxidant property. Moreover, we have investigated a molecular docking study of novel ligand. To the best of our knowledge, the molecular docking study of fabricated ligand is reported here for the first time.

Results and Discussion

Structural authentication of ligand

A novel chelating ligand (*sbebz*) was synthesized from 2-ethoxybenzamide and suberoyl chloride for the first time in our laboratory by following earlier scheme.^[11] The synthetic procedure has been given in S1 in the supporting information. A starting material 2-ethoxybenzamide was a novel moiety in the present work. Therefore, as-synthesized *sbebz* was fully characterized by using various spectroscopic techniques to authenticate its molecular structure and size. The physicochemical and analytical data of *sbebz* is given in S7 in the supporting information. Initially, a moiety (*sbebz*) was analyzed by the ESI mass spectrum. In the ESI mass spectrum (see Supporting Information S8) of *sbebz*, the molecular ion peak (M⁺) was found to be at M/Z 468 amu, which corresponds to molecular

weight (MW) of *sbebz*. A (M+Na) molecular ion peak m/z = 491. Then, ¹H NMR of *sbebz* (see Supporting Information S9) exhibited corresponding signals δ at 1.42, 3.09, 3.45, 4.19, 7.01, 7.07, 7.32, 7.45 ppm. δ 1.42(t,3H,CH₃), δ 3.09(q,1H,CH), δ 1.27(t,2H CH₂), δ 3.45(s,1H-NH), 4.19(q,2H,-CH₂), δ 7.01(t,1H,-CH(Ar)), δ 7.07(d,1H,-CH(Ar)) and 7.45(t, 1H) J = 7.32 Hz. Also, ¹³C NMR signals of *sbebz* (see Supporting Information S10) exhibited at 79.13, 78.80, 78.47 ppm confirmed -CH₂ group of aliphatic chain. The resonance signals obtained at 132.49, 131.06, 121.99, 120.28, 121.57 ppm assigned to carbon skeleton of aromatic ring. The signals at 166.25 and 156.59 ppm confirmed the presence of carbonyl carbon of *sbebz*.

Structural determination of Cu^{II} CP

A new microstructured Cu^{II} CP with *sbebz* was fabricated according to our previously reported method.^[11] The details procedure, measurements and physicochemical data are given in S2, S6 and S7 in the Supporting Information respectively (Scheme 1). The structural authentication of CP was examined by using standard electron spectroscopy. Initially, it was characterized by FT-IR spectroscopy to confirm chemical groups (Figure 1b). In FT-IR, spectrum functional groups shifted from *sbebz* to CP with some characteristics frequencies. As well as the numbers of peaks in CP reduced as compare to *sbebz*. The band at 2975.16 cm⁻¹ assigned to N-H frequency (*sbebz*) (see Supporting Information S11) was shifted to 3335.64 cm⁻¹ and 3297.54 cm⁻¹ in CP due to N-H and -OH groups merging, and emerging new broad band, indicating the presence of a lattice water.^[11] The presence of -CH₃ group was confirmed by bands at 2942 and 2737 cm⁻¹ in *sbebz* and CP too,^[10] while band at 1420.62 cm⁻¹ (*sbebz*) due to -CH₂ bending mode, and also found in CP too which were 1413.48 cm⁻¹. The strong bands at 1553 and 1531 cm⁻¹, and weak band at 1636 cm⁻¹, 1692 cm⁻¹ due to C=N stretching mode in *sbebz*,^[12] which clearly disappeared in CP and new strong bands appeared at 1556 cm⁻¹, 1656 and 1717 cm⁻¹ due to transformation and enolization as a C=O group for covalent linkage.^[13] Moreover, a new band appeared at 818.5 cm⁻¹ in CP due to rocking-wagging bending vibrations that attributed to presence of coordinated water molecules. Finally, a broad band appeared at 637.21 cm⁻¹ in CP which is totally different from ligand's spectrum which suggested coordination mode of Cu^{II} ion with oxygen of >C=O group (M-O).

Further, to discern the microstructure and crystallite nature of fabricated CP, XRD was helpful to investigate the pattern (Figure 1a). The diffraction pattern was calculated using Bragg equation $2d\sin\theta = n\lambda$. Figure 1a of *sbebz* clearly shows semi-

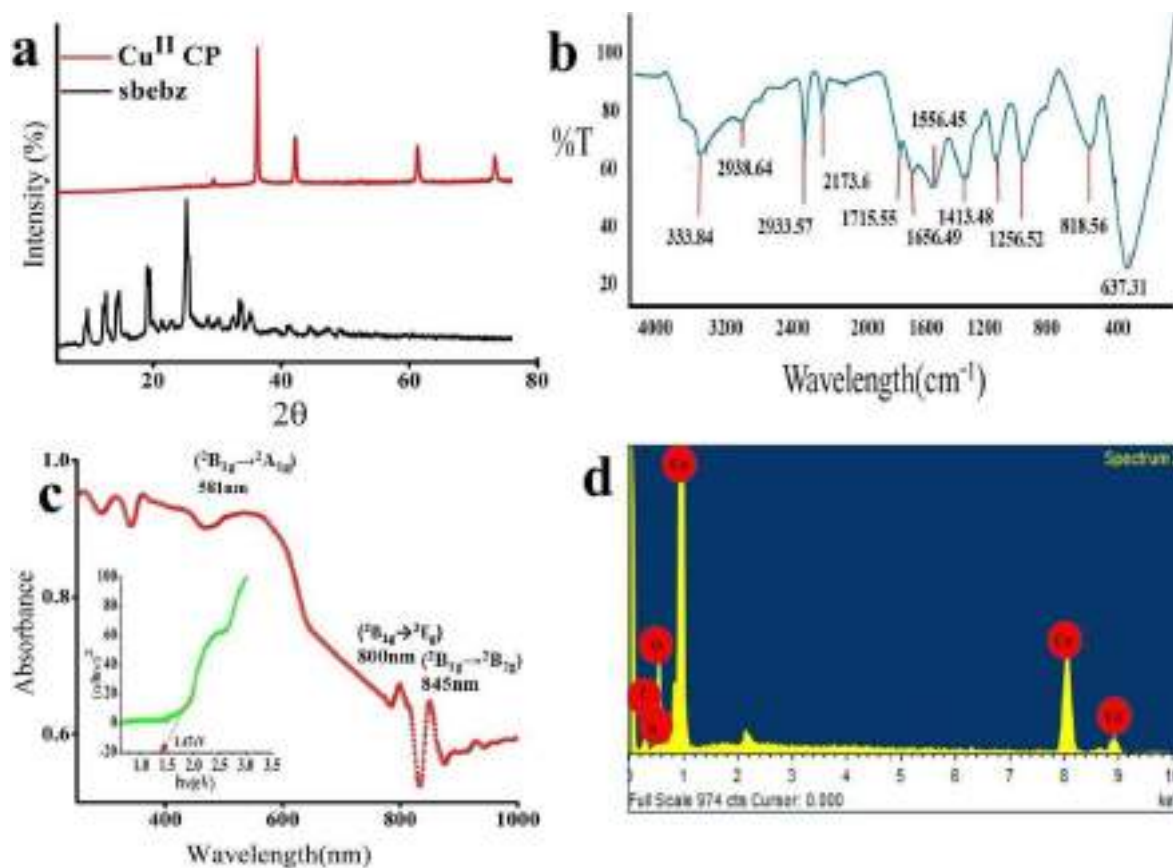


Figure 1. (a) XRD, (b) Raman, (c) DRS/band gap energy, and (d) EDS spectra of Cu^{II} CP

crystalline nature. But, after doping with copper ion it showed sharp diffraction pattern indicating highly crystalline or polycrystalline nature of material. The crystallite size of CP was calculated about 30 nm by using Debye-Scherrer equation. Then, Raman spectroscopy was employed for further structural assessment of Cu^{II} CP. The corresponding spectrum is shown in figure S12 in the Supporting Information. The characteristic peaks were found properly, bond linked to -CH₃ appeared at 2911.42 cm⁻¹ and 1444.60 cm⁻¹ band corresponds to -CH₂ group. The more intense band showed at 1175.17 cm⁻¹ was referred to as C–O stretching bond, and appearing as doublet in spectra. The strong band at 637.95 cm⁻¹ was attributed to the vibration of Cu–O mode. Peak at 1548.92 cm⁻¹ due to the presence of C=N stretching frequency, however, band at 1650.54 cm⁻¹ confirmed the C=O bonding mode. Most importantly, 842.05 cm⁻¹ which may correspond to rocking-wagging bending vibration due to coordinated H₂O molecule.^[14] Further, geometry of CP was examined by diffuse reflectance spectroscopy (Figure 1c). The electronic spectra of Cu^{II} CP shows three absorption bands at 11,834 cm⁻¹ (845 nm), 12,500 cm⁻¹ (800 nm) and 17,211 cm⁻¹ (581 nm) which could be assigned to ²B_{1g} → ²B_{2g}, ²B_{1g} → ²E_g, and ²B_{1g} → ²A_{1g} transitions, and which were in good agreement for an octahedral geometry.^[15] Besides, magnetic moment of Cu^{II} was found around 1.83 BM which favors a six coordinated geometry with high spin

distorted an octahedral geometry.^[15a] The band gap energy of CP was calculated by K–M plot, and it was found to be 1.47 eV, hence study recommended as-fabricated material could be a good photocatalytic agent (Figure 1c). Moreover, presence of elements in material were confirmed by EDS technique (Figure 1d), an elemental analysis atomic percent of Cu was found to be 21.12%, C- 51.97%, H-5.30, and N-4.43% close to the theoretical values (Cu-21.35%, C- 52.54%, H-5.37, and N-4.70%).

Prominently, XPS investigation was done to ensure the chemical composition and its analogous oxidation state, and result has been shown in Figure 2a,b,c,d. This is a highly expensive technique but crucial for examine the chemical state absolutely by displaying satellite peaks. The XPS survey spectrum of Cu^{II} CP is given in the figure S13 in the Supporting Information. Nonetheless, survey spectrum of each element is elaborated in details. Achieved results of CP were good promised with recent literature report. The Cu 2p peaks were observed at 932 and 954 eV attributed to Cu 2p_{3/2} and Cu 2p_{1/2} (Figure 2a). Two discrete centered strong satellite peaks were observed at 943.2 and 963.33 eV which correspond to Cu 2p_{3/2} and Cu 2p_{1/2} spin-orbit components that suggested 2⁺ state of copper. Because cuprous does not show strong satellite peaks at 943.2 eV and 963.33 eV. Undoubtedly, XPS confirmed the electronic state of Cu in CP is 2⁺ (Figure 2a). Next, the binding energy of the C1s carbon was observed around 285 eV

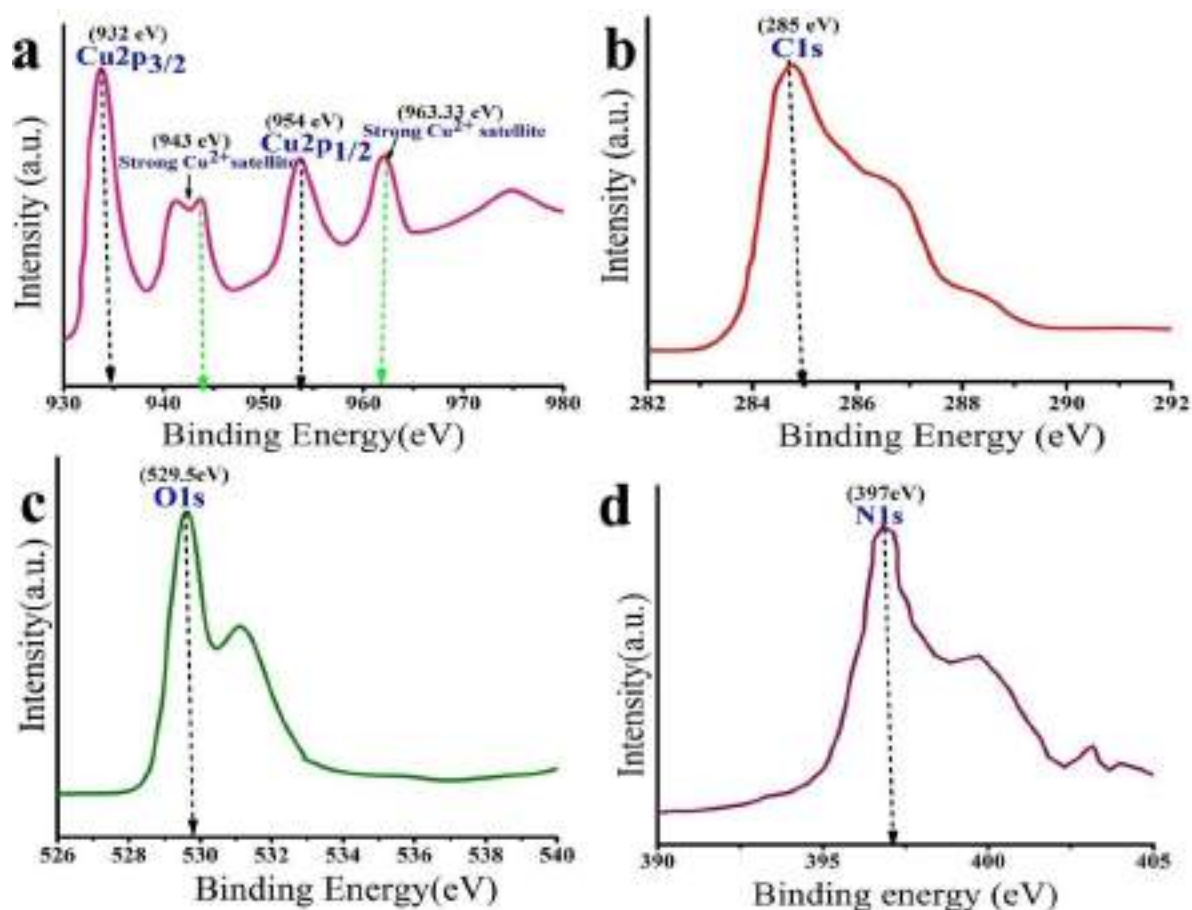


Figure 2. XPS spectra of CuII CP (a) Cu 2p, (b) C1s, (c) O1s, and (d) N1s

(Figure 2b), and peak with binding energy at 397 eV corresponds to Nitrogen (Figure 2d). Peak of O1s is observed at 529.5 eV binding energy confirming the presence of O^{2-} (Figure 2c). Indisputably, XPS confirmed the electronic state of Cu in fabricated material is 2^+ . Hence, this technique recommended a black color microspheres were in a cupric form (2^+), despite red color cuprous (1^+).

After that, *sbez* (Figure 3a), and CP (Figure 3b) were examined by comparative TG analysis (45–900 °C) at different

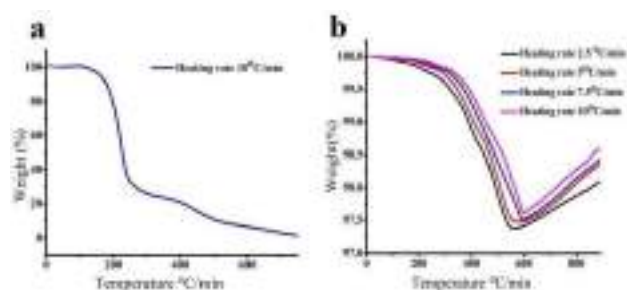


Figure 3. TG curves of (a) *sbez* and (b) CuII CP

heating rates $\beta = 2.5, 5, 7.5,$ and $10^\circ\text{C min}^{-1}$ under the nitrogen atmosphere. Thermal analysis is a powerful technique, which has proved to be useful in determining the lattice, and coordinated water content in the CP, beside, it is useful to determine the thermal degradation behaviors, structural aspects, and thermal stability. A sigmoid curve of *sbez* demonstrated a standard curve which suggested complete loss of mass (99.99%) in the range 140–750 °C with a single step which indicated a moderate thermal stability (Figure 3a). However, CP degraded in a multiple stages and losses only a fraction of mass (3%) at 595 °C, this suggested excellent thermal stability as compared to *sbez*. From Figure 3b, clearly reveals that an initially mass losses at range 100–200 °C due to the coordinated water molecules, these degradation ranges were good agreements with our earlier reports.^[16,11] Moreover, the presence of hydration of water was supported by infrared and Raman spectroscopy. Next, a gradually mass loss in the range 200–595 °C was due to the removal of small portion of the chelating ligand (3%). After, inspecting the thermographs Figure 3b, it was concluded that the heating rate has a significant influence on the temperature range and shape of thermoanalytical curves. The thermal decomposition curves shifted to higher temperature range when the heating rate was

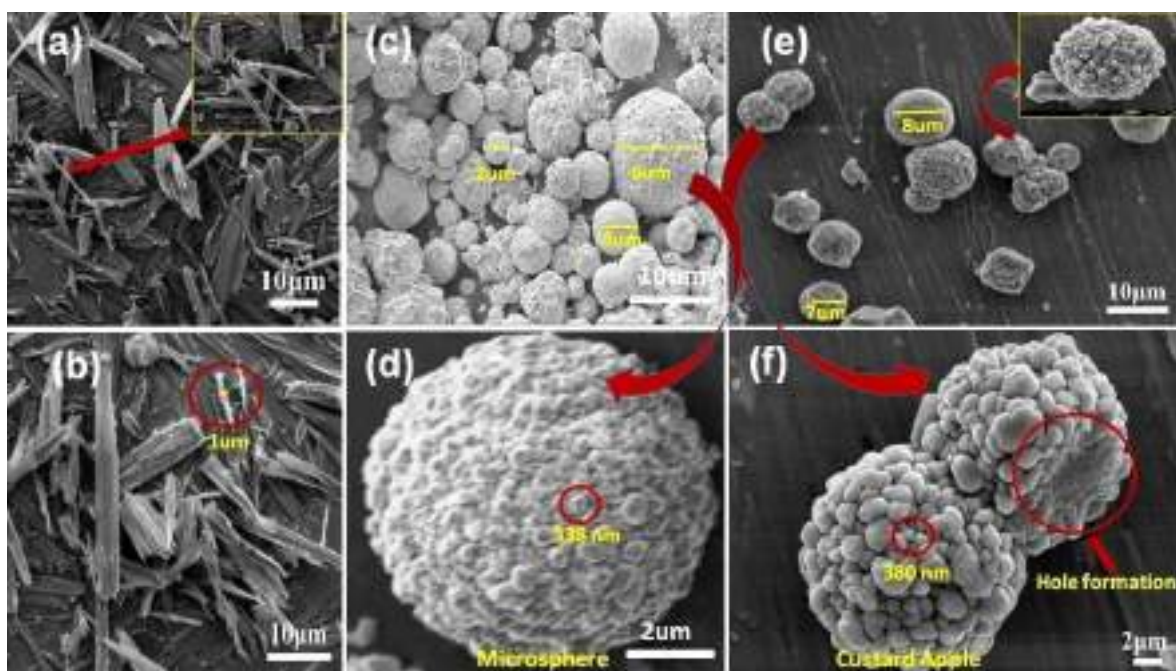


Figure 5. SEM images of (a-b) *sbebz*, (c-d) Microsphere, and (e-f) Custard-shape of Cu^{II} CP

increased. However, mass loss in polymer compounds at every stage does not change strongly in distinct heating rates.

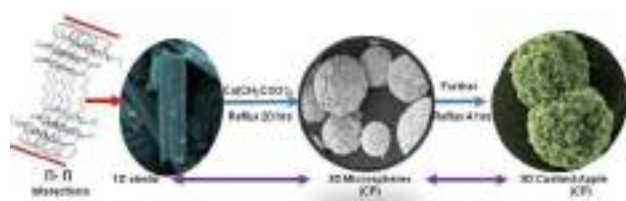


Figure 4. 3D Microsphere/Custard-apple shape formation Cu^{II} CP from the interaction of 1D *sbebz* with Cu^{II} ion

After, 595°C all the curves inflated erectly, it indicated refurbishment of mass of CP, means polymer agglomeration with degraded residue. Hence, it shows abnormal behaviour of CP might be due to the polymeric nature or changing of oxidation state of copper ion. Eventually, study suggested a high thermal stability of CP. A partial degradation of CP at 900°C , recommended CP must have high decomposing temperature.

Microscopy characterization for morphological investigation

A fascinating surface morphology, particle sizes, surface roughness or homogeneity, and porosity of CP was examined by SEM, TEM, AFM and BET respectively. The SEM images of *sbebz* and CP are shown in Figure 5a,b,c,d,e,f. As-synthesized *sbebz*

has uniform and well defined morphological pattern. From the images it is clearly signified that an assembled 1-dimensional (1D) direction, looking like a broken lady's finger or okra shaped (*Hibiscus esculantus*) Figure 5a,b. The 1D nature of *sbebz* supported the coordination pattern. From the molecular images (see docking result), it clearly shows that, the presence of two benzene rings at two corners make it assembling properties due to the presence of pi-pi (π - π) interactions. After, doping of copper ion (Cu^{2+}) with *sbebz* an oxygenated coordination site of the *sbebz* at heating duration about 20 hrs constructed several captivate-scaffold microspheres of Cu^{II} CP (Figure 4), and further, a beautiful 3D custard-apple shaped appeared as the heating duration increases about 4 hrs (Figure 4). EDS of microspheres/custard-apples morphology clearly indicated the presence of Cu, O, C, and N (Figure 1d). Actually, shapes were assembled with coordinate-covalent interaction with *sbebz*. Finally, a macromolecules (microsphere/custard-apple) were appeared due to the interaction of several tiny nanospheres.

Also, SEM images revealed nearly uniformity in spherical shapes of CP, it ought to be called as microspheres having an average diameter of each 2–7 μm , and each microsphere was constituted by several micronanoparticles having diameter 338–400 nm (Figure 5c,d). However, each microcustard-apple shaped have an average diameter of each 7–8 μm constructed by countless micro-/nanoparticles having diameter sizes 380–450 nm (Figure 5e,f). Fortunately, at heating time 24 hrs material was started a hole formation, indeed it is marvellous property of material. Basically, these uniform microspheres were developed from an aggregation of numerous nanoparticles having particles sizes 2–60 nm (Figure 6a,b,c,d). The

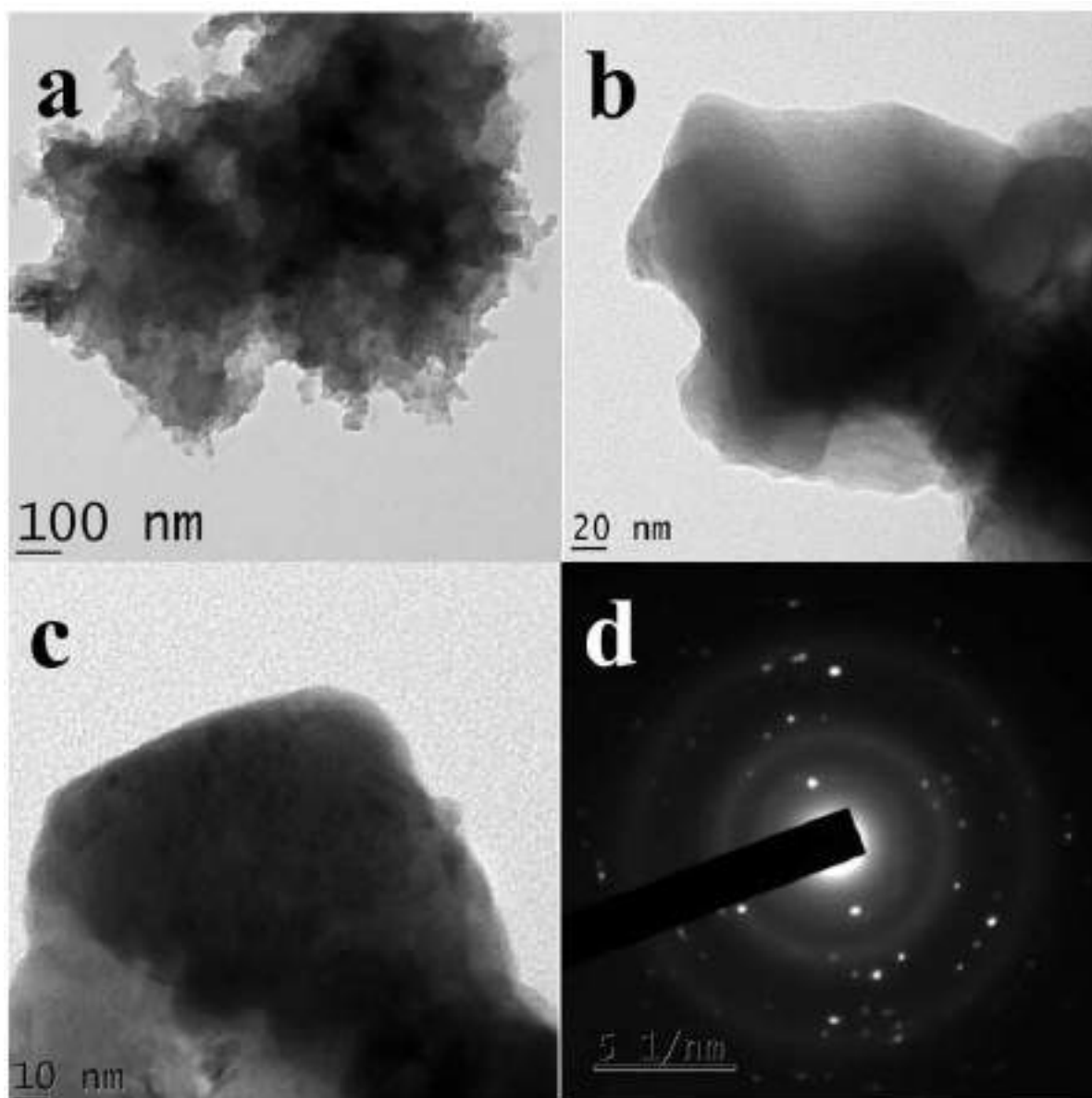


Figure 6. TEM image of Cu^I CP

process of aggregation to spherical morphology also depends on an aging time. With the increase of an aging time, the nearly monodisperse nanoparticles gradually comes into being which might be confirmed by transmission electron microscopy. The microspheres or custard-apple shaped formation might be due to the non-covalent interaction, orientation, and fusion of nanoparticles which lead to agglomeration that serves as crystal seed to grow microspheres.^[17] Most importantly, the development of uniform agglomerated microspheres might be due to homogeneous nucleation with constant and prolonged heating at higher temperature, conventional heating, longer time heating for nucleation might be enough but varied heat-zones led to formation of bigger particles and wider distribution.^[18] Nonetheless, we were succeeded to form a single microsphere of CP with nearly monodispersity. The

uniformity (monodispersity) particularly in shape and sizes of CP were achieved, and it might be due to the constant heating at high temperature. Most significantly, during the material fabrication we took a polydentate ligand which was more powerful chelating agent and sphere forming agent, ultimately, we succeeded to construct a stable uniform single microsphere. Literature survey reveals that the researchers succeeded to develop a single nanosphere.^[19] Fused custard-apple shaped with hole-formation stage was generated after 24 hrs, it was eye-catching result. Because of the hole-formed CP was efficiently active towards antioxidant and antibacterial activity, ultimately, said properties were highly enhanced.

Furthermore, the detail study of particles size investigation was done by TEM analysis. TEM image confirmed that the irregular shaped particles were assembled into each other at

nanometer scale, and which has been shown in Figure 6a,b,c. Figure 6d, the selected area electron diffraction pattern clearly shows semi-polycrystalline in nature. In background, few light circles (Figure 6d) were observed due to the polymeric nature of material. It was gambled due to supramolecular structure of the compound or the packing structure on molecular level might have influenced the morphology of nanostructured compound.^[20,19] Next, the specific surface area and pore size distribution of CP were characterized by using N₂ adsorption-desorption isotherm at low relative pressure ($p/p_0 \leq 0.1$) (Figure 7). The isotherm was shown a drastic uptake at very low P/

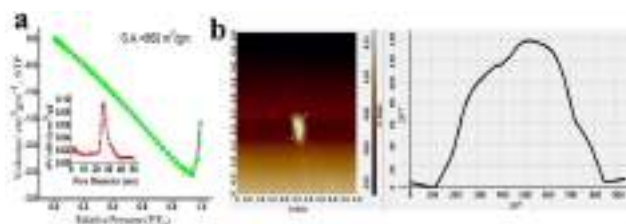


Figure 7. (a) BET and (b) AFM images of Cu^{II} CP

P_0 , indicating presence of mesoporous. The nature of the surface areas was found to be type IV. Specific surface areas and pore volumes were calculated by BET and t-plot method. The surface area of CP was found to be 860 m²/gm, while the pore size demonstrated about 29 nm hence, from the pore size distribution curve divulged the mesoporous nature of material.^[21] The surface roughness and particles behaviors of CP were examined by AFM (Figure 7b). AFM profile revealed an almost identical shape and sizes of CP *i.e.* nearly monodisperse in nature. Finally, on the basis of FT-IR, XRD, Raman, DRS, EDS, XPS, TG, SEM, TEM, AFM and BET techniques a fabricated microstructured Cu^{II} CP suggested microspheres/custard-apples shapes with mesoporous in nature and an octahedral geometry (Figure 8).

Molecular docking

In the present work we have performed docking study of a chelating ligand (*sbez*) due to an excellent physicochemical property of *sbez* (Table 1). However, we also tried for molecular docking study of CP but it was not fitted in statistical calculation due to its large complex structure.^[22] According to docking investigation, a ligand molecule interacted with receptor site of enzyme (Figure 9a,b,c,d). To perform docking study a protein grid design tools was used with autodock for details see Supporting Information S3. The docking was performed using both *genetic* (GA) and *non-genetic* (Non-GA) algorithm techniques. The genetic algorithm is newly adopted conformational technique that provides very accurate and quality results in very short duration of simulation time.

The controlled parameters were achieved by *sbez* docking with protein PDB ID 4Z3 M^[23] showing docked values and hydrogen-bond information which are listed in Table 2. In the present study we have chosen protein PDB ID 4Z3 M, a

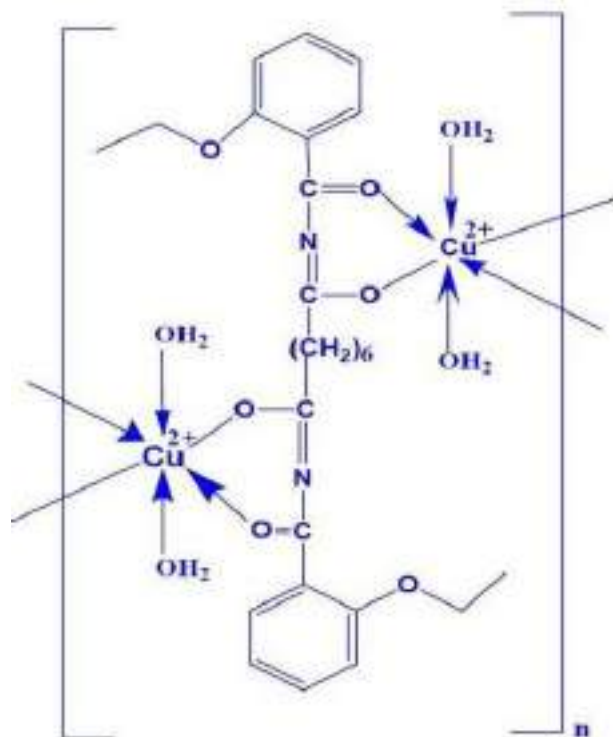


Figure 8. The proposed structure of Cu^{II} CP

Table 1. Physicochemical property of *sbez*

Heat of formation [kcal/mol] at 25 °C	Stretch energy in [kcal/mol]	Torsion energy in [kcal/mol]	Total energy in [eV]	Standard Gibbs free energy [kJ/mol]
-843.13	6.52741	6.16764	-6106.41	-72.72

Table 2. *sbez* docked with PDB ID 4Z3 M showing docked values and hydrogen-bond information

Molecular formula	Docking energy ΔG in [cal/mol]	Number of hydrogen bonding (HB)	Amino acids involved in hydrogen bonding
C ₂₆ H ₃₂ N ₂ O ₆	-6.69852	6	32 ALA, 108 TRP, 55 ILE, 37 ASN, 114 ARG, 33 LYS,

inhibitor 3-[2-chloranyl-2-[dimethyl(oxidanyl)-{4}-sulfanyl]-4-ethylsulfanyl-1-oxa-3{3} thia2{4} platinacyclohexa -3,5-dien-6-yl] having estimated dock energy value about -5.96493 Kcal/mol. Further, this inhibitor was studied using our newly synthesized *sbez* (N¹, N⁸ bis (2-ethoxybenzoyl) octanediamide), and comparatively an enhanced best docking result was obtained, and dock energy was found to be -6.69852 kcal/mol, indeed it was outstanding result, hence it revealed that the material (*sbez*) could be used as a best anticancer and antipathogenic drugs. Therefore, it was also tested as antibacterial agent against the gram-positive as well as gram-negative pathogens, and activity revealed effective results. The occupation of His15 side chains

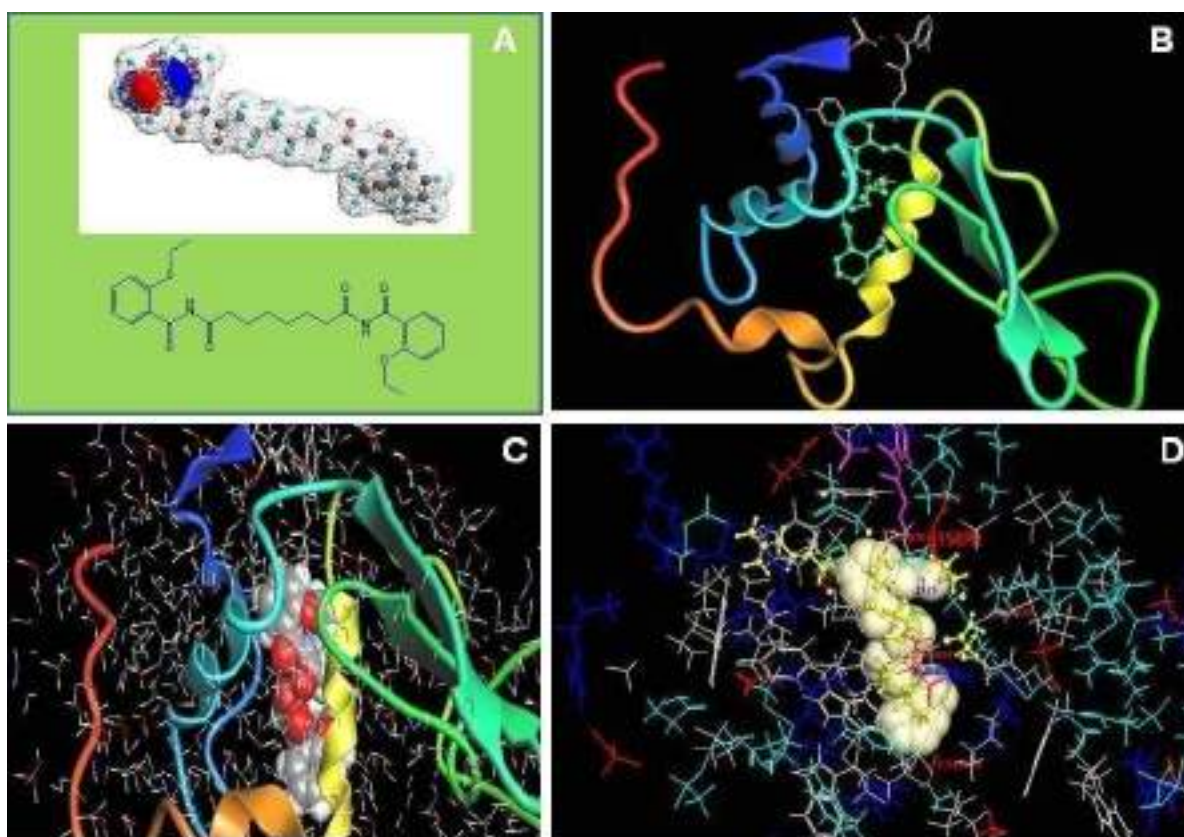


Figure 9. (A) 3-D view of N¹N⁸ bis(2-ethoxybenzoyl) octanamide (*sbez*), (B) Cartoon representation of the protein PDB ID 4Z3 M in the center bind with *sbez*, (C) Cartoon representation of the protein PDB ID 4Z3 M, *sbez* in CPK mode surrounded by water molecules, and (D) *sbez* is in cylinder with CPK mode surrounded by different modes amino acid.

by metallodrug fragments has been observed previously in various structural data,^[24] but also other amino acid side chains were found to be metallodrug involved in metallodrug binding which is mentioned in Table 3.

Table 3. Selected parameters for docking	
Parameter	Value
Grid resolution	0.4
Number of steps	50
The population size	100
Maximum generation	5000
Local search maximum iteration	20
Converged RMSD population fitness	< 1 [kcal./mol]
Grid dimensions	39 x 34 x 54
Total number of grid points	71604

Antibacterial assay

The in-vitro biological activity of *sbez* and Cu^{II} CP was tested against human pathogenic gram-positive bacteria (*S. aureus* and *B. subtilis*) and gram-negative bacteria (*E. coli* and *K. pneumoniae*) by agar well diffusion method by using MH (Molar

and Hinton) nutrient agar as a medium. For the details experimental protocols of antibacterial assay see Supporting Information S4. CP was insoluble in common organic solvents. Therefore, the test solutions were prepared as a CP suspension by dissolving in water, and were sonicated for 30 min to give dispersive suspension. This suspension was further used for an antibacterial assay. The 20 mL of sterile nutrients agar medium was poured into the Petri-plates and overnight grown bacterial cultures were swabbed on agar surfaces. The zone of inhibition was calculated for each tested microorganism after 24 hrs by incubating at 37 °C. Notably, well zone of inhibition was observed in all the tested bacterial strains (Figure 10a,b,c,d). A

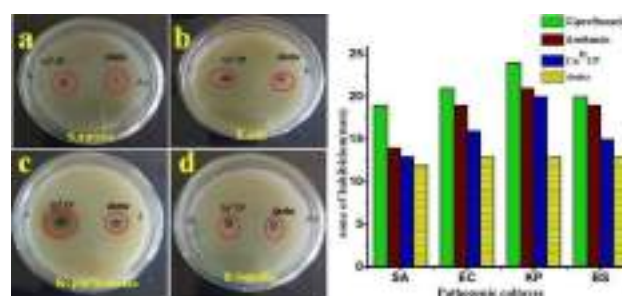


Figure 10. Zone of inhibition of pathogenic culture by *sbez* and Cu^{II} CP

chelating ligand *sbez* showed good antimicrobial activity against gram-negative bacteria (*E. coli* and *K. pneumoniae*) than gram-positive bacteria (*S. aureus* and *B. subtilis*). However, an inhibition zone was enhanced in CP. Perhaps, an enhanced strong inhibition because of reduced sizes of microspheres/custard-apples. A strong inhibition zone was observed by CP for gram-negative pathogens viz. *K. pneumoniae* and *E. coli* (Figure 10b,c). Out of that, a highest zone of inhibition was obtained for *K. pneumoniae*. A comparative result of both materials revealed that at concentration 0.1 mg/50 μ L showed an effective zone of inhibition against *K. pneumoniae* followed by *E. coli*, *S. aureus* and *B. subtilis* (Figure 10). The antibacterial assay was performed in triplicate time (Table 4). An enhanced

Pathogens	Standard Antibiotics (n = 3)		Zone of inhibition (mm) against pathogenic bacteria n = 3	
	<i>Ciprofloxacin</i> (5 μ g/50 μ L)	<i>Amikacin</i> (5 μ g/50 μ L)	Cu ^{II} CP (0.1 mg/50 μ L)	<i>Sbez</i> (0.1 mg/50 μ L)
<i>S. aureus</i>	19 \pm 0.16	14 \pm 0.58	13 \pm 0.57	12 \pm 0.20
<i>E. coli</i>	21 \pm 0.16	19 \pm 0.54	16 \pm 0.28	13 \pm 0.16
<i>K. pneumoniae</i>	24 \pm 0.22	21 \pm 0.27	20 \pm 0.90	13 \pm 0.54
<i>B. subtilis</i>	20 \pm 0.28	19 \pm 0.36	15 \pm 0.35	13 \pm 0.26

n = 3 (No of sample) \pm SD

antibacterial activity of CP might be due to its effectively binding on bacterial cell membrane and that inhibited the active transport ions process which ultimately causes cell lysis. The lysis of cell because of nanospheres particles (microspheres/

custard-apples) penetrated inside the bacteria that could damage organelles by interacting with DNA.^[25] Consequently, DNA lost its replication and proteins synthesis. Basically, nanospheres of CP released subsequently may bind to DNA and lead to disordering of helical structure by cross-linking within and between nucleic acid strands (Figure 10). Finally, inside the bacterial cells the CP nanoparticles disrupt biochemical processes (Figure 11).

In the present effort, the materials were in microspheres/custard-apple shapes with fine surface roughness having nanoscales particles sizes with nearly monodisperse and mesoporous in nature. Thus, because of microspherical shape of materials with fine surface roughness could use its whole surfaces through any direction to damage the cell membrane channels and blockage the transport property. Moreover, an alternative mechanism if there is positive ion released from the micromaterials might attach to negatively charged bacterial cell wall and rupture it, hence, leading to protein denaturation and cause death of cells.^[26] The opposite charges of bacteria and nanoparticles were attributed to their adhesion and bioactivity due to electrostatic forces. Therefore, in the present study, more effective zone inhibition was observed in the gram-negative bacteria as compared to gram-positive might be due to gram-negative bacterium has a thin peptidoglycan layer and an outer membrane that contains lipopolysaccharide, phospholipids, and proteins, while gram-positive bacterium has a thick peptidoglycan layer that contains teichoic and lipoteichoic acids. Due to teichoic and lipoteichoic acids the outer membrane of gram-positive bacterium is less rupture, while gram-negative bacterium do not contains such acids, hence outer membrane could rupture fast. Thus, CP was able to bind sulfhydryl group of pathogen enzyme which leads to cell death quickly. Actually, an antimicrobial rate is governed not only by

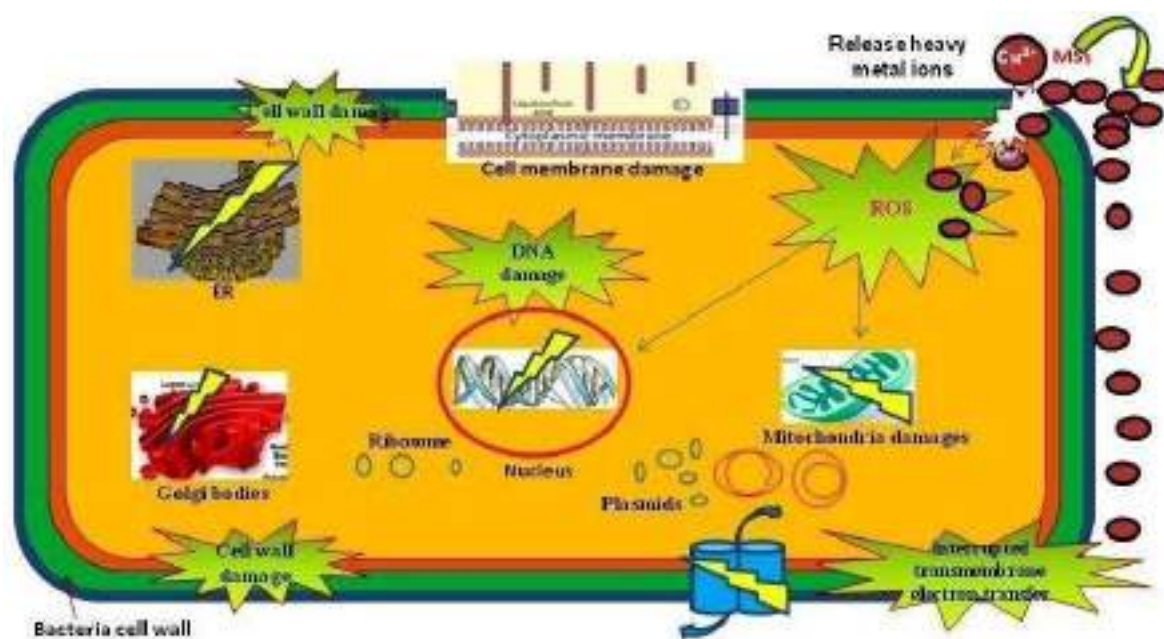
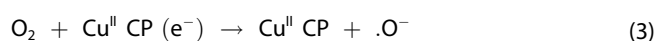
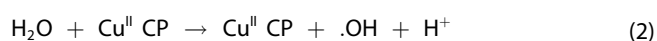


Figure 11. A lethal effects mechanism in bacterial cell by microsphere Cu^{II} CP

cell wall thickness, but also by the morphology of cell wrap and resistance of the outer membrane to the reactive oxygen species produced at micromaterial surface. In addition to, an antibacterial property of CP mostly depends on the presence of reactive oxygen species (ROS). The properties of ROS were due to the large surface area of NPs with its smaller in particle size that increases oxygen vacancies. As increase oxygen vacancies more will be the reactive oxygen species that ultimately cause cell death due to damage organelles, and finally leakage of minerals from cells. This was absolutely due to the superoxide (O_2^-) and hydroxyl (OH^-) radical formation (2) in the cell generated by of ROS (Figure 11). Further reaction of superoxide (O_2^-) (3) with hydrogen ion from coppermaterial that generated to HO_2^- radical (4), and finally these radicals collided with electrons to generate hydrogen peroxide ion ($H_2O_2^-$) (5). Basically, peroxide ions reacted with hydrogen ions, and formed hydrogen peroxide molecules, these molecules were responsible for death of cells. The generation of free radical mechanism was possible after antibacterial plates were irradiated under UV lights.



Antioxidant property

An antioxidant is like a substance that inhibits an oxidative damage to a target molecule or any cell in the living system.^[27] In the present work an antioxidant property of CP was determined by using of DPPH (α , α -diphenyl- β -picrylhydrazyl) method and it was compared with ascorbic acid. For the details experimental study of antioxidant activity sees Supporting Information S5). The comparative results in ethanol and methanol systems have been shown in Figure 12. DPPH is a popularly technique which is used to test the ability of compound to act as free radical scavengers or hydrogen donors to evaluate the antioxidant capacity. The different solvents were used for rendering the scavenging activity (Table 5). The characteristic role of DPPH (α , α -diphenyl- β -picrylhydrazyl) is to trap the free radicals. But, methanolic system shows a satisfactory effect in an inhibiting DPPH. At a concentration of 500 $\mu\text{g/mL}$, the scavenging effects of CP in DPPH radical increased in the order: ethanolic solution (51.25%) < methanolic solution 79.84%).

The results showed that among the solvents analyzed for DPPH scavenging activity, methanolic solvent showed higher radical inhibition activity which was comparable with that of standard ascorbic acid (85%) at 500 $\mu\text{g/mL}$.

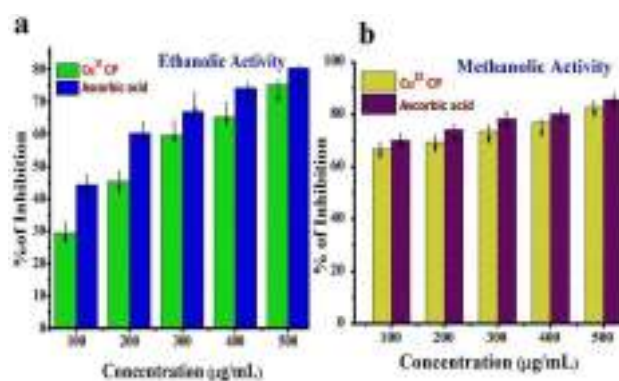


Figure 12. Antioxidant activity of Cu^{II} CP and ascorbic acid by DPPH method

Table 5. Antioxidant activity of Cu^{II} CP by DPPH method

Treatment	Solvent	100 $\mu\text{g/mL}$	200 $\mu\text{g/mL}$	300 $\mu\text{g/mL}$	400 $\mu\text{g/mL}$	500 $\mu\text{g/mL}$
Cu^{II} CP	Ethanol	29.31	45.23	51.56	59.34	65.19
Standard	Ascorbic acid	44.23	60.20	66.96	74.18	80.32
Cu^{II} CP	methanol	66.56	69.32	73.38	76.65	82.77
Standard	Ascorbic acid	70	74	78.33	80.18	85.69

3. Conclusion

We successfully fabricated mesoporous microspheres/microcustard-apples shaped Cu^{II} CP with polydentate chelating ligand (*sbebz*). Electron spectroscopy revealed an octahedral geometry around copper ion with oxidation state 2^+ coordinating by a chelating ligand and water molecules. Amazingly, a structure transformation was taken place, a 1D okra shaped *sbebz* was transformed into 3D microspheres/3D microcustard-apple shaped CP after doping with copper ion. Each microsphere of CP have an average diameter of 2–7 μm , and each microsphere was assembled by several micro/nanospheres having diameter 338–400 nm, while microcustard-apple shaped have an average diameter of each 7–8 μm constituted by countless micro/nanoparticles having diameter sizes 380–450 nm. Moreover, SEM revealed nearly monodispersity in microspheres which was further supported by AFM profile and BET. TEM rendered average particles sizes of nanoparticles about 10–47 nm. As-fabricated material shows best antioxidant property by using α , α -diphenyl- β -picrylhydrazyl in methanolic solvent. Furthermore, a polydentate chelating ligand showed an excellent antimicrobial activity against gram-negative bacteria (*E. coli* and *K. pneumoniae*) than gram-positive bacteria (*S. aureus* and *B. subtilis*). An enhanced and highest inhibition zone was observed after ligand doped with copper ion (CP) against gram-negative pathogen viz. *K. pneumoniae*. Moreover, molecular docking of *sbebz* was executed using both genetic (GA) and non-genetic (Non-GA) algorithm techniques, and achieved docking energy about -6.69852 kcal/mol.

Supporting Information Summary

Supporting information contains detailed experimental procedure for the synthesis of chelating ligand (*sbebz*) and Cu^{II} CP, their spectroscopic characterization (Mass analysis, ¹H NMR, and ¹³C NMR of *sbebz*, and Raman and XPS studies of Cu^{II} CP), materials measurements and experimental protocol for anti-bacterial, antioxidant and molecular docking studies of materials.

Acknowledgements

The author (Rina Bagade) would like to acknowledge BARTI, Pune, India for financial support (BARTI/CSNRF/2015-16/2567). The authors also acknowledge STIC, Cochin, IIT Bombay, Department of Physics RTM Nagpur University, and PGTD Chemistry and Microbiology S. K. Porwal College Kamptee for providing instrumental and pathological facilities. We are also thankful to Sunil G. Chaudhary, Assistant Professor, Department of English, Bramhpuri for his help in editing this paper.

Conflict of Interest

The authors declare no conflict of interest.

Keywords: Antibacterial assay · Antioxidants · Copper (II) chelate polymer · Mesoporous materials · Molecular docking

- [1] a) N. C. Burtch, H. Jasuja, K. S. Walton, *Chem. Rev.* **2014**, *114*, 10575–10612; b) N. Mao, P. Hu, F. Yu, X. Chen, G. Zhuang, T. Zhang, B. Li, *CrystEngComm* **2017**, *19*, 4586–4594; c) S. Noro, S. Kitagawa, T. Akutagawa, T. Nakamura, *Prog. Polym. Sci.* **2009**, *34*, 240–279; d) S. Islam, J. Datta, S. Maity, B. Dutta, F. Ahmed, P. Ghosh, P. Pratim Ray, M. Hedayatullah Mir, *ChemistrySelect* **2019**, *4*, 3294–3299; e) S. Ghosh, N. Hari, S. Mohanta, *ChemistrySelect* **2018**, *3*, 9402–9408.
- [2] a) W. C. Grignonneau, P. L. Chapman, A. G. Menke, F. Walmsley, *J. Inorg. Nucl. Chem.* **1971**, *33*, 3011–3017; b) G. K. Patra, I. Goldberg, *J. Chem. Soc. Dalt. Trans.* **2002**, 1051–1057; c) L. Laxmi, S. Khan, A. Kareem, F. Zafar, N. Nishat, *Spectrochim. Acta A Mol. Bimol. Spectrosc.* **2017**, *188*, 400–410; d) P. Nguyen, P. Gómez-Elipse, I. Manners, *Chem. Rev.* **1999**, *99*, 1515–1548; e) W. L. Zhang, Y. Y. Liu, J. F. Ma, H. Jiang, J. Yang, *Polyhedron* **2008**, *27*, 3351–3358; f) S. Kulovi, S. Dalbera, S. Kanta Dey, S. Maiti-Choudhury, H. Puschmann, E. Zangrando, S. Dalai, *ChemistrySelect* **2018**, *3*, 5233–5242; g) F. B. de Almeida, M. S. Cunha, H. A. De Abreu, R. Diniz, *ChemistrySelect* **2016**, *1*, 3770–3776; h) A. Kuila, N. A. Surib, N. S. Mishra, A. Nawaz, K. H. Leong, L. C. Sim, P. Saravanan, S. Ibrahim, *ChemistrySelect* **2017**, *2*, 6163–6177; i) S. Khan, A. Al Masum, P. Giri, M. M. Islam, K. Harms, S. Chattopadhyay, *ChemistrySelect* **2018**, *3*, 7112–7122.
- [3] a) A. Mohanty, A. Mondal, *Nanoscale* **2013**, *5*, 7238; b) V. A. Larionov, L. V. Yashkina, A. F. Smol'yakov, Y. V. Zubavichus, K. K. Babievsky, N. V. Akat'yev, A. A. Titov, Y. N. Belokon, V. I. Maleev, *ChemistrySelect* **2018**, *3*, 653–656; c) M. R. Shimpi, L. Giri, V. Rao Pedireddi, *ChemistrySelect* **2018**, *3*, 855–858; d) F. Baig, S. Khullar, S. K. Mandal, M. Sarkar, *ChemistrySelect* **2017**, *2*, 11677–11685.
- [4] a) O. M. Yaghi, M. O'Keeffe, N. W. Ockwig, H. K. Chae, M. Eddaoudi, J. Kim, *Nature* **2003**, *423*, 705–714; b) S. Mukherjee, S. Ganguly, K. Manna, S. Mondal, S. Mahapatra, D. Das, *Inorg. Chem.* **2018**, *57*, 4050–4060; c) D. Braga, F. Grepioni, O. Shemchuk, *Cryst EngComm* **2018**, *20*, 2212–2220; d) R. M. C. S. Diniz, C. E. S. Nogueira, C. C. Santos, F. S. M. Sinfrônio, F. F. de Sousa, A. S. de Menezes, *Spectrochim. Acta A Mol. Bimol. Spectrosc.* **2018**, *205*, 603–613.
- [5] a) R. Tayebbe, V. Amani, H. R. Khavasi, *Chin. J. Chem.* **2008**, *26*, 500–504; b) H. Shabbir, M. A. Hartmann, *New J. Phys.* **2017**, *19*, 93024; c) D. P. Wang, J. C. Lai, H. Y. Lai, S. R. Mo, K. Y. Zeng, C. H. Li, J. L. Zuo, *Inorg. Chem.* **2018**, *57*, 3232–3242; d) R. G. Chaudhary, H. D. Juneja, M. P. Gharpure, *J. Thermal Anal. Calorim.* **2013**, *112*, 637–647.
- [6] a) I. Kaya, *J. Inorg. Organomet. Polym.* **2010**, *20*, 369–79; b) E. J. Mensforth, M. R. Hill, S. R. Batten, *Inorganica Chim. Acta.* **2013**, *403*, 9–24.
- [7] a) M. L. Chen, Z. H. Zhou, *Inorganica Chim. Acta.* **2017**, *458*, 199–217; b) R. Robson, *Dalt. Trans.* **2008**, 5113; c) D. Bejan, L. G. Bahrin, S. Shova, M. Sardaru, L. Clima, A. Nicolescu, N. Marangoci, V. Lozan, C. Janiak, *Inorganica Chim. Acta.* **2018**, *482*, 275–283; d) C. Janiak, *Dalt. Trans.* **2003**, 2781; e) S. Sun, Y. Sun, H. Guo, X. Fu, M. Guo, S. Liu, X. Guo, L. Zhang, E. V. Alexandrov, *Inorganica Chim. Acta.* **2018**, *483*, 165–172; f) M. Yan, S. Chen, S. Zhang, J. Ru, R.-F. Zhang, *Inorganica Chim. Acta.* **2018**; g) G. I. Dzhardimalieva, I. E. Uflyand, *RSC Adv.* **2017**, *7*, 42242–42288.
- [8] a) L. Hashemi, A. Morsali, F. Marandi, I. Pantenburg, A. Azhdari Tehrani, *New J. Chem.* **2014**, *38*, 3375; b) L. Huang, **2003**, *58*, 105–114; c) A. Umamura, S. Diring, S. Furukawa, H. Uehara, T. Tsuruoka, S. Kitagawa, *J. Am. Chem. Soc.* **2011**, *133*, 15506–15513; d) R. Seetharaj, P. V. Vandana, P. Arya, S. Mathew, *Arab. J. Chem.* **2016**, *12*, 295–315.
- [9] a) J. Zhang, L. Wojtas, R. W. Larsen, M. Eddaoudi, M. J. Zaworotko, *J. Am. Chem. Soc.* **2009**, *131*, 17040–17041; b) K. Wang, Z. Geng, M. Zheng, L. Ma, X. Ma, Z. Wang, *Cryst. Growth Des.* **2012**, *12*, 5606–5614; c) W. T. Deng, J. C. Liu, T. B. Wei, B. Wang, S. Q. Niu, *Synth. React. Inorganic, Met. Nano-Metal Chem.* **2014**, *44*, 552–557.
- [10] a) I. P. Ejidike, P. A. Ajibade, *Bioinorg. Chem. Appl.* **2015**, *201*, 1–9; b) T. Taghipour, G. Karimipour, M. Ghaedi, A. Asfaram, *Ultrason. Sonochem.* **2018**, *41*, 389–396; c) A. Liu, C. Z. Wang, C. Chu, H.-Y. Chu, X. Chen, A. F. Du, J. Mao, W. Zheng, C. C. Wang, *J. Environ. Chem. Eng.* **2018**, *6*, 4961–4969; d) R. Arif, P. S. Nayab, I. A. Ansari, M. Shahid, M. Irfan, S. Alam, M. Abid, Rahisuddin, *J. Mol. Struct.* **2018**, *1160*, 142–153; e) A. U. Mirza, A. Kareem, S. A. A. Nami, M. S. Khan, S. Rehman, S. A. Bhat, A. Mohammad, N. Nishat, *J. Photochem. Photobiol. Biol.* **2018**, *185*, 262–274; f) M. Sankarganesh, J. Dhaweethu Raja, K. Sakthikumar, R. V. Solomon, J. Rajesh, S. Athimoolam, V. Vijayakumar, *Bioorg. Chem.* **2018**, *81*, 144–156.
- [11] a) R. G. Chaudhary, H. D. Juneja, R. Pagadala, N. V. Gandhare, M. P. Gharpure, *J. Saudi Chem. Soc.* **2015**, *19*, 442–453; b) M. A. Haque, R. G. Chaudhary, L. J. Paliwal, *Inorganica Chim. Acta.* **2017**, *462*, 298–307; c) R. G. Chaudhary, N. V. Gandhare, H. D. Juneja, M. P. Gharpure, *Res. J. Pharm. Biol. Chem. Sci.* **2013**, *4*, 1625–1636; d) R. G. Chaudhary, H. D. Juneja, N. V. Gandhare, *J. Chin. Adv. Mater. Soc.* **2013**, *1*, 305–316.
- [12] A. A. El-Asmy, A. Z. Al-Abdeen, W. M. Abo El-Moaty, M. M. Mustaffa, *Spectrochim. Acta A.* **2010**, *75*, 1561.
- [13] A. M. Rocco, J. L. Wardell, R. P. Pereira, *J. Therm. Anal. Calorim.* **2012**, *107*, 345–354.
- [14] P. L. Maurya, B. V. Agrawal, A. K. Dey, *J. Ind. Chem. Soc.* **1980**, *57*, 275.
- [15] a) A. Foziah, A. L. Saif, M. S. Refat, *J. Therm. Anal. Calorim.* **2012**, *111*, 2079–2096; b) R. G. Chaudhary, H. D. Juneja, M. P. Gharpure, *J. Chin. Adv. Mater. Soc.* **2013**, *1*, 121–133; c) H. S. Patel, D. J. Patel, *Int. J. Polym. Mater.* **2010**, *39*, 307–317; d) G. G. Mohamed, M. M. Omar, A. M. Hindy, *Turk. J. Chem.* **2006**, *30*, 361–382; e) A. Mohammad, A. A. Inamuddin, *J. Therm. Anal. Calorim.* **2012**, *107*, 127–134.
- [16] a) R. G. Chaudhary, H. D. Juneja, N. V. Gandhare, S. Bhuyar, M. P. Gharpure, S. Mondal, J. A. Tanna, *J. Chin. Adv. Mater. Soc.* **2014**, *2*, 244–258; b) R. G. Chaudhary, P. Ali, N. V. Gandhare, J. A. Tanna, H. D. Juneja, *Arab. J. Chem.* DOI 10.1016/j.arabj.2016.03.008; c) G. S. Padole-Gaikwad, R. D. Bagade, R. G. Chaudhary, M. P. Gharpure, H. D. Juneja, *J. Chin. Adv. Mater. Soc.* **2017**, *5*, 118–132.
- [17] A. Ilijinas, L. Marcinauskas, *Thin Solid Films*, **2015**, *594*, 192–196.
- [18] a) J. Zhang, Q. Han, X. Wang, J. Zhu, G. Duan, *Mater. Lett.* **2016**, *162*, 218–221; b) A. K. Potbhare, R. G. Chaudhary, P. B. Chouke, S. Yerpude, A. Mondal, V. Sonkusare, A. R. Rai, H. D. Juneja, *Mater. Sci. Eng. C.* **2019**, *99*, 783–793.
- [19] J. Zhang, J. Liu, Q. Peng, X. Wang, Y. Li, *Chem. Mater.* **2006**, *18*, 867–871.
- [20] a) B. Mirtamizdous, M. S. shalamzari, S. Behrouzi, M. H. florencio, H. K. Fun, *J. Inorg Organomet Polym.* **2012**, *22*, 1358–1364; b) L. Hashemi, A. Morasali, *Ultrason. Sonochem.* **2015**, *24*, 146–149.
- [21] L. Hashemi, A. Morasali, *Ultrason. Sonochem.* **2014**, *21*, 1417–1423.
- [22] a) S. Donini, D. M. Ferraris, R. Miggiano, A. Massarotti, M. Rizzi, *Sci. Rep.* **2017**, *7*, 1180; b) L. Esser, F. Zhou, Y. Zhou, Y. Xiao, W. Tang, C. Yu, Z.

- Qin, D. Xia, *J. Biol. Chem.* **2016**, *291*, 25019–25031; c) A. C. Pratt, S. W. Dewage, A. H. Pang, T. Biswas, S. B. Britson, G. A. Cisneros, O. V. Tsodikov, *J. Struct. Biol.* **2015**, *192*, 76–87.
- [23] C. Mügge, T. Marzo, L. Massai, J. Hildebrandt, G. Ferraro, P. Rivera-Fuentes, N. Metzler-Nolte, A. Merlino, L. Messori, W. Weigand, *ACS Inorg. Chem.* **2015**, *54*, 8560–8570.
- [24] a) A. Casini, G. Mastrobuoni, C. Temperini, C. Gabbiani, S. Francese, G. Moneti, C. T. Supuran, A. Scozzafava, L. Messori, *Chem. Commun.* **2007**, *2*, 156–158; b) L. Messori, T. Marzo, E. Michelucci, I. Russo Krauss, C. Navarro-Ranninger, A. Quiroga, A. G. Merlino, *Inorg. Chem.* **2014**, *53*, 7806–7808; c) L. Messori, F. ScalettiMassai, L. Cinellu, M. A. Gabbiani, C. Vergara, A. Merlino, *A. Chem. Commun.* **2013**, *49*, 10100–10102; d) D. Marasco, L. Messori, T. Marzo, A. Merlino, *Dalton. Trans.* **2015**, *44*, 10392–10398.
- [25] J. Elechiguerra, J. Burt, J. Morones, A. Camacho-Bragado, X. Gao, H. H. Lara, M. Jose Yacaman, *J. Nanobiotechnol.* **2005**, *3*, 6.
- [26] I. Sondi, B. S. Sondi, *J. Colloid. Interface Sci.* **2004**, *275*, 177–182.
- [27] S. Yamagishi, T. Matsui, *Pharmacol. Res.* **2011**, *64*, 187–194.

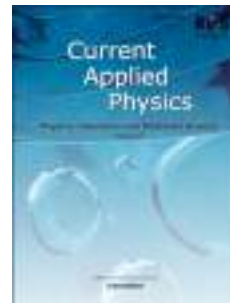
Submitted: March 27, 2019

Accepted: May 16, 2019

Accepted Manuscript

Cu₂S nanocrystals incorporated highly efficient non-fullerene ternary organic solar cells

Govinda Lakhotiya, Namdeo Belsare, Abhimanyu Rana, Vinay Gupta



PII: S1567-1739(19)30006-9

DOI: <https://doi.org/10.1016/j.cap.2019.01.006>

Reference: CAP 4903

To appear in: *Current Applied Physics*

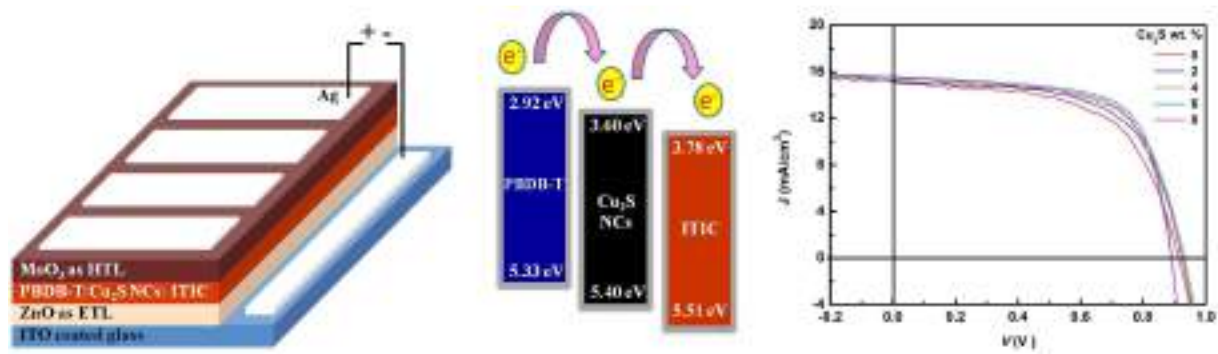
Received Date: 5 November 2018

Revised Date: 25 December 2018

Accepted Date: 4 January 2019

Please cite this article as: G. Lakhotiya, N. Belsare, A. Rana, V. Gupta, Cu₂S nanocrystals incorporated highly efficient non-fullerene ternary organic solar cells, *Current Applied Physics* (2019), doi: <https://doi.org/10.1016/j.cap.2019.01.006>.

This is a PDF file of an unedited manuscript that has been accepted for publication. As a service to our customers we are providing this early version of the manuscript. The manuscript will undergo copyediting, typesetting, and review of the resulting proof before it is published in its final form. Please note that during the production process errors may be discovered which could affect the content, and all legal disclaimers that apply to the journal pertain.



Cu₂S nanocrystals incorporated highly efficient non-fullerene ternary organic solar cells

*Govinda Lakhotiya^{1,2}, Namdeo Belsare², Abhimanyu Rana³ and *Vinay Gupta⁴

¹*Department of Physics, Jankidevi Bajaj College of Science (Autonomous), Wardha- 442001, India*

²*Department of Physics, Vidyabharati Mahavidyalaya, Amravati-444602, India*

³*School of Engineering and Technology, BML Munjal University, Haryana -122413, India*

⁴*Advanced Materials and Devices Division, CSIR-National Physical Laboratory, New Delhi-110012, India*

Abstract:

Here, we report Cu₂S nanocrystals based non-fullerene ternary polymer solar cells by incorporating Cu₂S in conjugated polymer (PBDB-T: poly[(2,6-(4,8-bis(5-(2-ethylhexyl)thiophen-2-yl)-benzo[1,2-b:4,5-b']dithiophene))-alt-(5,5-(1',3'-di-2-thienyl-5',7'-bis(2-ethylhexyl) benzo[1',2'-c:4',5'-c']dithiophene-4,8-dione))] and small molecule non-fullerene compound (ITIC:3,9-bis(2-methylene-(3-(1,1-dicyanomethylene)-indanone))-5,5,11,11-tetrakis(4-hexylphenyl)-dithieno[2,3-d:2',3'-d']-s-indaceno[1,2-b:5,6-b']dithiophene). The devices were fabricated in inverted configuration i.e. ITO/ZnO/PBDB-T: Cu₂S NCs: ITIC/MoO₃/Ag. Effect of concentration of Cu₂S nanocrystals on the performance parameters of PBDB-T: ITIC based organic solar cells is studied. An enhancement in the power conversion efficiency from 8.24% to 9.53% is achieved for optimum concentration of Cu₂S nanocrystals in the organic photoactive blend. The cause of improvement in the performance parameters of the device is investigated by means of the light intensity dependent electrochemical impedance spectroscopy and atomic force microscopy. It is found that the devices with Cu₂S nanocrystals have less trap-assisted recombination.

Keywords: Cu₂S nanocrystals, organic solar cells, PBDB-T, ITIC, photo electrochemical impedance spectroscopy.

*Corresponding Author E-mail: lakhotiya.govinda@gmail.com (G.L),
drvinyagupta@netscape.net (V.G)

1. Introduction:

It is well known that in comparison to conventional silicon-based solar cells, third generation solar cells which includes dye-sensitized solar cells (DSSCs), bulk-heterojunction organic/polymer solar cells (OSCs/PSCs), organic-inorganic hybrid solar cells (HSCs) and perovskite solar cells (PSCs) offers two main advantages: solution processability and low processing temperature [1-4]. Besides this, OSCs offer good cost-efficiency balance, short energy payback time, low-cost materials, scalable fabrication using screen printing, inkjet printing and roll-to-roll printing, and adaptability to flexible plastic substrates and therefore are of considerable interest in the recent times [5-7]. However, their power conversion efficiency (PCE) is still behind the other members of the third generation solar cells due to the narrow band gap of donor polymer and poor mobility of carriers in both donor polymers and fullerene-based acceptors [8-10]. To overcome this, in the last two decades, new low bandgap donor polymer and high electron mobility acceptors have been developed [11-14]. Although this has helped to improve the laboratory scale OSCs with PCE >17%, specially in case of tandem solar cells but commercialization of OSCs requires much higher PCE and stable device performance [15-20]. Fabricating a tandem OSCs is very challenging due to technical complexities as it involves multi-layer stacking, processing of a robust intermediated layer, and coupling of appropriate absorbers as well as the optimization of the active layer's thickness [21, 22]. On the other hand, fabrication of ternary OSCs is relatively better option and needs identification of the suitable third component of the ternary blend [23-26]. In some of the systems, PCE has increased and reached maxima with the optimization of the concentration of the third component in the matrix of the donor polymer and acceptor.

In general, ternary OSCs consists of photoactive layer spin-casted using ternary photoactive blend comprised of donor polymer/solution processable small molecule, fullerene/non-fullerene acceptor and the third component [25-28]. The choice of the third component is primarily done on the basis of the role expected such as cascade or parallel charge transfer, energy transfer, complementary absorption of donor polymers, in-situ light scattering, etc.[25-28]. Thus, in principle, it could be anything such as additional donor polymer, acceptor, sensitizer (dye/metal, semiconductors and dielectric nanocrystals (NCs)), etc. Till date, a variety of ternary OSCs were fabricated using the third component discussed above and has shown improvement in the performance parameters. Among them, ternary OSCs with semiconducting

NCs as the third component are of significant interest. Addition of semiconducting NCs brought a lot of advantages associated with semiconducting NCs such as tunable bandgap, scalable synthesis, energy band alignments that aids in exciton dissociation. Most important characteristics of NCs are its excellent charge transport, solubility in host matrix solvent and high thermal and photo-chemical stability. To exploit these advantages, semiconducting NCs of various semiconductors like CdSe, CdS, CdTe, Si, PbS, ZnO, Cu₂S, and FeS₂ have been incorporated in the photoactive blends comprised of multiple donors: acceptors systems [29-35]. However, to the best of our knowledge, there are hardly any reports on non-fullerene ternary OSCs with semiconducting NCs as the third component.

Here in, we report nanocrystals (NCs) based non-fullerene ternary polymer solar cells. For this, synthesis of Cu₂S NCs has been carried out and its effect on one of the most efficient solution processable organic solar cells (OSCs) consisting conjugated polymer (PBDB-T:poly[(2,6-(4,8-bis(5-(2-ethylhexyl)thiophen-2-yl)-benzo[1,2-b:4,5'-]dithiophene))-alt-(5,5-(1',3'-di-2-thienyl-5',7'-bis(2-ethylhexyl)benzo[1',2'-c:4',5'-c']dithiophene-4,8-dione))]) and small molecular non-fullerene compound (ITIC: 3,9-bis(2-methylene-(3-(1,1-dicyanomethylene)-indanone))-5,5,11,11-tetrakis(4-hexylphenyl)-dithieno[2,3-d:2',3'-d']-s-indaceno[1,2-b:5,6-b']dithiophene) has been studied. Cu₂S could be an interesting system due to low bandgap of ~1.21 eV (indirect), giving absorption over wide spectrum in UV-Vis.-NIR region, and therefore can harness the major part of the solar spectrum [29, 30]. Also, the conduction band of Cu₂S around 3.60 eV is well positioned between LUMO of donor polymer PBDB-T and fullerene free acceptor ITIC, acting as an electron cascade between them [29, 30]. Thus, here, we synthesized Cu₂S NCs and characterized it for the phase purity and crystal structure, morphology, and optical properties. This is followed by a systematic study to investigate variation in the performance parameters of PBDB-T: ITIC OSCs with a change in the concentration of Cu₂S NCs. The obtained results were explained by means of the light intensity dependent electrochemical impedance spectroscopy and atomic force microscopy.

2. Experimental:

2.1 Synthesis of Cu₂S NCs

In present study, synthesis of Cu₂S NCs has been carried out by slightly modifying the protocol developed by Alivisatos et al. [36]. Briefly, synthesis of colloidal Cu₂S NCs involves

hot injection reaction between copper(II) acetylacetonate and ammonium diethyldithiocarbamate in a mixed solvent of dodecanethiol and oleic acid. The detailed experimental procedure can be found elsewhere.

2.2 Device fabrication

Devices were fabricated following the device architecture mentioned in Fig. 3(a) and corresponding energy levels of the materials used in the fabrication are shown in Fig. 3(b). At first, a photoactive blend comprised of PBDB-T (10 mg) and ITIC (10 mg) was prepared in 1 ml of CB with 0.5% v/v of 1, 8 diiodooctane (DIO) solvent as an additive. The solution was allowed to stir at 50 °C in the dark for at least 12 h [12]. For ternary photo-active blend, some part of ITIC is replaced by the equal amount of Cu₂S NCs. For the device fabrication, sol-gel ZnO, synthesized by the method reported elsewhere, was spin-coated on the pre-cleaned ITO coated glass substrates (with a sheet resistance of 15 Ωsq⁻¹ and transmittance > 85%) at 2000 rpm for 30 s to obtain a film of ≈40 nm [37]. The substrates were annealed at 200 °C for 15 min to remove excess solvents. After that, the photoactive blend was spin-coated at 2500 rpm for 60 s to obtain a film thickness of ≈100 nm and annealed at 160 °C for 10 min. Subsequently, the devices were evaporated using the shadow mask by thermal evaporation of 10 nm MoO₃ layer as a hole transport layer and 100 nm Ag electrode as an anode.

2.3 Device characterization and testing

Keithley 2600 source meter, and a Newport solar simulator (model number 91160) with AM 1.5G spectral distribution at 1000W/m² intensity was used for J-V characteristics of the cells. Bentham's PVE300 was used external quantum efficiency (EQE) spectra. Using a shadow mask, the active device area of the cells was fixed as 7 mm². Atomic force microscopy (AFM) of the films of photoactive blends with the different wt % of Cu₂S NCs has been carried out on Nanosurf's C 3000 model.

3. Results and Discussion:

Before employing the synthesized Cu₂S nanocrystals (NCs) into the photoactive blend, a systematic study has been carried out to confirm phase purity and crystal structure, morphology and optical properties of the synthesized Cu₂S NCs. Fig. 1(a) depicts the X-ray diffraction

pattern (Cu K_{α} radiation, $\lambda = 1.5418 \text{ \AA}$, Rigaku's MiniFlex 600) of as-synthesized Cu_2S NCs employed at a scanning rate of $5^\circ/\text{min}$ in the 2θ range from 20° to 80° . Presence of all the prominent peaks and their corresponding 2θ value are in close agreement with the previous studies and conforms to the JCPDS file no.00-026-1116 [30, 38]. This confirms the hexagonal crystal structure of the as synthesized Cu_2S NCs. Absence of additional peaks besides the peaks of Cu_2S NCs confirms that the adopted protocol yields the pure phase of Cu_2S NCs which is essential for the device fabrication. Fig. 1(b) depicts the UV-Vis.-NIR absorbance spectra (Shimadzu 1800) of dispersion of the synthesized Cu_2S NCs in ethanol (1 mg/ml). It can be clearly seen that the as-synthesized Cu_2S NCs has wide absorption spectrum up to 1000 nm covering wide spectrum in UV-Vis.-NIR region and therefore it is capable of harnessing the major part of the solar spectrum [30].

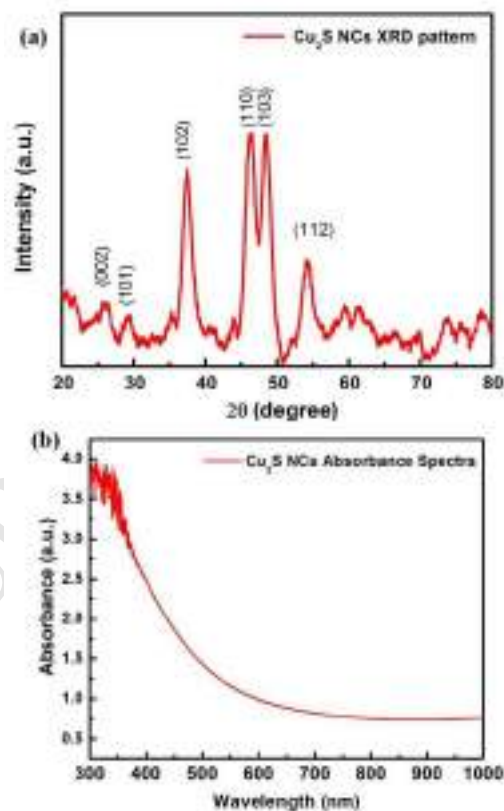


Fig. 1 (a) XRD pattern and (b) UV- Vis.-NIR absorption spectra of as synthesized Cu_2S NCs.

However, to confirm morphology, particle size and their distribution, HRTEM images (Jeol's JEM-2200FS) of as-synthesized Cu_2S NCs have been taken. From the Fig. 2(a) and (b), it is clearly seen that the particles are slightly elongated and possess uniform size distribution

whose length and diameter are around 10-20 nm and 6-10 nm respectively. The crystallinity of the as-synthesized Cu_2S NCs with an inter-layer spacing of 0.198 nm replicates quite well with d-spacing of the (110) plane of Cu_2S NCs [31].

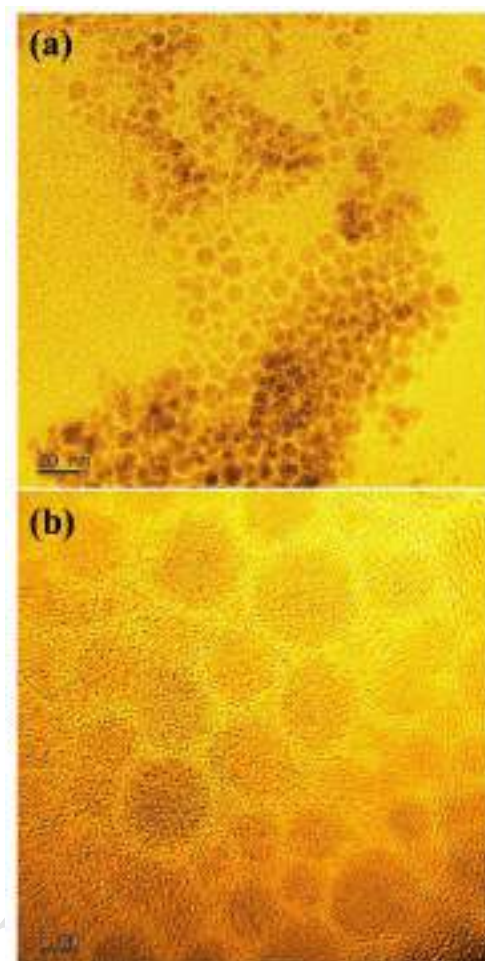


Fig. 2 (a-b) HRTEM images of as synthesized Cu_2S NCs.

After confirming the phase purity and crystal structure, morphology and optical properties of the synthesized Cu_2S NCs, nanocrystals based non-fullerene polymer solar cells were fabricated. As can be seen in Fig. 3(a), the conduction band of the Cu_2S lies between LUMO of donor polymer PBDB-T and non-fullerene ITIC, and therefore we hypothesize the enhancement in the device performance [39]. Devices were fabricated as shown in the Fig. 3(b) whose procedure including the blend composition has been discussed in the experimental section.

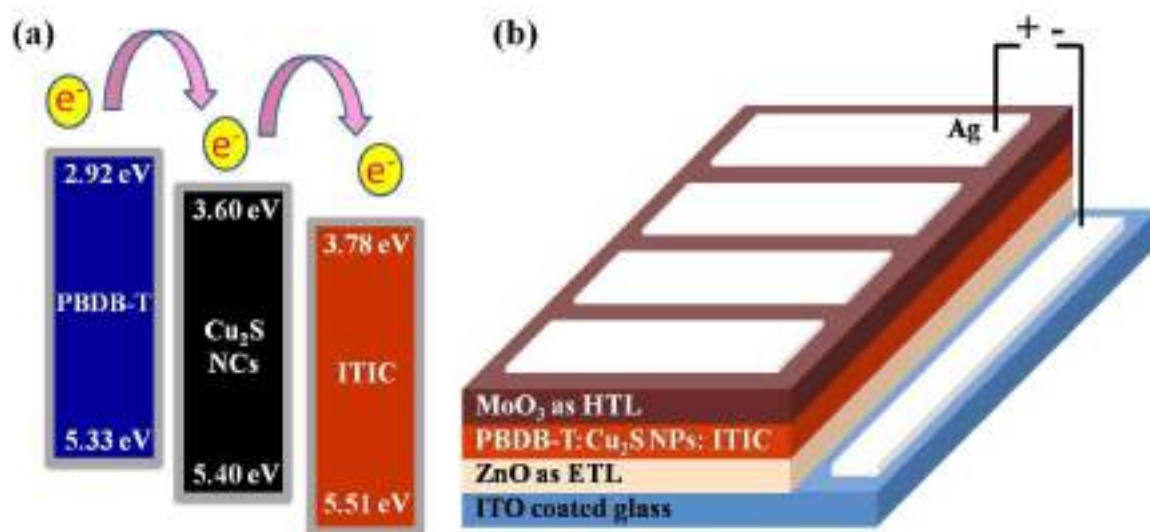


Fig. 3 (a) Energy levels of materials used in the solar cell device and (b) Schematic highlighting device architecture ITO/ZnO/PBDB-T: Cu₂S NCs: ITIC/MoO₃/Ag.

Fig. 4(a) and (b) shows the J–V characteristics and EQE spectra of PBDB-T: Cu₂S NCs: ITIC ternary device as a function of wt % of Cu₂S NCs and corresponding performance parameters has been described in the Table 1. As can be seen in the Table 1, with the increase in the wt % of Cu₂S NCs, initially there is a slight increase in the V_{oc} till the concentration of Cu₂S NCs is 4 wt %. This is the expected outcome as it is well established that V_{oc} depends on the energy difference between the HOMO of the donor polymer and the LUMO of the acceptor [40, 41]. Addition of Cu₂S NCs generates the possibility of an energy level offset between the LUMO of the Cu₂S NCs and the HOMO of donor polymer which is better than the energy level offset between the LUMO of ITIC and the HOMO of the donor polymer [39]. However, with increase in the concentration of Cu₂S NCs over 4 wt %, the surface defects of Cu₂S NCs dominates to create the shallow energy level trap in Cu₂S NCs leading to the disturbance of the energy level offset. Also, with the increase in wt % of Cu₂S NCs (till 6 wt %), there is a gradual increase in the current density (J_{sc}) and fill factor (FF). As a result, PCE of the device increases from 8.24 % to 9.53 %. This is ~15 % increase in the device PCE. This increase in the J_{sc} , FF and PCE can be understood by the observed decrease in the values of series resistance (R_s) and increase in the values of shunt resistance (R_{sh}) and can be attributed to PBDB-T, ITIC and Cu₂S NCs charge transfer type interaction by considering that the added Cu₂S NCs may bind with PBDB-T: ITIC via dipole-dipole interaction and form a charge transfer complex (CTC) [30, 35]. Upon further

addition of Cu_2S NCs beyond 6 wt %, there is a decrease in the J_{sc} and FF. This leads to the decrease in PCE which might be due to the agglomeration of Cu_2S NCs in the matrix owing to less CTC formation. It can be said that the agglomeration of Cu_2S NCs increases R_s and decreases R_{sh} . EQE spectra also shows similar trend and resemble with the trend observed in J-V curves. Calculated values of J_{sc} from EQE are shown in the Table 1. However, to visualize complete picture, we have done intensity dependent photo-EIS measurements and discussed that in the subsequent section.

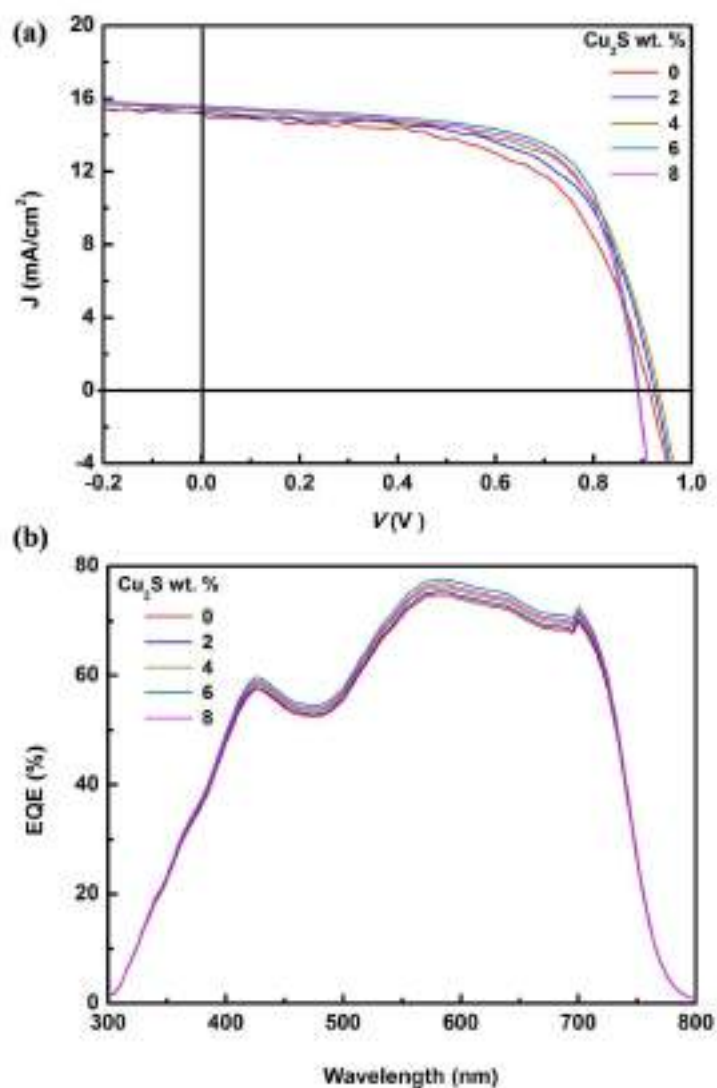


Fig. 4 (a) J – V characteristics under illumination (AM 1.5G, one sun) and (b) EQE spectra of PBDB-T: Cu_2S NCs: ITIC ternary OSCs with different wt % of Cu_2S NCs.

Table 1 Summary of J –V characteristics curves PBDB-T: Cu₂S NCs: ITIC devices with different wt % of Cu₂S NCs.

Cu ₂ S NCs wt %	V _{oc} (V)	Measured J _{sc} (mA/cm ²)	Calculated J _{sc} ¹⁾ (mA/cm ²)	FF (%)	PCE Best (%) ²⁾	R _s (Ωcm ²)	R _{sh} (Ωcm ²)
0 %	0.91	15.11	15.07	59.45	8.24 (8.18)	9.36	234.07
2 %	0.92	15.20	15.19	62.36	8.74 (8.69)	8.17	412.68
4 %	0.93	15.31	15.36	64.38	9.18 (9.11)	8.09	465.78
6 %	0.88	15.59	15.65	69.45	9.53 (9.45)	4.51	865.14
8 %	0.88	15.48	15.48	68.11	9.27 (9.22)	4.90	728.73

¹⁾ Calculated from EQE data.

²⁾ Average of the five devices in parentheses.

The incident light intensity dependent EIS spectra of both reference device (Cu₂S NCs, 0 wt %) as well as the best performing device (Cu₂S NCs, 6 wt %) are highlighted in Fig. 5 (a) and (b) respectively. It is apparently evident that in both the cases, photo-EIS spectra consist of only one semi-circle and can be fitted by a simple R_{rec}*C_μ equivalent circuit, where R_{rec} is a recombination resistance (R_{rec}) and C_μ is the chemical capacitance (C_μ). For attaining the proper fit, capacitor element has been replaced by commonly used constant phase elements (CPE) which gives a distribution of circuit element values in an equivalent circuit to account for any spatial inhomogeneity in the photoactive layer. For an ideal capacitor of capacitance C, the impedance is given by Eq (1) and in the case of a CPE, it is rather characterized by Eq (2) [42]. From above equations, it is apparent that CPE is equivalent to capacitance. If P equals 1, then Eq (2) is identical to Eq (1). In present study, the CPE exponent (P) is varied from 0.85 and 1 and is well within the acceptable values.

$$Z_C = 1/i\omega C \quad (1)$$

$$Z_{CPE} = 1/CPE(i\omega)^P \quad (2)$$

Before analyzing the photo-EIS data, it is essential to mention here that there are basically three different ways of calculating the order of recombination using EIS data: 1) using exponent of the recombination resistance as function of V_{oc} 2) using exponent of the recombination resistance and chemical capacitance as function of V_{oc} 3) slope of $\tau \propto n^{-\delta}$ [42].

We will discuss all the above the cases in the context of the reference device (Cu₂S NCs, 0 wt %) and the best performing device (Cu₂S NCs, 6 wt %) [42].

From Fig. 6(a) and (b), it can be observed that with increase in V_{oc} , the resistance and capacitance changes exponentially. Thus, recombination resistance and chemical capacitance can be fitted as a function of V_{oc} using the exponential laws mentioned in the Eq (3) and (4) [43]. This will give the insight about recombination processes within the devices. For the reference device (Cu₂S NCs, 0 wt %), obtained values of α and β are 0.30 and 0.83 respectively. However, for the best performing device (Cu₂S NCs, 6 wt %) α and β are 0.38 and 0.92 respectively. As discussed above, impedance measurements allow us to establish a direct relation between the order of recombination (λ) and exponents of resistance dependences on V_{oc} (β) and are given by Eq (5). Value of λ is 1 for trap-assisted recombination and is 2 for bimolecular recombination. In the present study, the order of recombination (λ) for reference device (Cu₂S NCs, 0 wt %) and for the best performing device (Cu₂S NCs, 6 wt %) are 1.66 and 1.84 respectively [43]. Thus, in both the cases, recombination losses are due to both trap-assisted recombination and bimolecular recombination [42]. However, it can be clearly observed that in the case of Cu₂S NCs 6 wt %, there are less trap assisted recombination which could be due to the facilitation of charge transfer from PBDB-T to ITIC through Cu₂S NCs. Thus, the presence of Cu₂S NCs improves the device performance by minimizing the trap-assisted recombination.

$$R_{rec} \propto \exp(-\beta V_{oc}/K_B T) \quad (3)$$

$$C_{\mu} \propto \exp(\alpha V_{oc}/K_B T) \quad (4)$$

$$\lambda = 2\beta \quad (5)$$

$$\lambda = \frac{\beta}{\alpha} \quad (6)$$

Order of recombination can also be calculated by using exponent of the recombination resistance and chemical capacitance as a function of V_{oc} using the Eq (6). Recombination process can be thought of as a multiple trapping mechanisms. Here, trapped holes can either recombine with electrons at the acceptor levels or get retrapped at an exponential tail of donor states [43]. In the present study, the order of recombination (λ) using the Eq (6) for reference device (Cu₂S NCs, 0 wt %) and for the best performing device (Cu₂S NCs, 6 wt %) are 2.76 and 2.44

respectively. This means that multiple trapping recombinations are less pronounced in the case of best performing device (Cu₂S NCs, 6 wt %).

To calculate the order of recombination using $\tau \propto n^{-\delta}$, we need to calculate recombination time and carrier density [44]. Response time representative of the recombination processes is calculated from the characteristic frequency (ω) at the top of the arc, where $2\pi\omega = 1/\tau$ [45, 46]. For both the devices, effective recombination time (τ) range in the order of 10^{-5} to 10^{-6} sec. Additionally, the charger carrier density (n) can be estimated from the chemical capacitance (C_{μ}) using Eq (7).

$$n = \frac{1}{e} \int_0^{V_{oc}} C_{\mu}(V) dv \quad (7)$$

$$\tau \propto n^{-\delta} \quad (8)$$

$$\lambda = (1 + \delta) \quad (9)$$

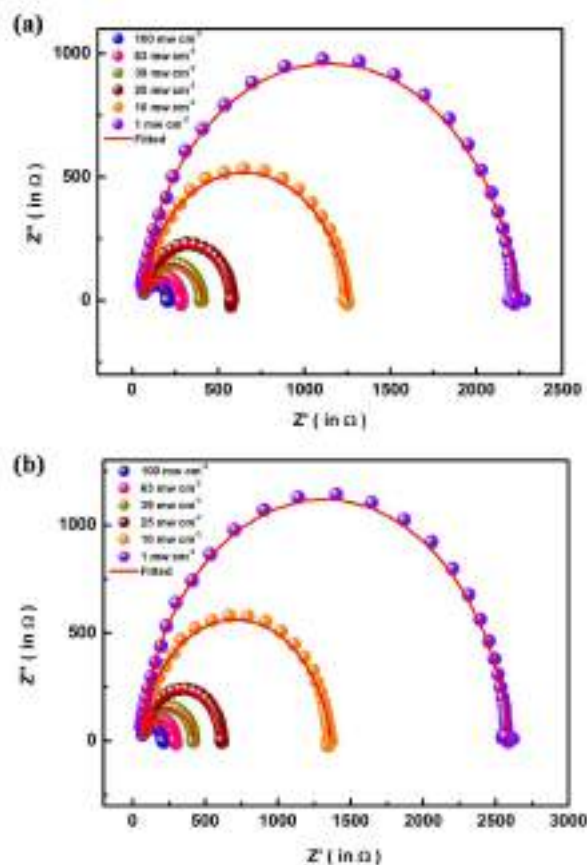


Fig. 5 Nyquist plots of PBDB-T: Cu₂S NCs: ITIC ternary OSCs under different white light illumination intensities with (a) 0 wt % of Cu₂S NCs and (b) 6 wt % of Cu₂S NCs.

A graph between carrier lifetime versus photo-generated carrier density is represented by Fig. 6(c). All the curves in the graph show decay dynamics that follow a power law trend mentioned in the Eq (8). The order of recombination (λ) can be obtained value from slope (δ) by using the relation given in the Eq (9). In both the cases, it was observed that the order of recombination is ~ 2 suggesting that bimolecular recombination is the prominent loss mechanism [44].

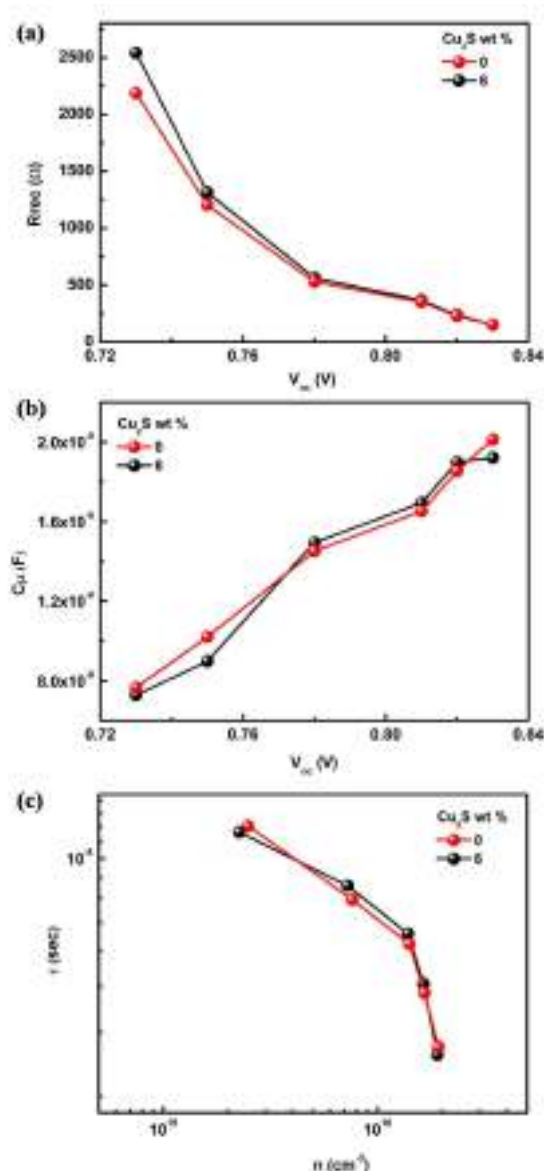


Fig. 6 (a) Recombination resistance (R_{rec}) as a function of V_{oc} , (b) Chemical capacitance (C_{μ}) as a function of V_{oc} and (c) Carrier life time as a function of the photo-generated carrier density of PBDB-T: Cu₂S NCs: ITIC ternary OSCs with 0 wt % and 6 wt % of Cu₂S NCs.

In order to investigate the topology of the photoactive films, binary and ternary blends of PBDB-T:Cu₂S:ITIC is spin casted over the ITO substrate and AFM height images were captured and is represented in Fig. 7. Film in the Fig. 7(a) represents the topology of binary photoactive blend which shows clusters with many aggregated domains and found to possess root mean square (RMS) surface roughness of 2.32 nm. This RMS surface roughness decreases with the increase of wt % of Cu₂S in the photoactive blend and further increases after some optimum concentration of Cu₂S in the blend. Similar trend has been observed in the previous studies related to incorporation of the NCs in OSCs [47]. The values of RMS surface roughness for different concentration of Cu₂S viz. 2 wt %, 4 wt %, 6 wt % and 8 wt % blends are found to be 2.18 nm, 2.09 nm, 1.83 nm and 1.99 nm respectively. Fig. 7(b) and (c) represents the 3D height images of the film made up of blend with 6 wt % and 8 wt % Cu₂S NCs while other images are attached in supplementary information (S1). This change in the trend of surface roughness of the film with 8 wt % Cu₂S in the photoactive blend hampers the performance of the cell and supports the hypothesis of the agglomeration of Cu₂S in the blend.



Fig. 7 AFM height images of the films made from the photoactive blend of PBDB-T:Cu₂S:ITIC with (a) 0 wt % Cu₂S NCs, (b) 6 wt % Cu₂S NCs and (c) 8 wt % Cu₂S NCs.

4. Conclusion:

We have successfully demonstrated Cu₂S NCs based non-fullerene ternary polymer solar cells. The devices were fabricated in an inverted geometry having a structure ITO /ZnO/PBDB-T: Cu₂S NCs: ITIC /MoO₃/Ag. It has been found that addition of Cu₂S NCs improves the performance parameters and PCE. PCE of ~9.6 % has been achieved for the devices with 6 wt % of Cu₂S NCs. The improvement in the performance parameters has been explained on the basis of the light intensity dependent photo-EIS measurements which suggest that there are less trap-assisted recombination in the case of best-performing device (Cu₂S NCs 6 wt %) due the facilitation of charge transfer from PBDB-T to ITIC through Cu₂S NCs.

Acknowledgments

GL thanks Dr. Bharat Kale, Director, Center for Materials for Electronics Technology (C-MET), Pune and Dr. Sudhir Arbuj, Scientist (C-MET, Pune) for their inputs in the synthesis of Cu₂S nanocrystals. GL also thanks management of Shiksha Mandal, Wardha and Principal, Jankidevi Bajaj College of Science (Autonomous), Wardha for providing central instrumentation facility to characterize the material. All the authors agreed on the results and given approval to the manuscript. The authors declare that there is no conflict of interest regarding the publication of this paper.

References

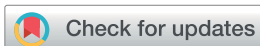
- [1] B. Oregan, M. Gratzel, *Nature* 353 (1991) 737.
- [2] G. Yu, J. Gao, J.C. Hummelen, F. Wudl, A.J. Heeger, *Science* 270 (1995) 1789.
- [3] M.M. Lee, J. Teuscher, T. Miyasaka, T.N. Murakami, H.J. Snaith, 338 (2012) 643.
- [4] J.H. Noh, S.H. Im, J.H. Heo, T.N. Mandal, S.I. Seok, *Nano Lett* 13 (2013) 1764.
- [5] N. Jain, N. Chandrasekaran, A. Sadhanala, R.H. Friend, C.R. McNeill, D. Kabra, *J Mater Chem A* 5 (2017) 24749.
- [6] A.K. Kyaw, D.H. Wang, V. Gupta, J. Zhang, S. Chand, G.C. Bazan, A.J. Heeger, *Adv Mater* 25 (2013) 2397.
- [7] V. Gupta, A.K. Kyaw, D.H. Wang, S. Chand, G.C. Bazan, A.J. Heeger, *Sci Rep-Uk* 3 (2013).
- [8] J.F. Yan, B.R. Saunders, *Rsc Adv*, 4 (2014) 43286.
- [9] S. Gunes, H. Neugebauer, N.S. Sariciftci, *Chem Rev* 107 (2007) 1324.

- [10] G. Dennler, R. Gaudiana, C.J. Brabec, *Abstr Pap Am Chem S* 238 (2009).
- [11] Y.H. Liu, J.B. Zhao, Z.K. Li, C. Mu, W. Ma, H.W. Hu, K. Jiang, H.R. Lin, H. Ade, H. Yan, *Nat Commun* 5 (2014).
- [12] W.C. Zhao, D.P. Qian, S.Q. Zhang, S.S. Li, O. Inganäs, F. Gao, J.H. Hou, *Adv Mater*, 28 (2016) 4734.
- [13] Y.Z. Lin, J.Y. Wang, Z.G. Zhang, H.T. Bai, Y.F. Li, D.B. Zhu, X.W. Zhan, *Adv Mater*, 27 (2015) 1170.
- [14] Z.C. He, B. Xiao, F. Liu, H.B. Wu, Y.L. Yang, S. Xiao, C. Wang, T.P. Russell, Y. Cao, *Nat Photonics* 9 (2015) 174.
- [15] Q.Q. Pan, S.B. Li, Y. Wu, Y. Geng, M. Zhang, Z.M. Su, *Org Electron* 53 (2018) 308.
- [16] Y.K. Yang, Z.G. Zhang, H.J. Bin, S.S. Chen, L. Gao, L.W. Xue, C. Yang, Y.F. Li, *J Am Chem Soc*, 138 (2016) 15011.
- [17] W.C. Zhao, S.S. Li, H.F. Yao, S.Q. Zhang, Y. Zhang, B. Yang, J.H. Hou, *J Am Chem Soc* 139 (2017) 7148.
- [18] F.W. Zhao, S.X. Dai, Y.Q. Wu, Q.Q. Zhang, J.Y. Wang, L. Jiang, Q.D. Ling, Z.X. Wei, W. Ma, W. You, C.R. Wang, X.W. Zhan, *Adv Mater* 29 (2017).
- [19] X. Xu, T. Yu, Z. Bi, W. Ma, Y. Li, Q. Peng, *Adv Mater*, 30 (2018) 1703973.
- [20] L. Meng, Y. Zhang, X. Wan, C. Li, X. Zhang, Y. Wang, X. Ke, Z. Xiao, L. Ding, R. Xia, *Science* (2018) 2612.
- [21] Y. Cui, H.F. Yao, B.W. Gao, Y.P. Qin, S.Q. Zhang, B. Yang, C. He, B.W. Xu, J.H. Hou, *J Am Chem Soc*, 139 (2017) 7302.
- [22] M.M. Li, K. Gao, X.J. Wan, Q. Zhang, B. Kan, R.X. Xia, F. Liu, X. Yang, H.R. Feng, W. Ni, Y.C. Wang, J.J. Peng, H.T. Zhang, Z.Q. Liang, H.L. Yip, X.B. Peng, Y. Cao, Y.S. Chen, *Nat Photonics* 11 (2017) 85.
- [23] J.Q. Zhang, Y.J. Zhang, J. Fang, K. Lu, Z.Y. Wang, W. Ma, Z.X. Wei, *J Am Chem Soc* 137 (2015) 8176.
- [24] Y.J. Zhang, D. Deng, K. Lu, J.Q. Zhang, B.Z. Xia, Y.F. Zhao, J. Fang, Z.X. Wei, *Adv Mater* 27 (2015) 1071.
- [25] Q.S. An, F.J. Zhang, J. Zhang, W.H. Tang, Z.B. Deng, B. Hu, *Energ Environ Sci* 9 (2016) 281.

- [26] R. Sharma, H. Lee, V. Gupta, H. Kim, M. Kumar, C. Sharma, S. Chand, S. Yoo, D. Gupta, *Org Electron* 34 (2016) 111.
- [27] L.Y. Lu, M.A. Kelly, W. You, L.P. Yu, *Nat Photonics* 9 (2015) 491.
- [28] R. Yu, H. Yao, J. Hou, *Advanced Energy Materials* 1702814-n/a.
- [29] H.C. Liao, C.S. Tsao, T.H. Lin, M.H. Jao, C.M. Chuang, S.Y. Chang, Y.C. Huang, Y.T. Shao, C.Y. Chen, C.J. Su, U.S. Jeng, Y.F. Chen, W.F. Su, *Acs Nano* 6 (2012) 1657.
- [30] S.R. Gollu, R. Sharma, G. Srinivas, S. Kundu, D. Gupta, *Org Electron*, 15 (2014) 2518.
- [31] R. Sharma, S. Bhalerao, D. Gupta, *Org Electron*, 33 (2016) 274.
- [32] B.J. Richardson, L.Z. Zhu, Q.M. Yu, *Sol Energ Mat Sol C*, 116 (2013) 252.
- [33] C.Y. Liu, Z.C. Holman, U.R. Kortshagen, *Nano Lett* 9 (2009) 449.
- [34] G. Itskos, A. Othonos, T. Rauch, S.F. Tedde, O. Hayden, M.V. Kovalenko, W. Heiss, S.A. Choulis, *Advanced Energy Materials* 1 (2011) 802.
- [35] M.T. Khan, A. Kaur, S.K. Dhawan, S. Chand, *J Appl Phys* 110 (2011).
- [36] Y. Wu, C. Wadia, W.L. Ma, B. Sadtler, A.P. Alivisatos, *Nano Lett* 8 (2008) 2551.
- [37] Y.M. Sun, J.H. Seo, C.J. Takacs, J. Seifert, A.J. Heeger, *Adv Mater* 23 (2011) 1679.
- [38] S. Li, H.Z. Wang, W.W. Xu, H.L. Si, X.J. Tao, S.Y. Lou, Z.L. Du, L.S. Li, *J Colloid Interf Sci*, 330 (2009) 483.
- [39] M. Wright, A. Uddin, *Sol Energ Mat Sol C*, 107 (2012) 87.
- [40] H.X. Zhou, L.Q. Yang, S. Stoneking, W. You, *Acs Appl Mater Inter* 2 (2010) 1377.
- [41] Z.T. Liu, M.F. Lo, H.B. Wang, T.W. Ng, V.A.L. Roy, C.S. Lee, S.T. Lee, *Appl Phys Lett*, 95 (2009) 227.
- [42] W.L. Leong, S.R. Cowan, A.J. Heeger, *Advanced Energy Materials* 1 (2011) 517.
- [43] P.P. Boix, J. Ajuria, R. Pacios, G. Garcia-Belmonte, *J Appl Phys* 109 (2011) 074514.
- [44] A. Guerrero, N.F. Montcada, J. Ajuria, I. Etxebarria, R. Pacios, G. Garcia-Belmonte, E. Palomares, *J Mater Chem A* 1 (2013) 12345.
- [45] T.M. Clarke, C. Lungenschmied, J. Peet, N. Drolet, A.J. Mozer, *Advanced Energy Materials* 5 (2015) 1401345.
- [46] R. Sharma, V. Gupta, H. Lee, K. Borse, R Datt , C. Sharma, M. Kumar, S. Yoo, D. Gupta, *Organic Electronics* 62 (2018) 441.
- [47] B.J. Richardson, L. Zhu, Q. Yu, *Solar Energy Materials and Solar Cells*, 116 (2013) 252.

- Nanocrystals based non-fullerene ternary organic solar cells.
- PCE improves from 8.24% to 9.53% for optimum concentration of Cu₂S NCs.
- Reason for enhancement in the performance parameters is investigated by photo-EIS and AFM.

ACCEPTED MANUSCRIPT



Cite this: *RSC Adv.*, 2019, 9, 7457

Enhanced performance of PTB7-Th:PCBM based active layers in ternary organic solar cells†

Govinda Lakhotiya,^{*ab} Namdeo Belsare,^b Sudhir Arbuj,^c Bharat Kale^{bc} and Abhimanyu Rana^{td}

The present study aims at understanding the role of incorporating Cu₂S nanocrystals (NCs) as a third component in ternary organic solar cells. Ternary photoactive blends consisting of conjugated polymer poly[4,8-bis(5-(2-ethylhexyl)thiophen-2-yl)benzo[1,2-*b*;4,5-*b'*]dithiophene-2,6-diyl-*alt*-(4-(2-ethylhexyl)-3-fluorothiopheno[3,4-*b*]thiophene)-(2-carboxylate-2-6-diyl)] (PTB7-Th), fullerene derivative phenyl-C₇₁-butyric acid methyl ester (PCBM) and different wt% of Cu₂S NCs were formulated and were employed to fabricate ternary OSCs having a device architecture of ITO/ZnO/PTB7-Th:Cu₂S NCs:PCBM/MoO₃/Ag. It has been observed that with the addition of 3 wt% of Cu₂S NCs, an improved power conversion efficiency (PCE) of 8.20% is obtained against the PCE of 6.96% for reference devices. EIS measurements and AFM studies suggests that the presence of Cu₂S NCs facilitates formation of cascading energy levels, provides smoother surfaces and helps in suppressing trap-assisted recombination.

Received 28th October 2018
 Accepted 21st February 2019

DOI: 10.1039/c8ra08919a

rsc.li/rsc-advances

1. Introduction

Fabrication of bulk heterojunction ternary organic solar cells (OSCs) using ternary photoactive blends is considered as one of the recent strategies to overcome the two well-known major impediments in restricting the power conversion efficiency (PCE) of OSCs, *i.e.* narrow band gap of the donor polymer and poor mobility of carriers in both donor polymers and fullerene-based acceptors.¹⁻⁴ It has been demonstrated that with the addition of the right third component in the binary photoactive blend, it is possible to enhance the absorption of photons, to improve the charge collection, and to do both.⁴⁻⁶ For this, as of now various materials including additional donor polymer/acceptor polymer/sensitizer (dye/metal, semiconductors and dielectric NCs)/high mobility polymers have been studied as a third component.⁷⁻¹⁰ Most of these materials except semiconducting NCs, are found to be capable of either enhancing the absorption of photon or improving the charge collection and not both. Some recent studies have suggested that the use of semiconducting NCs as a third component can simultaneously enhance both photon harvesting and charge collection.¹¹⁻¹⁵ Importance of semiconducting NCs can be understood from the fact that they have

tunable band-gaps which can be tuned to make it complimentary to the absorption of donor polymer and high charge carrier mobility and excellent charge transport properties which can certainly improve the charge collection.¹⁶⁻¹⁸ Further, easy way of synthesis of semiconducting NCs using solution chemistry like wet-chemical synthesis and microwave synthesis is certainly helping to realize the goal of fabricating high PCE OSCs using screen printing, inkjet printing and roll-to-roll printing, and adaptability to flexible plastic substrates.¹⁹⁻²³

In the past, many metallic and semiconducting NCs have been added in ternary photoactive blends of P3HT and PCBM giving the PCE less than 5% in most of the cases.²⁴⁻³² Some of the best known reported PCE of reference cell and best performing device upon the addition of optimum concentration of CdSe, CdS, CdTe, ZnO, Cu₂S and FeS₂ was found to be 3.5% and 4.2%, 0.74% and 0.95%, 0.72% and 0.79%, 2.78% and 3.39%, 1.46% and 3.39% and 2.37% and 2.89% respectively.²⁴⁻³² Recently, Sharma *et al.*³³ have demonstrated the use of microwave synthesized CdS nanoparticles in one of the efficient photoactive blend matrix consisting of PTB7:PCBM highlighting the increased PCE of OSCs from 6.44% to 7.14% upon the addition of optimum concentration of CdS nanoparticles. Although this is good PCE when compared to the previously reported P3HT:PCBM based ternary photoactive blend but it involves the use of toxic, hazardous and rare earth elements like cadmium and therefore can not be used for large scale fabrication.

In the present study, we have demonstrated the fabrication of high efficiency ternary OSCs by employing Cu₂S NCs as third component in one of the well-studied photoactive blend comprised of conjugated polymer PTB7-Th (poly[4,8-bis(5-(2-

^aDepartment of Physics, Jankidevi Bajaj College of Science, Wardha 442001, India. E-mail: lakhotiya.govinda@gmail.com

^bDepartment of Physics, Vidyabharati Mahavidyalaya, Amravati 444602, India

^cCentre for Materials for Electronics Technology, Panchwati, Off Pashan Road, Pune 411008, India

^dSchool of Engineering and Technology, BML Munjal University, Gurgaon 122413, India. E-mail: rana.abhimanyu@gmail.com

† Electronic supplementary information (ESI) available. See DOI: 10.1039/c8ra08919a



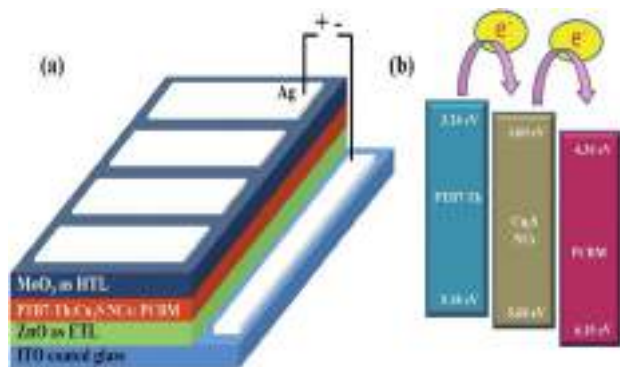


Fig. 1 (a) Schematic highlighting device architecture ITO/ZnO/PTB7-Th:Cu₂S NCs:PCBM/MoO₃/Ag (b) energy levels of materials used in the solar cell device.

ethylhexyl)thiophen-2-yl)benzo[1,2-*b*;4,5-*b'*]dithiophene-2,6-diyl-*alt*-(4-(2-ethylhexyl)-3-fluorothiopheno[3,4-*b'*]thiophene)-(2-carboxylate-2-6-diyl)) and fullerene derivative PCBM (phenyl-C₇₁-butyric acid methyl ester). Apparently, Cu₂S consists of earth abundant and eco-friendly elements and also exhibit unusual properties such as high thermal and photo-chemical stability, broad absorption up to near IR range, high fluorescence quantum yields, high charge carrier mobilities and high electron affinities.^{34,35} Moreover, conduction band of Cu₂S is located around 3.60 eV and lies between the LUMO of donor polymer PTB7-Th and

fullerene acceptor PCBM.^{35,36} Thus, it is expected to form type II heterojunction with PTB7-Th and PCBM and can act as an electron cascade between them. This makes it more promising and interesting for this photoactive blend in comparison to other semi-conducting NCs. However, to the best of our knowledge, there is no report on using Cu₂S as a third component with PTB7-Th:PCBM polymers based OSCs. Here, we have studied the role of Cu₂S NCs as third component by varying the concentration of Cu₂S NCs in the photoactive blend of PTB7-Th:PCBM. With the inverted geometry of the devices and the addition of optimum wt% of Cu₂S NCs, improved PCE of 8.20% is obtained as against the 6.96% for reference device. The obtained results are explained by electrochemical impedance spectroscopy (EIS) and atomic force microscopy (AFM) studies.

2. Experimental

2.1 Synthesis of Cu₂S NCs

The synthesis of copper(i) sulfide nanocrystals (NCs) was performed using hot injection technique whose protocol was developed by Alivisatos *et al.*³⁴ It deals with the chemistry of copper(II) acetylacetonate and ammonium diethyldithiocarbamate in a mixed solvent of dodecanethiol and oleic acid whose detailed procedure can be found somewhere else.³⁴ Isopropanol and toluene were used for washing to get the precipitate of required NCs and were centrifuged with 5000 rpm for 10 min.

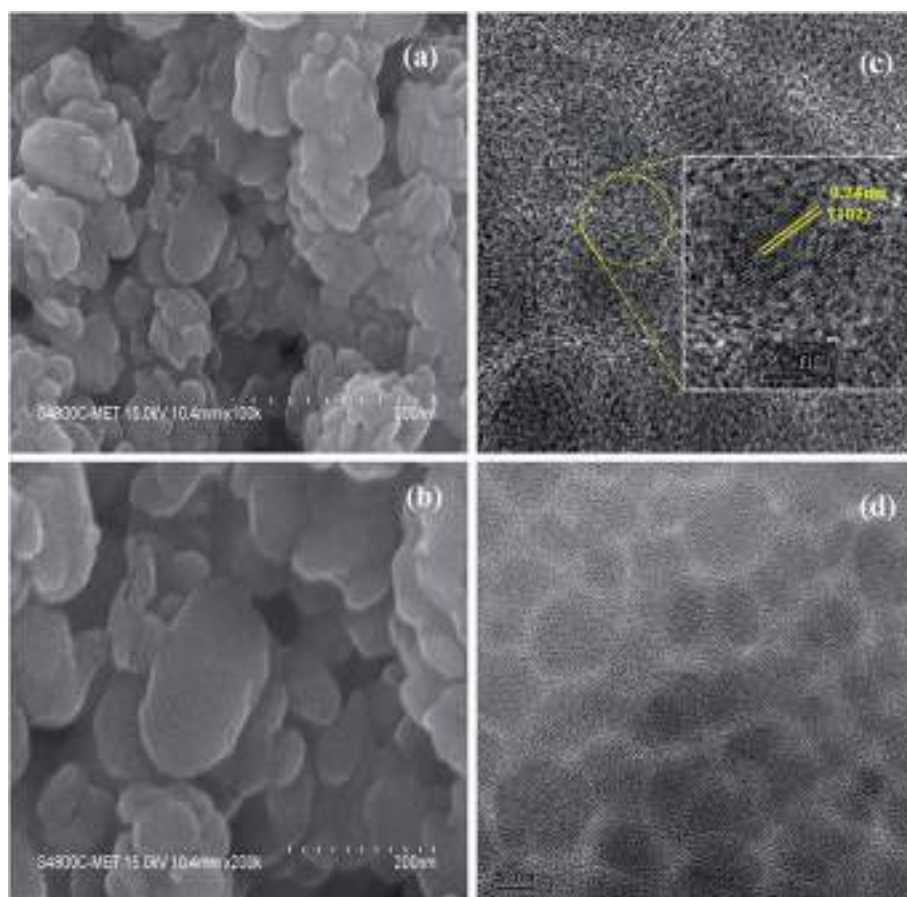


Fig. 2 (a and b) FESEM images and (c and d) HRTEM images of as synthesized Cu₂S NCs.



2.2 Material characterization and device fabrication

For morphological studies, we have analyzed field emission scanning electron microscope (FESEM) images and high resolution transmission electron microscopy (HRTEM) images at different magnification. FESEM images were recorded using Hitachi's (S4800) field emission electron microscope which was operated at 30 kV and HRTEM images were recorded using JEOL FS2200-FEG operating at 200 kV. Cu₂S nanocrystals (NCs) were also characterized for its phase purity by X-ray diffraction (XRD) technique using Rigaku's Miniflex 600 X-ray diffractometer which was operated at 40 kV and 30 mA using Cu K_α X-rays (1.54 Å). Optical property of Cu₂S NCs was studied using UV-vis absorption spectrophotometer using Shimadzu 1800.

Devices were fabricated as per the schematic shown in the Fig. 1(a) and involves depositions of different layers. Mainly PTB7-Th, PCBM and Cu₂S NCs based binary/ternary photoactive layer was sandwiched between the ZnO (an electron transport layer) and MoO₃ (a hole transport layer). A pre-cleaned and patterned ITO coated glass substrates is used as a transparent substrate. Sol-gel synthesized ZnO was spin coated over ITO at 2000 rpm for 30 s and annealed at 200 °C for 15 min to obtain a film of ~40 nm.¹⁵ Photoactive blend is prepared using PTB7-Th (10 mg), PCBM (15 mg) and varying amount of Cu₂S NCs in 1 ml of chlorobenzene (CB) with 3% v/v of 1,8 diiodooctane (DIO) solvent. Ternary blend was subjected to vigorous overnight stirring at 50 °C in the dark before being spin coated over the ZnO layer.^{15a} For ternary photoactive blend, some amount of PCBM is replaced by the equal amount of Cu₂S NCs. Photoactive blends were spin-coated at 1200 rpm for 60 s to obtain a film of thickness ~100 nm and was allowed to dry for 2 h. At last, 10 nm MoO₃ layer as a hole transport layer and 100 nm Ag electrode as an anode was deposited by thermal evaporation. Keithley 2600 source meter and a Newport solar simulator (model number 91160) with AM 1.5G spectral distribution at 1000 W m⁻² intensity was used for *J-V* characteristics of the fabricated devices. Bentham's PVE300 was used for external quantum efficiency (EQE) spectra of the devices where the active device area was fixed to 7 mm². Atomic force microscopy (AFM) of the films of photoactive blends with the different wt% of Cu₂S NCs was carried out using Nanosurf's C 3000 model. The EIS studies were carried out using electrochemical work station. The frequency range was swept from 1 MHz to 1 Hz and 20 mV and AC signal was superimposed with various DC applied bias voltage.

3. Results and discussion

The schematic of full device configuration is shown in the Fig. 1(a) and the positions of conduction band and valance band of Cu₂S NCs with respect to HOMO and LUMO levels of donor polymer PTB7-Th and acceptor polymer PCBM has been shown in Fig. 1(b). To confirm the morphology, phase purity, crystal structure and optical properties of the synthesized Cu₂S NCs, we have recorded the FESEM and HRTEM images, XRD pattern and UV-vis absorption spectra. Fig. 2a-d shows FESEM and HRTEM images at two different magnifications. The

recorded images suggest that the protocol used for the synthesis of NCs has yielded dumbbell shaped NCs having length and diameter less than 20 nm. An inter-layer spacing of 0.198 nm and 0.24 nm, as can be seen in the high magnification HRTEM image (Fig. 2(c)), corresponds to (110) and (102) planes of Cu₂S NCs respectively. XRD pattern and UV-vis absorption spectra shown in the Fig. S1(a and b)† confirms that the as synthesized NCs are phase pure and have wide absorption spectrum UV-vis-NIR region. This is in close agreement with the previous studies.^{28,34} Current density *versus* voltage (*J-V*) characteristics used for the calculation of power conversion efficiency (PCE) of fabricated solar cell is shown in Fig. 3(a) and the corresponding external quantum efficiency (EQE) spectra is shown in Fig. 3(b). Various device parameters such as open circuit voltage (*V*_{oc}), short-circuit current (*J*_{sc}), fill factors (FF) and PCE with different wt% of Cu₂S NCs blended in PTB7-Th:Cu₂S NCs:PCBM ternary OSCs is summarized in Table 1.

As can be seen in the Table 1, for all the wt% of Cu₂S NCs, there is very negligible change in the *V*_{oc}. To explain this, it is necessary to understand the origin of *V*_{oc}. It is well known that the *V*_{oc} mainly depends on the energy difference between the HOMO of the donor polymer and the LUMO of the acceptor polymer. In the present study, for all the composition of the

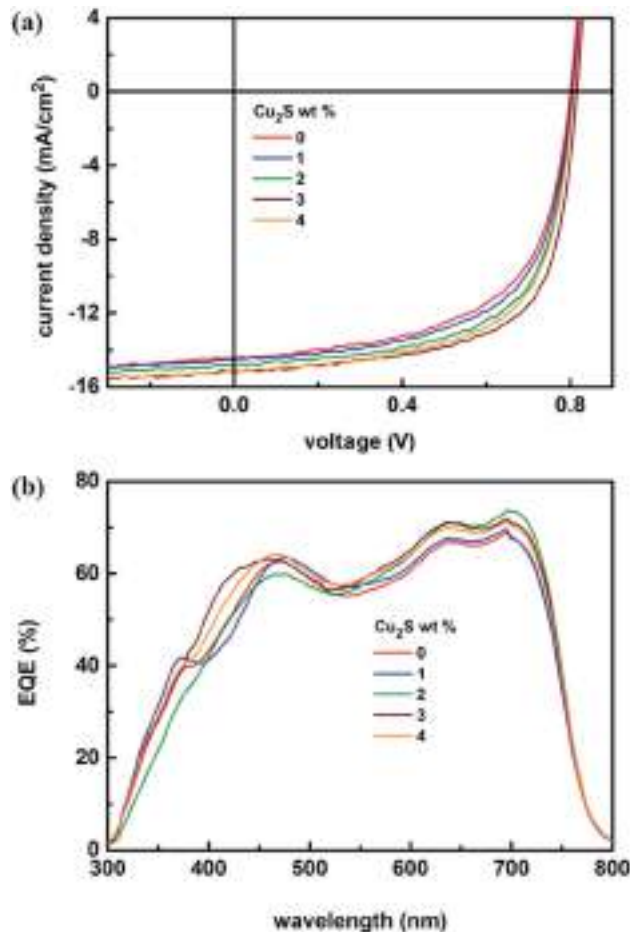


Fig. 3 (a) *J-V* characteristics under illumination (AM 1.5G, one sun) and (b) EQE spectra of PTB7-Th:Cu₂S NCs:PCBM ternary OSCs with different wt% of Cu₂S NCs.



Table 1 Summary of J - V characteristics of PTB7-Th:Cu₂S NCs:PCBM devices with different wt% of Cu₂S NCs

Cu ₂ S NCs wt%	V _{oc} (mV)	Measured J_{sc} (mA cm ⁻²)	Calculated J_{sc}^a (mA cm ⁻²)	FF (%)	PCE best ^b (%)
0%	803	14.44	15.07	59.95	6.96 (6.85)
1%	803	14.58	14.59	61.73	7.23 (7.18)
2%	803	14.86	14.88	63.75	7.61 (7.52)
3%	818	15.17	15.20	66.10	8.20 (8.11)
4%	803	15.05	15.48	64.95	7.85 (7.76)

^a Calculated from EQE data. ^b Average of the five devices.

ternary photoactive blend, added wt% of Cu₂S NCs is very small as compared to the donor PTB7-Th and acceptor PCBM and therefore it is most likely that at most of the interfaces within the nano-morphology of the photoactive blend, interpenetrating networks of PTB7-Th and PCBM are in direct contact with each other. As a result, the V_{oc} remains nearly same for all the composition. However, the scenario is different in the case of the J_{sc} and FF. It is observed that both J_{sc} and FF increases with the increase in the wt% of Cu₂S NCs. This trend is observed till the concentration of Cu₂S NCs reaches its optimum value of 3 wt% and fabricated ternary device has demonstrated the PCE of 8.20% as against the PCE of 6.96% for reference device. This dramatic increase in the J_{sc} and FF and therefore the PCE can be justified by using the theory of charge transfer complex (CTC).³⁷ It might be possible that the added Cu₂S NCs located at the interface of

PTB7-Th and PCBM may get bind with PTB7-Th:PCBM *via* dipole-dipole interaction and form a charge transfer complex (CTC).³⁸ This is due to the formation of the electron cascade structure arises out of the well-placed conduction band of the Cu₂S between LUMO of donor polymer PTB7-Th and acceptor polymer PCBM. Also, it might be possible that presence of the Cu₂S NCs in the photoactive blend provides additional energetically favorable interfaces necessary for the exciton diffusion and formation of CT states. However, when the Cu₂S NCs concentration was further increased in the ternary photoactive blend, there is possibility that Cu₂S NCs might have agglomerated. This agglomeration might have decreased the additional energetically favorable interfaces thereby seriously affecting the process of exciton diffusion and CT states formation. As a result, it was observed that there is a decrease in the J_{sc} and FF and therefore

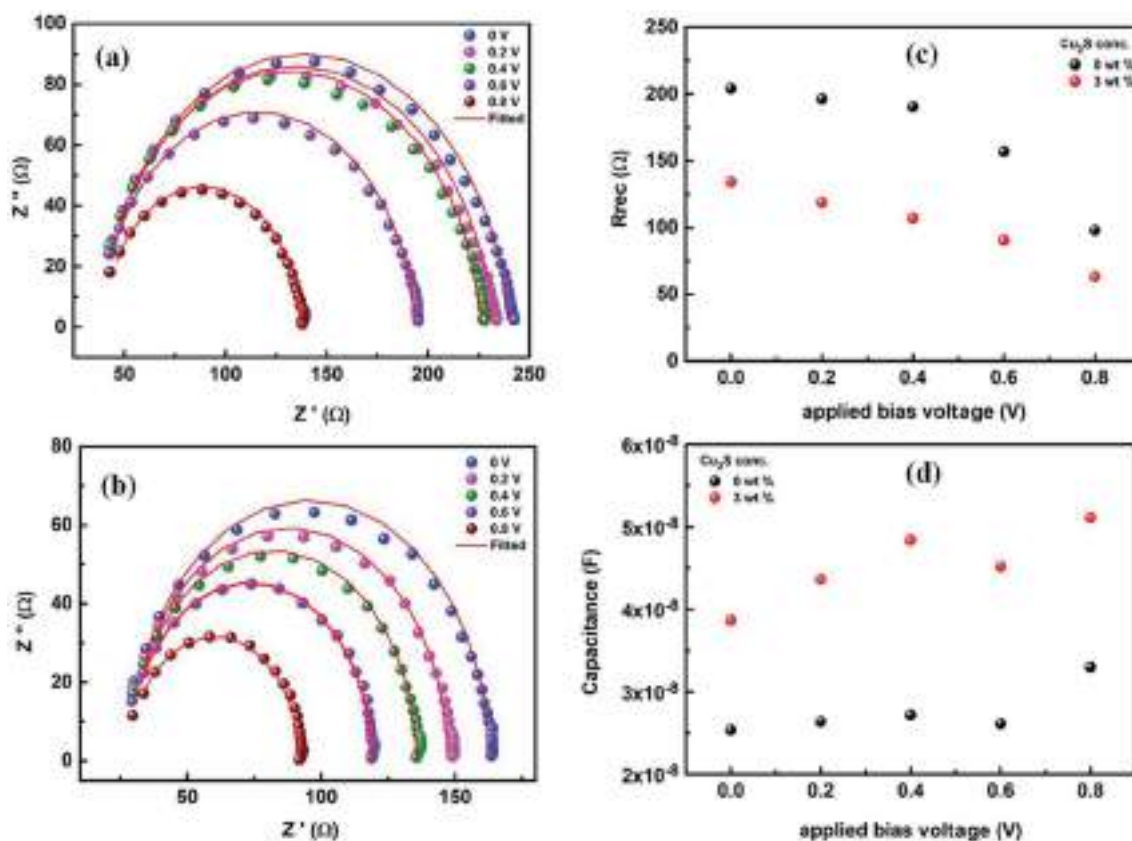


Fig. 4 (a) and (b) Nyquist plots of PTB7-Th:Cu₂S NCs:PCBM ternary OSCs with 0 and 3 wt% of Cu₂S NCs respectively at different applied bias voltage (c) recombination resistance (R_{rec}) and (d) chemical capacitance (C_{μ}) as a function of applied bias voltage for devices with 0 and 3 wt% of Cu₂S NCs.



the PCE. A similar trend was observed in the case of EQE spectra. The calculated values of J_{sc} from EQE are shown in the Table 1. Here, it is worth mentioning that the encapsulated ternary devices were quite stable for one month without significant change in the performance. We have also fabricated the PTB7-Th:Cu₂S NCs based binary device but found that the binary film of PTB7-Th:Cu₂S was very rough and comprised of so many pinholes. Thus, most of the fabricated devices got short and only few of them were measurable. Few of the measurable devices yielded PCE < 1%. Therefore, this data has not been included in the manuscript. FF and J_{sc} is found to be highly compromised in these devices. It might be due to the poor dispersion of higher concentration of Cu₂S NCs (15 mg ml⁻¹) in PTB7-Th matrix which might have tend to agglomerate to form scattering centers.

To get further insight about the improved performance parameters of the ternary OSCs with optimum wt% (3%) of Cu₂S NCs, EIS and AFM studies were carried out. Fig. 4(a) shows the Nyquist plots for both reference device (Cu₂S NCs, 0 wt%) as well as the best performing device (Cu₂S NCs, 3 wt%) respectively. It is observed that for both the systems, EIS spectra comprised of only one semi-circle. Therefore, they can be fitted by a simple R_{rec} , C_{μ} equivalent circuit, where R_{rec} is a recombination resistance (R_{rec}) and C_{μ} is the chemical capacitance (C_{μ}). However, as can be noticed, in both the cases, obtained Nyquist plots are not perfect semi-circles. This truncated semi-circle arises mainly due to the spatial inhomogeneity within the photoactive layer. This has to be taken into consideration and

therefore for fitting purpose the capacitor element is replaced by constant phase elements (CPE).³⁹ Impedance for an ideal capacitor and CPE is given by eqn (1) and (2) respectively.⁴⁰ From above equations, it is apparent that CPE is equivalent to capacitance if P equals 1.

$$Z_C = 1/i\omega c \quad (1)$$

$$Z_{CPE} = 1/CPE(i\omega)^P \quad (2)$$

$$n = \frac{1}{e} \int_0^{V_{oc}} C_{\mu}(V)dv \quad (3)$$

After fitting, values of recombination resistance and chemical capacitance is obtained and is further used to calculate the value of carrier density using eqn (3). Response time representative of the recombination processes is calculated from the characteristic frequency (ω) at the top of the arc, where $2\pi\omega = 1/\tau$.^{40,41} It is observed that for both the system recombination lifetime lies in order of 10⁻⁶ s. Further, as can be seen in Fig. 4(c), recombination resistance is less in case of best performing device (Cu₂S NCs, 3 wt%) when compared to reference device (Cu₂S NCs, 0 wt%). Additionally, using eqn (3), we have calculated the charger carrier density (n) for both the systems using the capacitance values shown in Fig. 4(d). It is found that carrier densities for best performing device (Cu₂S NCs, 3 wt%) and reference device (Cu₂S NCs, 0 wt%) at 0.8 V is $\sim 5 \times 10^{17}$

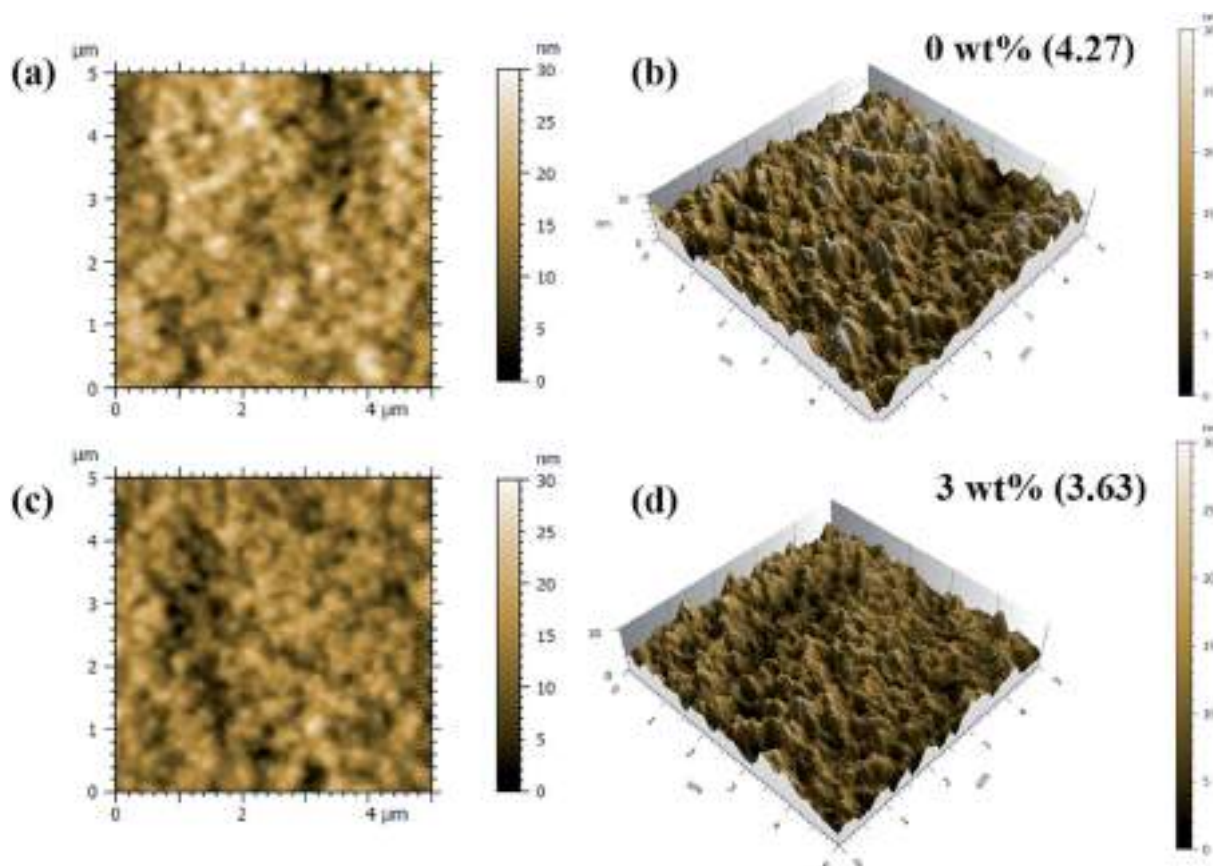


Fig. 5 2D and 3D AFM images of the films of PTB7-Th:Cu₂S NCs:PC₇₀BM photoactive blend with (a and b) 0 wt% (c and d) 3 wt% of Cu₂S NCs.



cm^{-3} and $\sim 3 \times 10^{17} \text{ cm}^{-3}$ respectively. Higher charge carrier density for the best performing device (Cu_2S NCs, 3 wt%) suggest that the charge collection is more efficient in this system. Thus, it can be said that the presence of Cu_2S NCs helps in improving the charge transfer and charge collection by providing electron cascade. This increase in the J_{sc} and FF and therefore the PCE supports the theory of charge transfer complex (CTC)³⁷ wherein the formation of the electron cascade structure of the well-placed conduction band of the Cu_2S NCs between LUMO of donor polymer PTB7-Th and PCBM polymer plays a vital role. Also, it might be possible that the presence of Cu_2S NCs in the photoactive blend provides additional energetically favorable interfaces necessary for the exciton diffusion and formation of CT states.

AFM studies of the spin casted films of binary and ternary photoactive blends was carried out and 2D and 3D images are shown in the Fig. 5 and S2.† As can be seen, films are quite smooth and does not have any pin-holes. The rms values of surface roughness are found to decrease from $\sim 4.27 \text{ nm}$ for the films with 0 wt% of Cu_2S NCs to $\sim 3.63 \text{ nm}$ for the films with 3 wt% of Cu_2S NCs. However, with the further increase in the concentration of Cu_2S NCs, rms surface roughness increases to 3.77 nm . This might be due to the possibility of inhomogeneous distribution/agglomeration of Cu_2S NCs in the matrix. Accordingly, this has decreased the additional energetically favorable interfaces thereby affecting the process of exciton diffusion and CT states formation. The shielding effect could be due to the higher concentration of NCs which inherently affects the transport of electron in the matrix. This might have increased the charge carrier recombination which ultimately reduces the PCE.

4. Conclusion

In conclusion, role of Cu_2S NCs as third component in ternary OSCs has been successfully investigated by varying the concentration of Cu_2S NCs in ternary photoactive blend comprised of PTB7-Th, PCBM and Cu_2S NCs. Fabricated ternary OSCs having a device architecture ITO/ZnO/PTB7-Th: Cu_2S NCs:PCBM/ MoO_3 /Ag has shown the improved PCE of 8.20% as against the PCE of 6.96% for the reference device. The improvement in the performance parameters has been explained on the basis of the EIS measurements and AFM studies which suggest that presence of Cu_2S NCs facilitates formation of cascading energy levels and thus helps in suppressing trap-assisted recombination.

Conflicts of interest

Authors declare no conflict of interest.

Acknowledgements

GL thanks Principal, Jankidevi Bajaj College of Science, Wardha and Principal, Vidyabharti College for providing instrumentation facility for the work. AR thanks VC, BML Munjal University, Gurgaon for providing the facilities for this work. GL and AR

thank Ramakant Sharma, IIT Bombay for valuable discussion and help.

References

- 1 D. Wöhrle and D. Meissner, *Adv. Mater.*, 1991, **3**, 129–138.
- 2 H. Hoppe and N. S. Sariciftci, *J. Biomed. Mater. Res.*, 2004, **19**, 1924–1945.
- 3 S. Günes, H. Neugebauer and N. S. Sariciftci, *Chem. Rev.*, 2007, **107**, 1324–1338.
- 4 A. Pivrikas, N. S. Sariciftci, G. Juška and R. Österbacka, *Prog. Photovoltaics*, 2007, **15**, 677–696.
- 5 Q. An, F. Zhang, J. Zhang, W. Tang, Z. Deng and B. Hu, *Energy Environ. Sci.*, 2016, **9**, 281–322.
- 6 J. H. Noh, S. H. Im, J. H. Heo, T. N. Mandal and S. I. Seok, *Nano Lett.*, 2013, **13**, 1764–1769.
- 7 T. Ameri, P. Khoram, J. Min and C. J. Brabec, *Adv. Mater.*, 2013, **25**, 4245–4266.
- 8 J. Zhang, Y. Zhang, J. Fang, K. Lu, Z. Wang, W. Ma and Z. Wei, *J. Am. Chem. Soc.*, 2015, **137**, 8176–8183.
- 9 R. Sharma, H. Lee, V. Gupta, H. Kim, M. Kumar, C. Sharma, S. Chand, S. Yoo and D. Gupta, *Org. Electron.*, 2016, **34**, 111–117.
- 10 Y. Zhang, D. Deng, K. Lu, J. Zhang, B. Xia, Y. Zhao, J. Fang and Z. Wei, *Adv. Mater.*, 2015, **27**, 1071–1076.
- 11 F. Ongul, S. A. Yuksel, C. Allahverdi, S. Bozar, M. Kazici and S. Gunes, *Spectrochim. Acta, Part A*, 2018, **194**, 50–56.
- 12 K. Borse, R. Sharma, H. Sagar, P. A. Reddy, D. Gupta and A. Yella, *Org. Electron.*, 2017, **41**, 280–286.
- 13 S. A. Yousaf, M. Ikram and S. Ali, *Appl. Nanosci.*, 2018, **1**, 1–9.
- 14 W. Luan, C. Zhang, L. Luo, B. Yuan, L. Jin and Y.-S. Kim, *Appl. Energy*, 2017, **185**, 2217–2223.
- 15 (a) A. K. Kyaw, X. W. Sun, C. Y. Jiang, G. Q. Lo, D. W. Zhao and D. L. Kwong, *Appl. Phys. Lett.*, 2008, **93**, 221107; (b) C. Li, X. Sun, J. Ni, L. Huang, R. Xu, Z. Li, H. Cai, J. Li, Y. Zhang and J. Zhang, *Sol. Energy*, 2017, **155**, 1052–1058.
- 16 I. Gur, N. A. Fromer, M. L. Geier and A. P. Alivisatos, *Science*, 2005, **310**, 462–465.
- 17 W. U. Huynh, J. J. Dittmer and A. P. Alivisatos, *Science*, 2002, **295**, 2425–2427.
- 18 D. J. Milliron, I. Gur and A. P. Alivisatos, *MRS Bull.*, 2005, **30**, 41–44.
- 19 C. J. Brabec and J. R. Durrant, *MRS Bull.*, 2008, **33**, 670–675.
- 20 X. Peng, J. Yuan, S. Shen, M. Gao, A. S. Chesman, H. Yin, J. Cheng, Q. Zhang and D. Angmo, *Adv. Funct. Mater.*, 2017, **27**(41), 1703704.
- 21 S. I. Na, S. S. Kim, J. Jo and D. Y. Kim, *Adv. Mater.*, 2008, **20**, 4061–4067.
- 22 X. Fan, J. Wang, H. Wang, X. Liu and H. Wang, *ACS Appl. Mater. Interfaces*, 2015, **7**, 16287–16295.
- 23 Y. Lin, H. F. Dam, T. R. Andersen, E. Bundgaard, W. Fu, H. Chen, F. C. Krebs and X. Zhan, *J. Mater. Chem. C*, 2013, **1**, 8007–8010.
- 24 C.-Y. Liu, Z. C. Holman and U. R. Kortshagen, *Nano Lett.*, 2008, **9**, 449–452.
- 25 M. Taukeer Khan, A. Kaur, S. Dhawan and S. Chand, *J. Appl. Phys.*, 2011, **110**, 044509.



- 26 S. R. Gollu, R. Sharma, G. Srinivas, S. Kundu and D. Gupta, *Org. Electron.*, 2014, **15**, 2518–2525.
- 27 H.-C. Liao, C.-S. Tsao, T.-H. Lin, M.-H. Jao, C.-M. Chuang, S.-Y. Chang, Y.-C. Huang, Y.-T. Shao, C.-Y. Chen and C.-J. Su, *ACS Nano*, 2012, **6**, 1657–1666.
- 28 B. J. Richardson, L. Zhu and Q. Yu, *Sol. Energy Mater. Sol. Cells*, 2013, **116**, 252–261.
- 29 G. Itskos, A. Othonos, T. Rauch, S. F. Tedde, O. Hayden, M. V. Kovalenko, W. Heiss and S. A. Choulis, *Adv. Energy Mater.*, 2011, **1**, 802–812.
- 30 W. J. Beek, M. M. Wienk, M. Kemerink, X. Yang and R. A. Janssen, *J. Phys. Chem. B*, 2005, **109**, 9505–9516.
- 31 P. V. Kamat, *J. Phys. Chem. C*, 2008, **112**, 18737–18753.
- 32 M. Choi, H. Fu, W. Luan and Y.-S. Kim, *IEEE Nanotechnol. Mater. Devices Conf.*, 2011, 482–483.
- 33 R. Sharma, S. Bhalerao and D. Gupta, *Org. Electron.*, 2016, **33**, 274–280.
- 34 Y. Wu, C. Wadia, W. Ma, B. Sadtler and A. P. Alivisatos, *Nano Lett.*, 2008, **8**, 2551–2555.
- 35 A. Baray-Calderón, R. Galindo, J. Maldonado, O. Martínez-Alvarez, L. Acosta-Torres, J. Santos-Cruz, J. de la Fuente-Hernández and M. Arenas-Arrocena, *MRS Online Proc. Libr.*, 2015, 1748.
- 36 S. H. Liao, H. J. Jhuo, Y. S. Cheng and S. A. Chen, *Adv. Mater.*, 2013, **25**, 4766–4771.
- 37 F. Bencheikh, D. Duché, C. M. Ruiz, J.-J. Simon and L. Escoubas, *J. Phys. Chem. C*, 2015, **119**, 24643–24648.
- 38 S. Hong, H. Kang, G. Kim, S. Lee, S. Kim, J.-H. Lee, J. Lee, M. Yi, J. Kim and H. Back, *Nat. Commun.*, 2016, **7**, 10279.
- 39 A. Guerrero, N. F. Montcada, J. Ajuria, I. Etxebarria, R. Pacios, G. Garcia-Belmonte and E. Palomares, *J. Mater. Chem. A*, 2013, **1**, 12345–12354.
- 40 T. M. Clarke, C. Lungenschmied, J. Peet, N. Drolet and A. J. Mozer, *Adv. Energy Mater.*, 2015, **5**, 1401345.
- 41 R. Sharma, V. Gupta, H. Lee, K. Borse, R. Datt, C. Sharma, M. Kumar, S. Yoo and D. Gupta, *Org. Electron.*, 2018, **62**, 441–447.



SHORT
COMMUNICATIONS

Proton/Metal–Ligand Stability Constants of Complexes of Sr(II), Cr(II), and Al(III) with *N*-Phthaloyl Aminoacid and Benzimidazole Derivatives in Dioxane–Water Mixture¹

Pradip V. Tekade^{a,*}, Sonal Bajaj^{a,**}, Bhagyashri Tale^{a,***}, Neha R. Titirmare^a, and Priyanka Bandwal^a

^aDepartment of Chemistry, Jankidevi Bajaj College of Science, Jannalal Bajaj Marg, Civil Lines, Wardha, India

*e-mail: pradiptekade@gmail.com

**e-mail: sonulstar@gmail.com

***e-mail: bhagyashritale@gmail.com

Received August 19, 2017

Abstract—Formation of complexes Sr(II), Cr(II), and Al(III) with ligands (1,3-dioxo-1,3-dihydro-2H-isoindol-2-yl)acetic acid (L1), 2-(1-(2-(4-nitrophenyl)-1H-benzo[d]imidazol-1-yl)-1-oxobutan-2-yl)-2,3-dihydroinden-1-one(L2) and 2-(2-(2-(4-chlorophenyl)-1H-benzo [d] imidazol-1-yl)-2-oxoethyl)isoindoline-1,3-dione (L3) investigated using pH metric technique in 70% dioxane-water mixture. Proton ligand formation number and metal-ligand formation number determined. Proton-ligand stability constants pK values and metal – ligand stability constants $\log k$ values evaluated using half integral method. It indicates that Sr(II), Cr(II), and Al(III) metal ions formed 1 : 1 and 1 : 2 complexes with the ligands L1, L2, and L3. These can be of interest for specialists in the field of coordination chemistry.

Keyword: proton–ligand and metal–ligand stability constants, pH-metric study, benzimidazole derivative, Irving–Rossetti expression

DOI: 10.1134/S0036024418120427

INTRODUCTION

Naik et al. [1], El-Gammal et al. [2], Anan et al. [3], Fukada et al. [4], and O'Sullivan et al. [5] reported pH-metric studies of metal complexes. Szpak et al. [6] explained Coordination abilities of *N*-methyl alkyl-aminomethane-1, 1-diphosphonic acids towards zinc(II), magnesium(II), and calcium(II) metal ions. El-Bindary et al. [7] reported thermodynamic studies of azo dye ligand and its metal complexes potentiometrically.

In our ongoing endeavor, we studied Proton/metal–ligand stability constants of complexes of Ni(II), Cu(II), and Co(II) [8, 9]. In continuation to our earlier work, here in this paper we have reported the study of Proton/Metal Ligand Stability Constants of Complexes of Sr(II), Cr(II), and Al(III) with *N*-phthaloyl and benzimidazol derivatives pH metrically.

EXPERIMENTAL PROCEDURE

pH-Measurements carried out with digital pH-meter model Equiptronics EQ-610. The experimental procedure involves pH titration of following 3 sets of

mixtures (keeping total volume constant) against a carbonate free standard alkali.

1. Free acid (0.01 M) titration.
2. Free acid (0.01 M) and ligand (20×10^{-4}) titration.
3. Free acid (0.01 M), ligand (20×10^{-4}) and metal ion (4×10^{-4}), against standard NaOH solution.

The ionic strength of all the solutions maintained constant (0.1 M) by addition of appropriate quantity of 1 M NaClO₄ solution.

- a. Proton-ligand formation numbers $\bar{\eta}A$:

$$\bar{\eta}A = \gamma \frac{(E^0 + N)\Delta V}{(V^0 + V_1)T_L^0},$$

where V^0 is initial volume of solution (50 mL), N is normality of sodium hydroxide, T_L^0 is concentration of ligand in 50 mL solution, E^0 is initial concentration of free acid (HClO₄), γ is number of dissociable protons from ligand, $\bar{\eta}A$ is proton-ligand formation number, $(V_2 - V_1) = \Delta V$ are volumes of alkali consumed by acid and ligand at the same pH.

- b. Proton-ligand formation curves ($\bar{\eta}A$). Formation curves are plotted between $\bar{\eta}A$ and pH The half

¹ The article is published in the original.

integral method employed for the determination of proton-ligand stability constants.

c. Half integral method. The proton-ligand stability constant (pK values) are calculated from formation curve.

d. Metal-ligand formation number ($\bar{\eta}$):

$$\bar{\eta} = \gamma \frac{(E^0 + N)\Delta V}{(V^0 + V_2)T_M^0},$$

where V^0 is initial volume of solution (50 mL), N is normality of sodium hydroxide, T_M^0 is concentration of metal ions, $\bar{\eta}$ is metal-ligand formation number, E^0 is initial concentration of free acid (HClO_4), γ is number of dissociable protons from ligand, $(V_3 - V_2) = \Delta V$ are volumes of alkali consumed by acid and ligand at the same pH.

e. Metal-ligand formation curves. Formation curves are plotted between $\bar{\eta}$ and pH. The metal-ligand stability constants determined by half integral method.

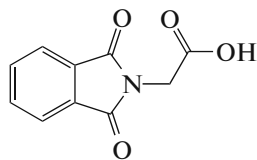
The value of $pL = \log K$ is calculated with the help of following expression.

$$pL = \log \left[\frac{[\text{H}^+]/K_L}{T_L^0 - T_M^0 \bar{\eta}} \right].$$

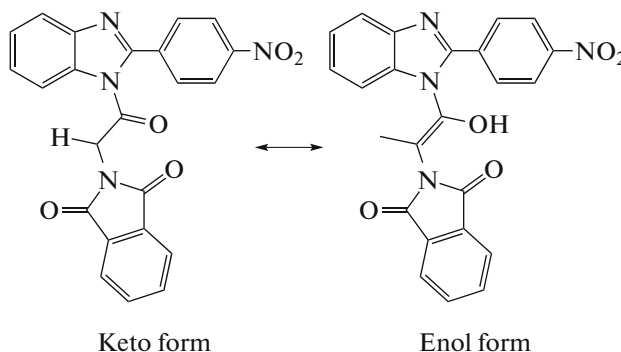
f. Relation between $\log K$ and pK values. The proton-ligand stability constant (pK) and metal-ligand stability constants ($\log K$) used to verify the validity of $\log K = apK + b$ relation. The validity of this relationship tested only for the metal complexes of similar substituted ligands.

Ligands used for this work are:

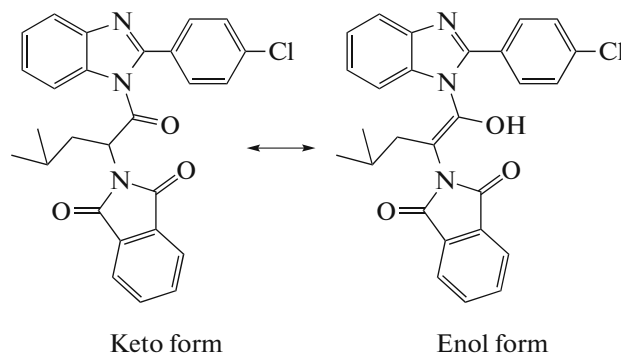
1. (1,3-Dioxo-1,3-dihydro-2H-isoindol-2-yl) acetic acid (*N*-phthaloyl glycine), i.e., L1



2. 2-(1-(2-(4-Nitrophenyl)-1H-benzo[d]imidazol-1-yl)-1-oxobutan-2-yl)-2,3-dihydroinden-1-one, i.e., L2



3. 2-(2-(2-(4-Chlorophenyl)-1H-benzo[d]imidazol-1-yl)-2-oxoethyl)isoindoline-1,3-dione i.e., L3



The values of slope and intercept in present work are not in good agreement. The disagreement may be attributed to the fact that pi electrons donating and accepting properties of cations may not be the only factor which influences slope values. Other factors, such as ionization potential of metal ion, nuclear repulsion between metal ion and donor atoms. Tendency of metal ions to form pi bonds. Ligand field stabilization may influence slope values.

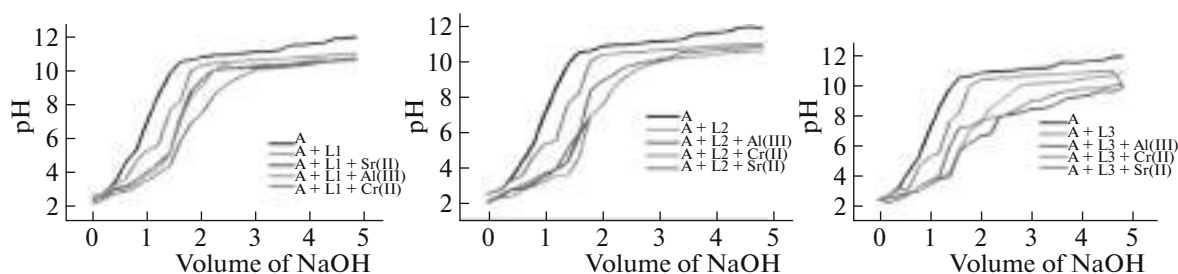


Fig. 1. Acid curve (A), acid-ligand titration curve (A + L) and acid-ligand-metal (Sr(II), Cr(II), and Al(III)) (A + L + M) titration curves for L1, L2, and L3.

Table 1. Proton ligand stability constant for complexes of metal (Sr(II), Cr(II), and Al(III)) with ligands (L1, L2, and L3)

S.N.	System	Constant half p <i>K</i> integral method
1	L1	1.99×10^{-5}
2	L2	1.548×10^{-6}
3	L3	9.332×10^{-6}

RESULTS AND DISCUSSION

A. Free acid titration curve, acid + ligand titration curve, and acid + ligand + metal titration curve. As per Fig. 1, the deviation between free acid titration curve and ligand titration (acid + ligand) curve is conformation of the dissociation of proton/OH group (of –COOH) from ligand L1 and OH group (of enol form) L2 and L3. The deviation between (acid + ligand) curve and (acid + ligand + metal) curve shows the commencement formation of complex. The change of color in the range of pH 2.5 to 7.5, shows the formation of complex.

B. Proton ligand stability constant (p*K*). Table 1 shows the p*K* values (proton–ligand stability constants) calculated from the formation curves between pH vs. $\bar{\eta}A$ by half integral method, which increases in order: L1 > L3 > L2. The difference in p*K* values of two ligands is due to the relative position of the groups in the structure. p*K* value is less in case of L2 may be due to presence of electron withdrawing –NO₂ group. In case of L2 and L3, p*K* value is less than L1 which may be due to steric hindrance.

C. Metal ligand stability constant (log *k*₁ and log *k*₂). Tables 2, 3 show the p*L* values (metal–ligand stability constants) calculated from the formation curves between pH vs. $\bar{\eta}$ by half integral method. Ordinarily log *k*₁ values are greater than log *k*₂ values for all metal complexes except L2–Al(III) complex.

Therefore, L2–Al(III) complex occurred simultaneously, because there is no appreciable difference between log *k*₁ and log *k*₂ values. Rest of the complexes occurred stepwise due to sufficient difference between log *k*₁ and log *k*₂ values increases in the following order:

for Sr(II), L3 > L2 > L1,

for Al(III), L2 > L3 > L1,

for Cr(II), L2 > L3 > L1.

CONCLUSION

The proton–ligand and metal–ligand stability constant of complexes of Sr(II), Cr(II), and Al(III) with *N*-phthaloyl and benzimidazole derivatives pH metrically reported here in 70% dioxane–water mixture.

According to the titration curves, the deviation between acid + ligand (A + L) curve and acid + ligand + metal (A + L + M) curve for all systems started from pH 2.5 to 3. This indicated the commencement of complex formation.

p*K* value is less in case of L2 because of presence of electron withdrawing –NO₂ group. In case of L2 and L3, p*K* value is less than L1 because of steric hindrance. However there is a difference in log *K*₁ and log *K*₂ values which shows the stepwise formation of 1 : 1 and 1 : 2 complexes with all three ligands. The results shows that the ratio of log *K*₁/log *K*₂ is positive in all cases, consequently it leads to the formation of stable complexes. L2–Al(III) complex formation occurred simultaneously, as there is no appreciable difference between log *k*₁ and log *k*₂ values. Rest of the complexes occurred stepwise due to sufficient difference between log *k*₁ and log *k*₂ values; log *k*₁ and log *k*₂ values of Sr(II) are maximum for L3 means Sr(II) forms most stable complex with L3. Conversely log *k*₁ and log *k*₂ values of Cr(II) and Al(III) are maximum

Table 2. Metal–ligand stability constants for complexes of Metal (Sr(II), Cr(II), and Al(III)) with ligands (L1, L2, and L3)

S.N.	System	log <i>k</i> ₁ i.e., p <i>L</i> ₁	log <i>k</i> ₂ i.e., p <i>L</i> ₂	log <i>k</i> ₁ –log <i>k</i> ₂	log <i>k</i> ₁ /log <i>k</i> ₂
1	L1–Sr(II)	2.948	1.7803	1.1677	1.6778
2	L1–Al(III)	2.817	1.799	1.018	1.5658
3	L1–Cr(II)	2.977	1.87	1.107	1.591
4	L2–Sr(II)	3.056	2.729	0.327	1.1198
5	L2–Al(III)	4.146	4.219	0.073	0.9826
6	L2–Cr(II)	4.207	3.169	1.038	1.3275
7	L3–Sr(II)	3.476	2.739	0.737	1.2690
8	L3–Al(III)	3.636	3.139	0.497	1.1583
9	L3–Cr(II)	3.336	2.219	1.117	1.5033

Table 3. Values of slope and intercept for proton–ligand titration and metal–ligand titration

S.N.	Details of data mentioned in tables	Intercept	Slope
1	Curve of pH vs. $\bar{\eta}A$ values for L1	0.471012	0.046012
2	Curve of pH vs. $\bar{\eta}$ values for L1 + Sr(II)	6.342667	–0.52133
3	Curve of pH vs. $\bar{\eta}$ values for L1 + Al(III)	5.338545	–0.32545
4	Curve of pH vs. $\bar{\eta}$ values for L1 + Cr(II)	1.508545	0.594545
5	Curve of pH vs. $\bar{\eta}A$ values for L2	0.157697	0.077697
6	Curve of pH vs. $\bar{\eta}$ values for L2 + Sr(II)	3.598364	0.036364
7	Curve of pH vs. $\bar{\eta}$ values for L2 + Al(III)	1.426364	0.636364
8	Curve of pH vs. $\bar{\eta}$ values for L2 + Cr(II)	4.34697	0.26897
9	Curve of pH vs. $\bar{\eta}A$ values for L3	0.278182	0.062182
10	Curve of pH vs. $\bar{\eta}$ values for L3 + Sr(II)	–16.3836	3.208364
11	Curve of pH vs. $\bar{\eta}$ values for L3 + Al(III)	–17.4685	3.995515
12	Curve of pH vs. $\bar{\eta}$ values for L3 + Cr(II)	2.653636	0.411636

for L2 means Cr(II) and Al(III) forms most stable complex with L2.

Notwithstanding the proton-ligand stability constant (pK) and metal-ligand stability constants ($\log K$) used to verify the validity of $\log K = a \times pK + b$ relation.

REFERENCES

1. A. B. Naik and M. L. Narwade, *Russ. J. Coord. Chem.* **35**, 932 (2009). doi 10.1134/S1070328409120136
2. O. A. El-Gammal, G. M. A. El-Reash, and M. M. El-Gamil, *Spectrochim. Acta, Part A* **123**, 59 (2014). <https://doi.org/10.1016/j.saa.2013.12.034>.
3. N. A. Anan, S. M. Hassan, E. M. Saad, I. S. Butler, and S. I. Mostafa, *Carbohydr. Res.* **346**, 775 (2011). <http://doi.org/10.1016/j.carres.2011.01.014>.
4. Y. Fukuda, R. Morishita, and K. Sone, *Bull. Chem. Soc. Jpn.* **49**, 1017 (1976). <https://doi.org/10.1246/bcsj.49.1017>.
5. W. J. O'Sullivan and G. W. Smithers, *Methods Enzymol.* **63**, 294 (1979). [https://doi.org/10.1016/0076-6879\(79\)63014-8](https://doi.org/10.1016/0076-6879(79)63014-8).
6. M. Szpak, A. Kamecka, B. Kurzak, and W. Goldeman, *Polyhedron* **123**, 385 (2017). <https://doi.org/10.1016/j.poly.2016.12.017>.
7. A. A. El-Bindary, G. G. Mohamed, A. Z. El-Sonbati, M. A. Diab, W. M. I. Hassan, S. M. Morgan, and A. K. Elkholy, *J. Mol. Liq.* **218**, 138 (2016). <https://doi.org/10.1016/j.molliq.2016.02.021>.
8. P. V. Tekade, S. D. Bajaj, and S. Thool, *Russ. J. Phys. Chem. A* **89**, 2346 (2015). doi 10.1134/S0036024415130282
9. S. Badhe, P. Tekade, S. Bajaj, and S. Thakare, *Russ. J. Phys. Chem. A* **89**, 2254 (2015). doi 10.1134/S0036024415120250

 PHYSICAL CHEMISTRY
 OF SOLUTIONS

Specific Molecular Interactions of Dihydropyridine Moiety in Polar and Non-Polar Solvents at Various Concentrations and Temperatures 303–318 K on Ultrasonic Data¹

Pradip V. Tekade^{a,*}, Bhagyashri U. Tale^{a,**}, Sonal D. Bajaj^{a,***}, and Nandini Authankar^a

^aDepartment of Chemistry, Jankidevi Bajaj College of Science, Jannalal Bajaj Marg, Civil Lines, Wardha, India

*e-mail: pradiptekade@gmail.com

**e-mail: bhagyashritale@gmail.com

***e-mail: sonu1star@gmail.com

Received October 25, 2017

Abstract—Ultrasonic studies of compounds of dihydropyridine series in polar and non-polar solvents at various concentrations and temperatures 303–318 K. Density and ultrasonic velocity and different thermoacoustical parameters measured. Rao's constant, molar volume, Wada's constant, isothermal compressibility reported with the help of these data using standard formulae. Ethanol and DMF selected as polar and non-polar solvents respectively. The variation in thermoacoustical parameters with temperature and concentration shows that the solute–solute molecular interaction takes place in solution which is more in DMF.

Keywords: dihydropyridine, adiabatic compressibility, intermolecular free length, acoustic impedance, surface tension, Rao's constant, molar volume, Wada's constant, isothermal compressibility

DOI: 10.1134/S0036024418120415

INTRODUCTION

Ultrasonic velocity measurements are used in understanding the molecular interactions in liquids. We already reported the ultrasonic studies on molecular interactions in *N*-phenyl-3-(pyridin-4-yl) prop-2-enamide as well as pyridoxine solutions in polar and non-polar solvents at different temperatures [1, 3]. Acoustical study on molecular interaction is also reported by Kukade et al. [2], Kharat [4] and Sasaki et al. [5]. Many researchers used IR spectroscopy to illustrate hydrogen bonding [6–9].

EXPERIMENTAL

Digital ultrasonic pulse echo velocity meter (Vi Microsystems Pvt. Ltd., India, Model no. VCT 70) used to measure the ultrasonic velocity of solutions. Here, ultrasonic studies of compounds of dihydropyridine series i.e. diethyl 1-(2-(1,3-dioxoisindolin-2-yl)butanoyl)-2,6-dimethyl-4-(3-nitrophenyl)-1,4-dihydropyridine-3,5-dicarboxylate (C-DHP-1), diethyl 1-(2-(1,3-dioxoisindolin-2-yl)-3-methylbutanoyl)-2,6-dimethyl-4-(3-nitrophenyl)-1,4-dihydropyridine-3,5-dicarboxylate (C-DHP-2) and diethyl 1-(2-(1,3-dioxoisindolin-2-yl)-3-methylbutanoyl)-2,6-dimethyl-4-(3-nitrophenyl)-1,4-dihydropyridine-

3,5-dicarboxylate (C-DHP-3) studied in ethanol and DMF at various concentrations and temperatures viz. 303, 308, 313, and 318 K. Structures of solutes are given in Fig. 1.

By measuring ultrasonic velocity and density, various acoustic parameters are calculated which are mentioned below. The variations of these properties with concentration and different temperature are represented by graphs.

From ultrasonic velocity and density data, various acoustic parameters are calculated using following formulae:

ultrasonic velocity

$$v, \text{ms}^{-1} = f\lambda,$$

where f is frequency of ultrasonic waves, λ is wave length;

adiabatic compressibility

$$\kappa, \text{kg}^{-1} \text{ms}^2 = 1/v^2\rho,$$

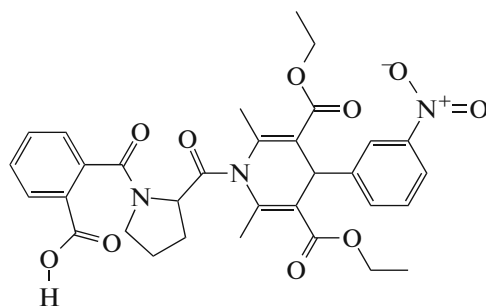
where v is ultrasonic velocity, ρ is density of the solution;

acoustic impedance

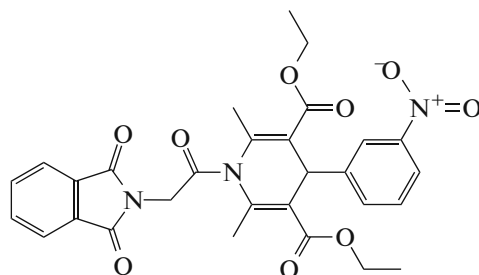
$$Z, \text{kg m}^{-2} \text{s}^{-1} = v\rho,$$

where v is ultrasonic velocity, ρ is density of the solution;

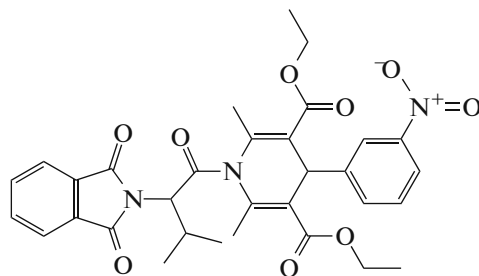
¹ The article is published in the original.



Diethyl 1-(2-(1,3-dioxisoindolin-2-yl)butanoyl)-2,6-dimethyl-4-(3-nitrophenyl)-1,4-dihydropyridine-3,5-dicarboxylate (C-DHP-1)



Diethyl 1-(2-(1,3-dioxisoindolin-2-yl)-3-methylbutanoyl)-2,6-dimethyl-4-(3-nitrophenyl)-1,4-dihydropyridine-3,5-dicarboxylate (C-DHP-2)



Diethyl 1-(2-(1,3-dioxisoindolin-2-yl)-3-methylbutanoyl)-2,6-dimethyl-4-(3-nitrophenyl)-1,4-dihydropyridine-3,5-dicarboxylate (C-DHP-3)

Fig. 1. Structure of solutes.

free length

$$L_f, m = K/\nu\rho^{1/2},$$

where ν is ultrasonic velocity, ρ is density, K (Jacobson temperature dependent constant) = $(93.875 + 0.345T) \times 10^{-8}$;

isothermal compressibility (β_T):

$$\beta_{T,n\text{-mix}} = \frac{17.1 \times 10^{-4}}{\nu_{n\text{-mix}}^2 T^{4/9} \rho_{n\text{-mix}}^{4/3}},$$

where ρ is density, ν is velocity;

Rao's constant

$$R = M/\rho\nu^{1/3},$$

where ρ is density, ν is molar volume, and M is molecular weight;

surface tension (γ)

$$\gamma = (S/6.3 \times 10^{-4} \rho)^{2/3};$$

molar volume (it is the ratio of density and molecular weight)

$$V_m = \frac{\rho}{M};$$

Wada's constant

$$W = (M\beta^{-1/7})/\rho,$$

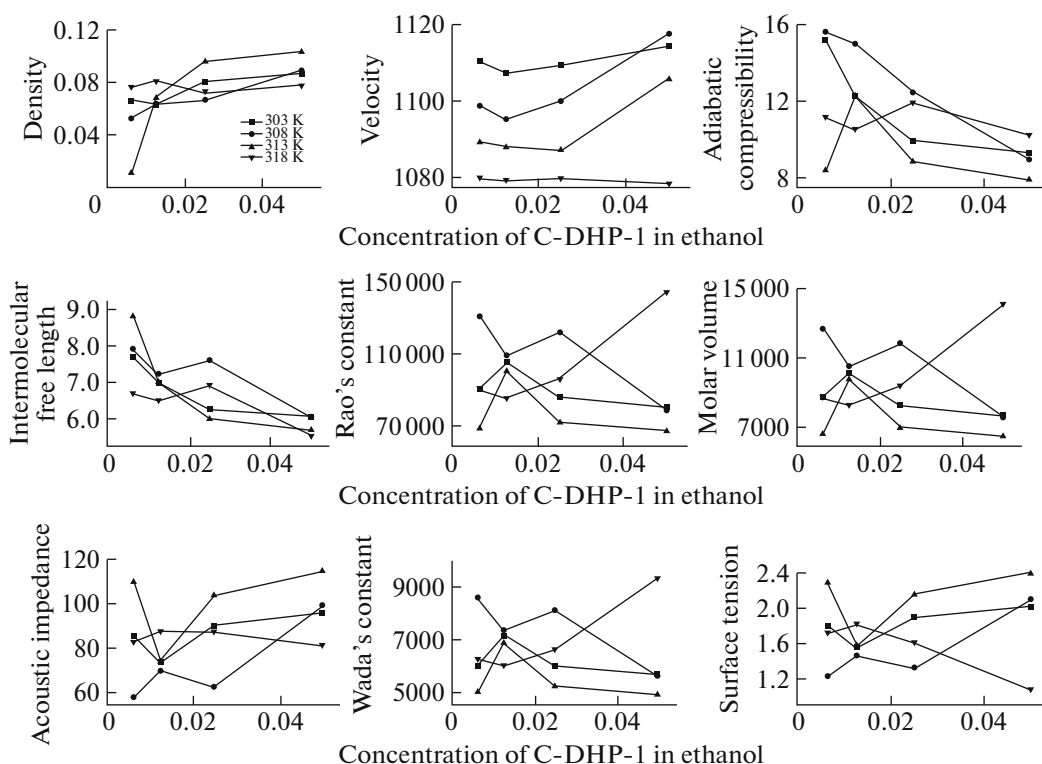


Fig. 2. Density, velocity, adiabatic compressibility, intermolecular free length, acoustic impedance, molar volume, Rao's constant, Wada's constant, surface tension at various temperature and concentration for (C-DHP-1 in ethanol).

where ρ is density, β is adiabatic compressibility, and M is molecular weight.

FTIR spectra were recorded on Bruker Alpha FTIR spectrometer at Department of Chemistry, Jankidevi Bajaj College of Science, Wardha.

RESULT AND DISCUSSION

Acoustical Study

The increase in velocity with concentrations, indicates the increase in cohesive forces due to solute-solvent interactions and it also suggests the intermolecular attractions, macromolecular motion in solution. Moreover, the increase in ultrasonic velocity also indicates the possibility of H-bond formation between solute and solvent. Density is measure of solvent-solvent and solute-solvent interaction. If value of density increases with increase in concentration, it indicates increase in solvent-solvent and solute-solvent interaction due to structure making ability of solute in presence of solvent. Adiabatic compressibility has the inverse relation with the ultrasonic velocity. The decrease in compressibility takes place due to a closer packing which leads to a decrease of intermolecular free length.

Free length or intermolecular free length (L_f) is the distance between the surfaces of the adjacent molecules. Intermolecular free length (L_f) changes due to

intermolecular attraction or repulsion. With increase in concentration, number of ions or particles increases in a given solution which leads to decrease in the gap (intermolecular free length) between two species. The intermolecular free length values decreases with the increasing values of ultrasonic velocity. It indicates significant interaction among solute and solvent molecules, due to which the structural arrangements in the adjacent constituent ions is considerably affected. The closer packing molecule suggests the dipole-dipole interaction between solute and solvent.

When an acoustic wave travels in any medium, pressure varies from particle to particle. The ratio of the instantaneous pressure excess at any particle in medium to the instantaneous velocity of that particle in medium is acoustic impedance of that medium. The increase in impedance values also suggests effective solute-solvent interactions. Positive values of molar volume suggests the effective interaction between the solute and solvent molecules because of increase in pressure and cohesive energy of the system due to strong interaction. Further, the increasing trends of apparent molar volume of systems with increase in molarity confirms the presence of strong solute-solvent as well as ion-solvent interactions

The molar sound velocity (Rao's constant) and molar compressibility (Wada's constant) increases with increase in temperature. This variation confirms

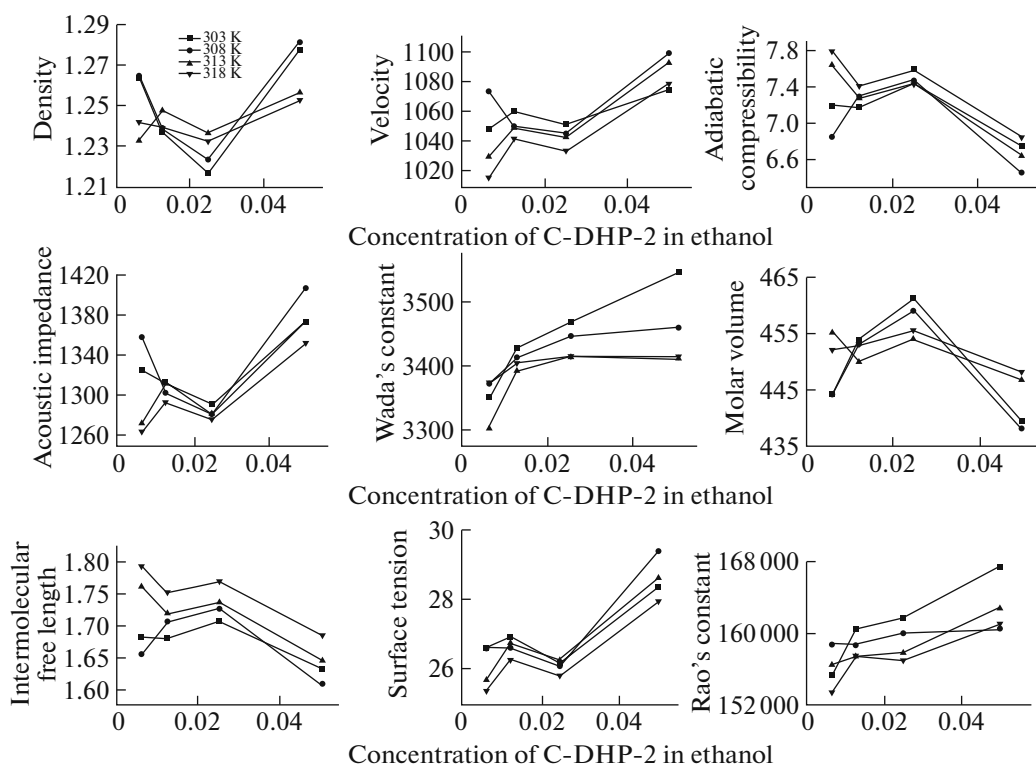


Fig. 3. Density, velocity, adiabatic compressibility, intermolecular free length, acoustic impedance, molar volume, Rao's constant, Wada's constant, surface tension at various temperature and concentration for (C-DHP-2 in ethanol).

the change in molecular interaction. The values of surface tension also increase with increase in concentration and temperatures. Surface tension is used to study the surface composition in aqueous solution. A variation of surface tension supports the attractive interactions between the solute and solvent.

In the present ultrasonic study of C-DHP-1, C-DHP-2, and C-DHP-3, observations are as follows.

1. For C-DHP-1 in ethanol: values of density, ultrasonic velocity, acoustic impedance and surface tension increases with increase in concentration and values of adiabatic compressibility as well as intermolecular free length decreases with increase in concentration which indicates strong solute–solvents interaction. Values of Rao's constant, molar volume and Wada's constant increases with increase in concentration for temperature 318 K which indicate more solute–solvent interaction than other temperatures (Fig. 2).

2. For C-DHP-2 in ethanol : values of density, ultrasonic velocity, acoustic impedance, surface tension, Rao's constant, molar volume (up to 0.025% concentration), Wada's constant increases with increase in concentration and values of adiabatic compressibility as well as intermolecular free length decreases with increase in concentration indicates strong solute–solvents interaction (Fig. 3).

3. For C-DHP-3 in ethanol : values of density, ultrasonic velocity, acoustic impedance, surface ten-

sion increases with increase in concentration & values of adiabatic compressibility as well as intermolecular free length decreases with increase in concentration indicates strong solute–solvents interaction. Upto 0.025% concentration, values of Rao's constant, molar volume, wada's constant increases with increase in concentration for 308 K temperature indicates strong more solute–solvents interaction at that temperature than other temperature where these parameters shows opposite trends (Fig. 4).

4. For C-DHP-1 in DMF : with increase in concentration, values of parameters such as density, ultrasonic velocity, acoustic impedance, surface tension, molar volume (except Rao's constant and Wada's constant) increases and values of adiabatic compressibility as well as intermolecular free length decreases which indicates strong solute–solvents interaction (Fig. 5).

5. For C-DHP-2 in DMF : with increasing concentration, increasing values of parameters such as density, ultrasonic velocity, acoustic impedance, surface tension, molar volume (at 303 K), Rao's constant (at 303 K) and wada's constant (at 303 K) indicates strong solute–solvent interaction. Decreasing values of adiabatic compressibility as well as intermolecular free length also indicates strong solute–solvents interaction (Fig. 6).

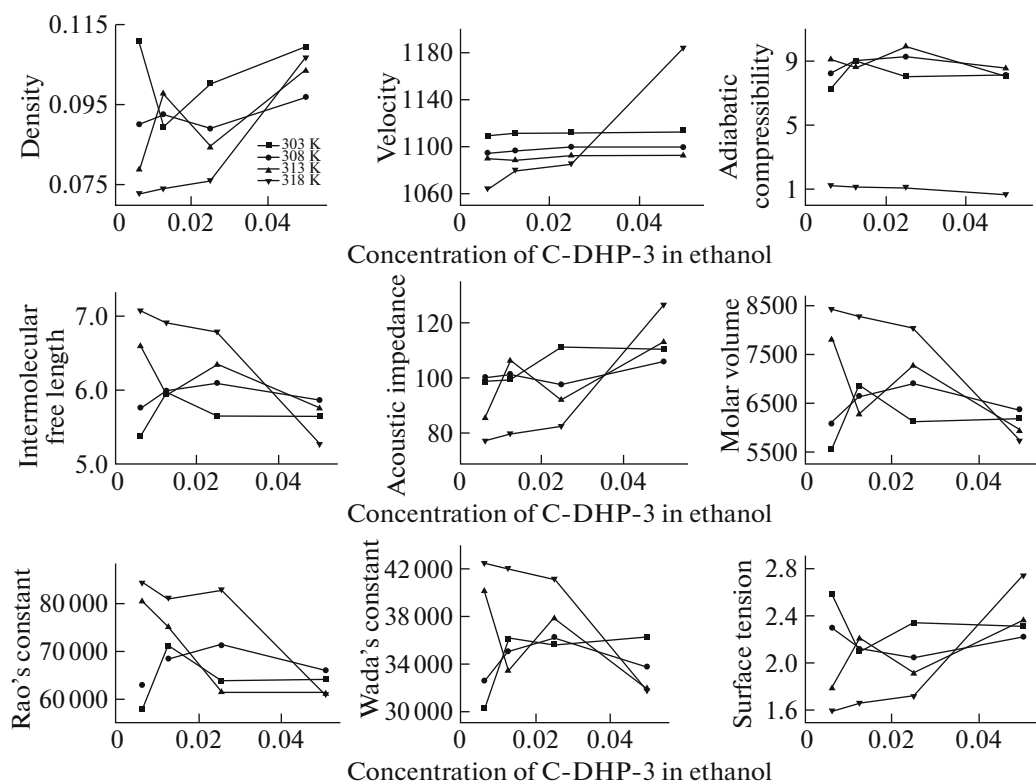


Fig. 4. Density, velocity, adiabatic compressibility, intermolecular free length, acoustic impedance, molar volume, Rao's constant, Wada's constant, surface tension at various temperature and concentration for (C-DHP-3 in ethanol).

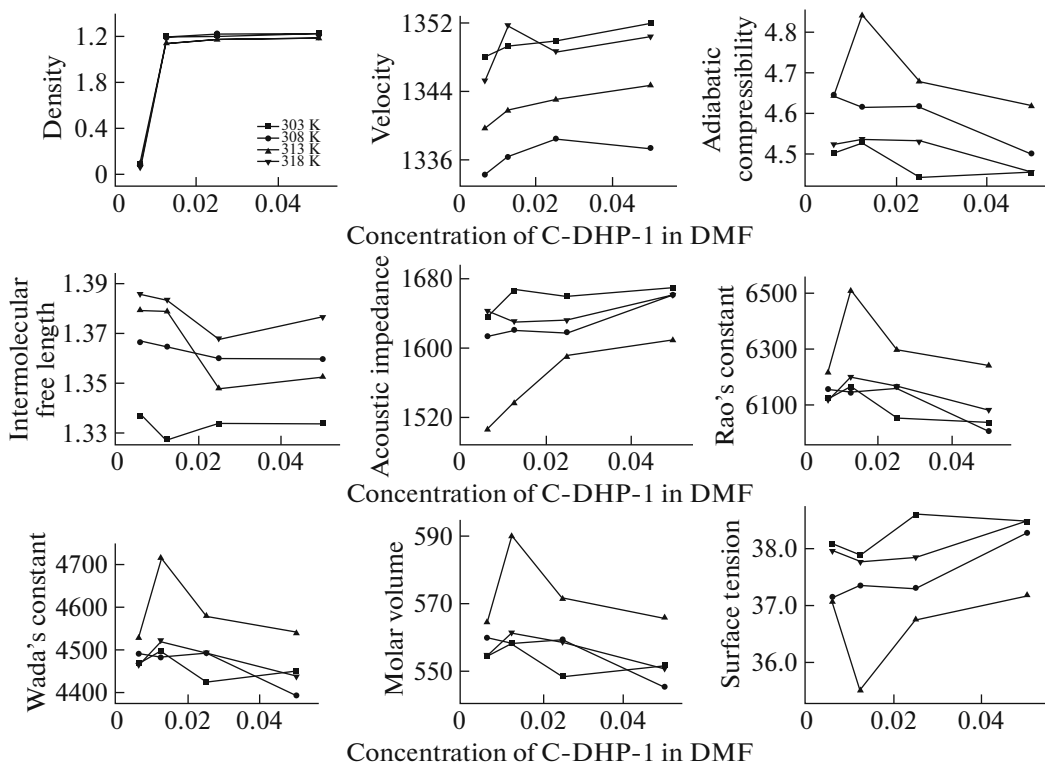


Fig. 5. Density, velocity, adiabatic compressibility, intermolecular free length, acoustic impedance, molar volume, Rao's constant, Wada's constant, surface tension at various temperature and concentration for (C-DHP-1 in DMF).

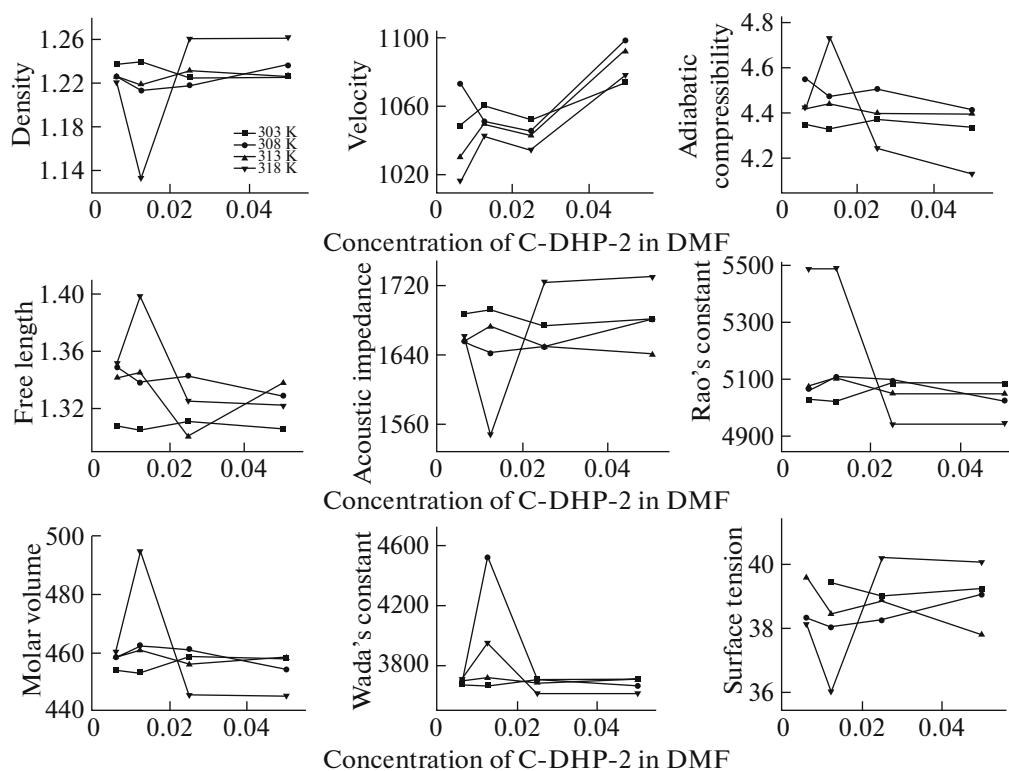


Fig. 6. Density, velocity, adiabatic compressibility, intermolecular free length, acoustic impedance, molar volume, Rao's constant, Wada's constant, surface tension at various temperature and concentration for (C-DHP-2 in DMF).

6. For C-DHP-3 in DMF : values of density, ultrasonic velocity, acoustic impedance (except 318 K), surface tension, Rao's constant (at 303 K), molar volume (at 303 K), Wada's constant (at 303 K) increases and values of adiabatic compressibility as well as intermolecular free length decreases with increase in concentration indicates strong solute–solvents interaction (Fig. 7).

FTIR Analysis

Results of ultrasonic velocity and density measurement are further supported by FTIR spectral analysis. The change in transmittance and shift in frequency of the representative peaks –OH and other functional groups present in the compounds in FTIR spectra gives interferences about the complex formation between solute and solvent by molecular interaction. Here All the three solutes i.e., C-DHP-1, C-DHP-2, and C-DHP-3 has carbonyl/hydroxyl/carboxylic acid functional group and solvent has hydroxyl/carbonyl functional group. So hydrogen bonding between solute and solvent is possible as shown in Figs. 8–11. In Figs. 8–11, frequency is expressed in terms of wave number. In IR spectra, when solute dissolved in solvent (ethanol/DMF) then value of its IR absorption frequency is found to be different from the IR absorption frequency of pure solute. Alteration in value of

frequency in presence of solvents supports hydrogen bonding between solute and solvent. The complex formation can be illustrated through the molecular structures of compounds and solvent.

Figure 8 clearly indicates frequency shifts from 3326.31 cm^{-1} (solute) to 3485.19 cm^{-1} (mixture of solute + solvent DMF). In Fig. 9 the FTIR spectrum of compound shows –OH stretching band at 3326.31 cm^{-1} and the FTIR spectrum of the solution of this compound in ethanol shows a broad band for –O–H stretching at 3348.95 cm^{-1} . Although, there are various hetero atoms present in the structure of the compound which are also available for the hydrogen bonding with the hydrogen atom of ethanol, but it is observed from the FTIR spectrum that there is a strong hydrogen bonding in –OH group of compound with oxygen atom of ethanol, which supports the presence of specific molecular interaction in solute and solvent.

In Fig. 10 the FTIR spectrum shows the enol form of the structure due to the presence of a band for –O–H stretching at 3342.12 cm^{-1} . When it is compared with the FTIR spectrum of solute in DMF solvent, it is observed that the frequency of –O–H band alters which is seen at 3463.87 cm^{-1} . Figure 11 clearly indicates that in mixture 1, the –O–H band appears at frequency 3347.33 cm^{-1} . When it is compared with the

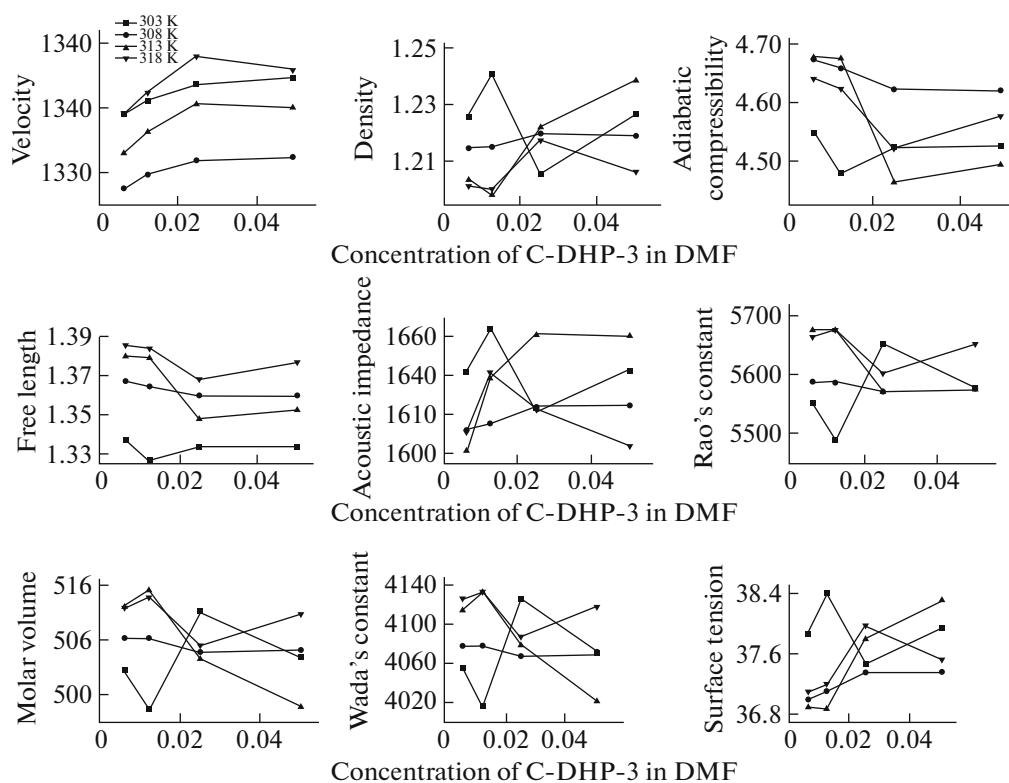


Fig. 7. Density, velocity, adiabatic compressibility, intermolecular free length, acoustic impedance, molar volume, Rao's constant, Wada's constant, surface tension at various temperature and concentration for (C-DHP-3 in DMF).

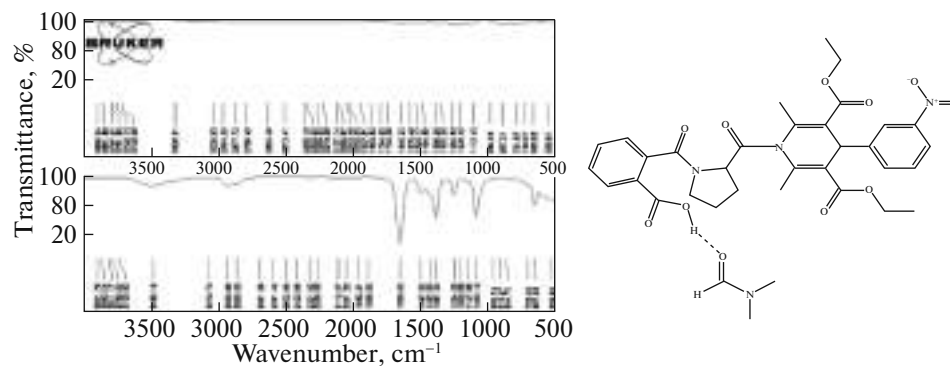


Fig. 8. FTIR spectrum of C-DHP-1 in DMF and hydrogen bonding of C-DHP-1 with DMF.

FTIR spectrum of the solute, it is observed that the frequency shifts from 3334.12 cm⁻¹ (solute-enol form) to 3347.33 cm⁻¹ (mixture of solute + ethanol solvent). Although, various oxygen and nitrogen atoms are there in the structure of the compound, which are also available for hydrogen bonding with the hydrogen atom in -O-H group of ethanol. It is seen from the FTIR spectrum of binary mixture that, the shift in the frequency of -OH group is more pronounced as that of other groups. Therefore, it can be concluded that the -OH group form a hydrogen bond.

CONCLUSION

From the present study it may be concluded that Interaction of solute with DMF is higher than that with ethanol, since values of acoustical parameters viz. density, ultrasonic velocity, acoustic impedance, surface tension are more in case of DMF except Rao's constant, Wada's constant as well as molar volume (for C-DHP-1 and C-DHP-3) and values of acoustical parameters viz. adiabatic compressibility and intermolecular free length are less for DMF. The com-

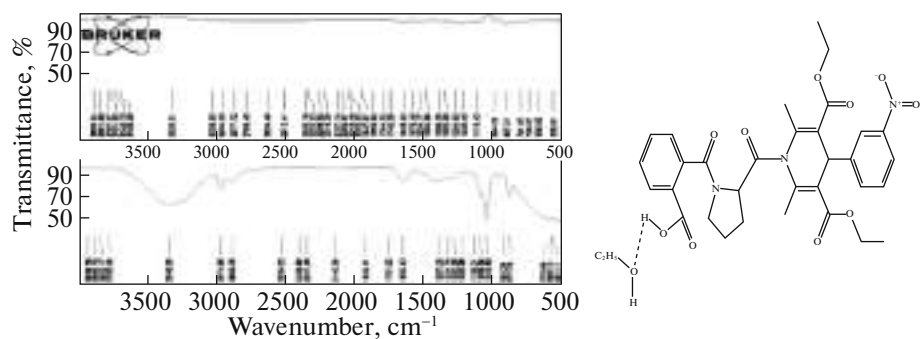


Fig. 9. FTIR spectrum of C-DHP-1 in ethanol and hydrogen bonding of C-DHP-1 with ethanol.

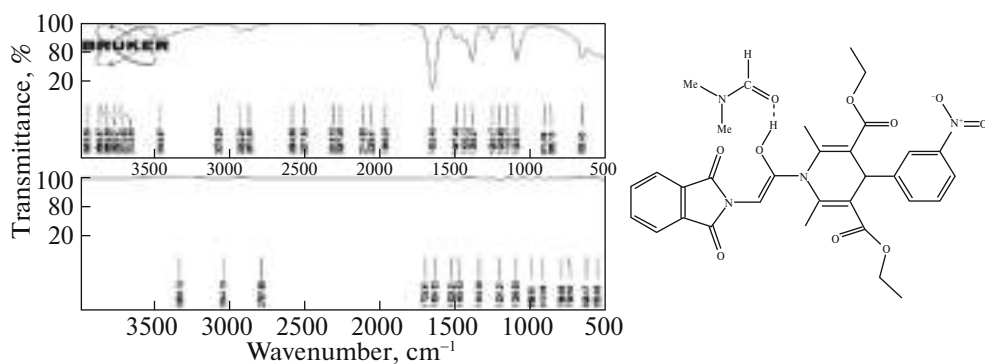


Fig. 10. FTIR spectrum of C-DHP-2 in DMF and hydrogen bonding of C-DHP-2 with DMF.

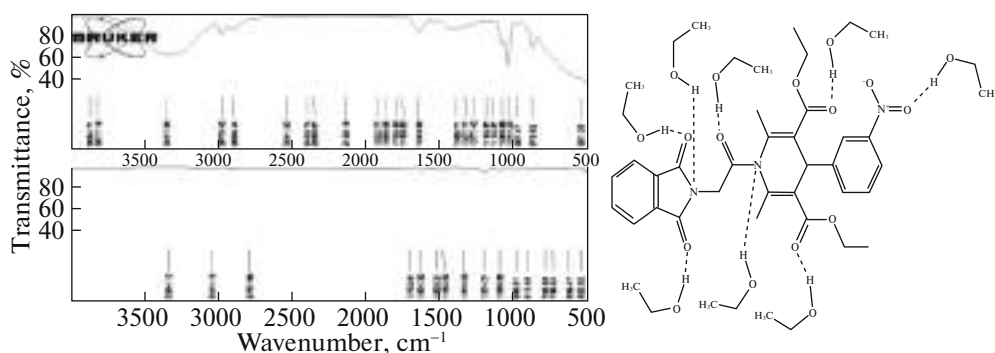


Fig. 11. FTIR spectrum of C-DHP-2 in ethanol and hydrogen bonding of C-DHP-2 with ethanol.

compressibility values are more for polar solvent, i.e., ethanol than non-polar solvent, i.e., DMF because solute in ethanol forms polar–polar molecule interaction, resulting in higher values of compressibility. But in DMF, the interaction is polar (solute)–non-polar (solvent), which leads to the decrease in compressibility. Similarly values of free length are more for ethanol because of less solute–solvent interaction. Thus the variation in thermoacoustical parameters with temperature and concentration shows that the solute–solvent molecular interaction also takes place in solution.

The resultant interaction in a solution is not only because of molecular structure of components of solution but also due to other factors like dispersion forces, dipole–dipole interaction, dipole–induced dipole interaction, hydrogen bonding, charge transfer interaction and complex formation etc. In graphical representation of various thermo-acoustical parameters, non-linear variation of these parameters over the whole composition and temperature in all cases indicates a strong solute–solvent interaction. On addition of solute to solvents, non-specific physical interac-

tions and unfavorable interactions takes place between unlike component molecules thereby giving the non-linear variation in various thermo-acoustical parameters at different temperature and concentration of binary solvent mixtures.

All values of acoustical parameters shows strong correlation with each other. The solute–solute molecular association takes place due to dipole–dipole interaction and the polar nature of various molecular species in the mixture. The solute–solvent association takes place due to slightly polar solute and polar/non-polar nature of the solvent. The association in this mixture is because of hydrogen bonding between solute and solvent. An analysis of these values supports strong intermolecular interaction which may be due to hydrogen bond, dipole–dipole, hyperconjugation and charge transfer. Thus, the concept of intermolecular interaction explained by variation of acoustical parameter.

The results of ultrasonic velocity measurements were further examined using FTIR spectra for C-DHP-1 and C-DHP-2 in polar and non-polar solvents. FTIR study shows alteration in the frequency values for O–H stretching of the compound in binary solution which indicates the molecular interaction between solute–solvent (compound with ethanol and DMF) and solvent–solvent (ethanol and DMF).

Thus, the interaction of solute with ethanol is more than DMF.

REFERENCES

1. P. Tekade, S. Lohakare, S. Bajaj, and R. Naik, *Russ. J. Phys. Chem. A* **89**, 2105 (2015). doi 10.1134/S0036024415110187
2. S. D. Kukade, S. K. Singh, R. R. Naik, and S. V. Bawankar, *J. Mol. Liq.* **222**, 225 (2016). <https://doi.org/doi.10.1016/j.molliq.2016.07.059>.
3. R. R. Naik, S. V. Bawankar, P. V. Tekade, and O. A. Mahodaya, *Russ. J. Phys. Chem. A* **89**, 152 (2015). doi 10.1134/S0036024415010227
4. S. J. Kharat, *J. Mol. Liq.* **140**, 10 (2008). <https://doi.org/doi.10.1016/j.molliq.2007.12.006>.
5. K. Sasaki and K. Arakawa, *Bull. Chem. Soc. Jpn.* **46**, 2738 (1973). <https://doi.org/doi.10.1246/bcsj.46.2738>
6. S. Schlucker, J. Koster, R. K. Singh, and B. P. Asthana, *J. Phys. Chem. A* **111**, 5185 (2007). doi 10.1021/jp0702292
7. F. Schwager, E. Marand, and R. M. Davis, *J. Phys. Chem.* **100**, 19268 (1996). doi 10.1021/jp9613448
8. S. Kubo and J. F. Kadla, *Biomacromolecules* **6**, 2815 (2005). doi 10.1021/bm050288q
9. J. Zhang, F. Han, X. Wei, L. Shui, H. Gong, and P. Zhang, *Ind. Eng. Chem. Res.* **49**, 2025 (2010). doi 10.1021/ie9014759

PHYSICAL CHEMISTRY
OF SOLUTIONS

Stability Constants of Complexes of Cr(II) and Sr(II)
with Quinazoline and Dihydropyridine in Dioxane–Water Mixture
on Spectrophotometric Data¹

Pradip V. Tekade^{a,*}, Sonal D. Bajaj^{a,**}, Bhagyashri U. Tale^a, Nandini Authankar^a, and Sonali Sadmake^a

^aDepartment of Chemistry, Jankidevi Bajaj College of Science, Jannalal Bajaj Marg, Civi Lines, Wardha, India

* e-mail: pradiptekade@gmail.com

** e-mail: sonulstar@gmail.com

Received August 21, 2017

Abstract—The interaction of Cr(II) and Sr(II) with a series of four novel *N*-heterocycles viz. 2-(1,3-dioxoindoline-2-yl)-*N*-(4-oxo-2-phenylquinazolin-3(4H)-yl), 1-(2-((4-oxo-2-phenylquinazolin-3(4H)-yl) carbomoyl), diethyl 1-(2-(1,3-dioxoisoindolin-2-yl)-3-methylbutanoyl)-2,6-dimethyl-4-(3-nitrophenyl)-1,4-dihydropyridine-3,5-dicarboxylate, diethyl 1-(2-(1,3-dioxoisoindolin-2-yl)butanoyl)-2,6-dimethyl-4-(3-nitrophenyl)-1,4-dihydropyridine-3,5-dicarboxylate studied by spectrophotometric technique at 0.01 M ionic strength and 28°C in 70% dioxane–water mixture. The data obtained used to estimate the stability constant of the complexes. Investigation of Cr(II) and Sr(II) complexes with these ligands shows 1 : 1 complex formation. The values of conditional stability constants of Sr(II) complexes are greater than the corresponding Cr(II) complexes. The results obtained of stability constants are in good agreement with the structure of ligand and reactivity pattern of metal ion. These can be of interest for specialists in the field of coordination chemistry.

Keywords: stability constant, chromium complexes, strontium complexes, *N*-heterocyclic ligands, Job's variation method, quinazoline, dihydropyridine

DOI: 10.1134/S0036024418110419

INTRODUCTION

The scientific community is striving to understand the role of heterocycles and fused heterocycles in drug discovery programme due to its impact on multi-drug resistance (MDR) of anticancer drugs. The quinazolines belong to a family of heterocyclic nitrogen compounds that have attracted increasing interest because of their broad spectrum of biological activity [1], including antifungal, anti-tumor, anti-malaria, anti-convulsant, anti-microbial, anti-inflammatory, anti-tumor and antihyperlipidemic activities [2]. Moreover, Pyridine derivatives are very important chemicals with tremendous biological application. The pyridine derivatives have different biological target by interacting with enzymes, proteins and DNA [3]. The stability constants for the metal complex widely used in many fields such as biological processes, analytical processes, pharmaceuticals, etc. Moreover, metal complex play a very important role in nature.

The basic principle of the spectrophotometric technique is the measurement of interaction between energy and electrons of the substance. The spectrophotometric technique is analytical method used for estimating con-

centration of metal ion in liquid solution. One of the most spectacular effects of complex formation is the change of spectral properties. Consequently, spectrophotometry emerged as suitable technique for determination of stability constant of metal complexes with biologically active compounds. Study of stability constant of different complexes reported by many researchers [4–7] in different solvents by spectrophotometric technique. Maurya et al. [8] and Hassan [9] reported the complex formation in benzimidazole derivatives by spectrophotometric study.

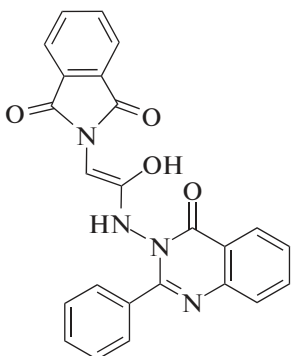
Therefore, we thought to study the chelating properties of some novel *N*-heterocycles viz. dihydropyridine and quinazoline derivatives (ligands 1 to 4) with Cr(II) and Sr(II) metal ions by Job's variation method under suitable conditions spectrophotometrically.

EXPERIMENTAL

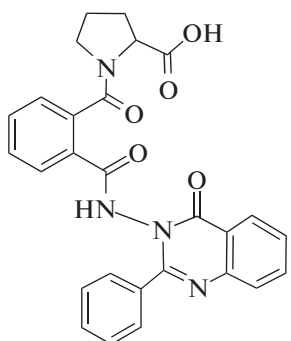
All the chemicals used are of laboratory grade and used without further purification. The ligands prepared by known methods [10, 11]. Compounds recryst-

¹ The article is published in the original.

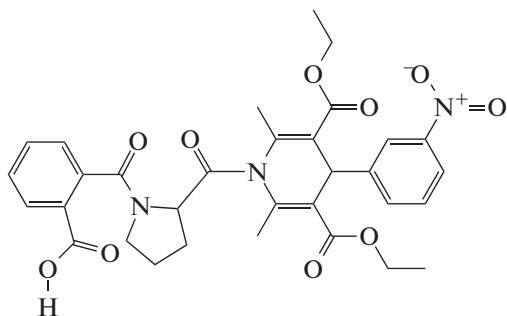
tallized before use. The structures of ligands 1 to 4 are given below:



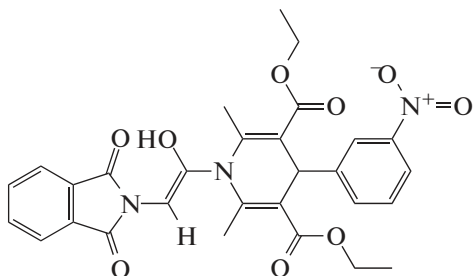
Ligand 1: 2-(1,3-dioxoisindolin-2-yl)-*N*-(4-oxo-2-phenylquinazolin-3(4H)-yl)acetamide;



Ligand 2: 1-(2-((4-oxo-2-phenylquinazolin-3(4H)-yl)carbamoyl)benzoyl)pyrrolidine-2-carboxylic acid;



Ligand 3: diethyl 1-(2-(1,3-dioxoisindolin-2-yl)-3-methylbutanoyl)-2,6-dimethyl-4-(3-nitrophenyl)-1,4-dihydropyridine-3,5-dicarboxylate;



Ligand 4: diethyl 1-(2-(1,3-dioxoisindolin-2-yl)butanoyl)-2,6-dimethyl-4-(3-nitrophenyl)-1,4-dihydropyridine-3,5-dicarboxylate.

The distilled water used free from carbon dioxide and pH of this water about 6.80. Cr(II) (0.01 M) and Sr(II) (0.01 M) ionic solutions prepared from Chromium chloride and Strontium chloride (AR grade) and standardized by standard methods. 0.01 M KNO_3 used for maintaining ionic strength constants. The ligands are insoluble in water, hence ligand solutions of 0.01 M prepared in 70% dioxane–water (vol/vol) mixture. Contech digital balance (CA 224) having accuracy 0.001 g used for weighing of samples. Bio-Era Elite UV–Vis spectrophotometer with accuracy ± 0.01 units used for absorbance measurements.

Metal–ligand stability constants and confirmation of complex formation studied by and Gürkan [12]. Solutions of metal salt and ligand of equimolar concentration (1.00×10^{-2} M) mixed pairwise in different ratios to prepare Job's solutions. Final volume of each solution made 10 mL after adjusting the appropriate pH and maintaining the constant ionic strength. In addition to the wavelength of maximum (λ_{max}) some other wavelength selected as proposed by Gould and Vosburgh [13].

RESULTS AND DISCUSSION

The concentration of complex (x) in any metal ligand solution is obtained by Job's curve. Initial concentrations of metal and ligand in a particular solution considered a and b and the equilibrium constant determined by the law of mass action.

$$K = \frac{x}{(a-x)(b-x)}$$

or

$$K = \frac{x}{(a_1-x)(b_1-x)(a_2-x)(b_2-x)}$$

The composition of metal ion solution (1×10^{-2} M) and ligand (1×10^{-2} M) prepared in ten series. Value λ_{max} determined using one of the compositions at conditional stability constants of complexes in which there is maximum absorption. The absorptions for all the compositions recorded at constant wavelength (λ_{max}). Each solution is diluted up to 15 mL and absorptions recorded at same λ_{max} . The data of absorption and percentage composition of metal ion and ligand solutions at constant pH used and the curves constructed. The conditional stability constants obtained by spectrophotometric techniques presented in the Table 1.

It is seen from the above table that, the highest stability constant value obtained for Cr(II)–Ligand 1. This is due to the formation of coordinated bond between –OH group of Ligand 1 (enol form) with the Cr(II) metal ion. Moreover, Ligand 1 contains both –NH and –OH group which are susceptible for the

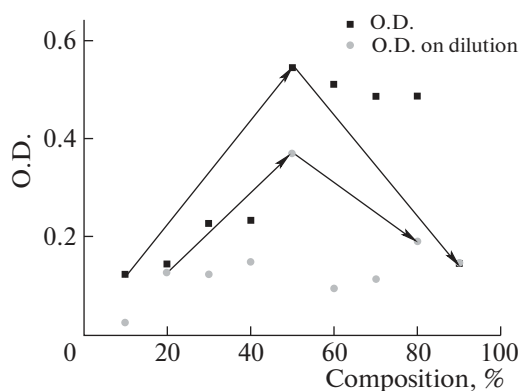


Fig. 1. The variation of O.D. with % composition for system Cr(II)–Ligand 1.

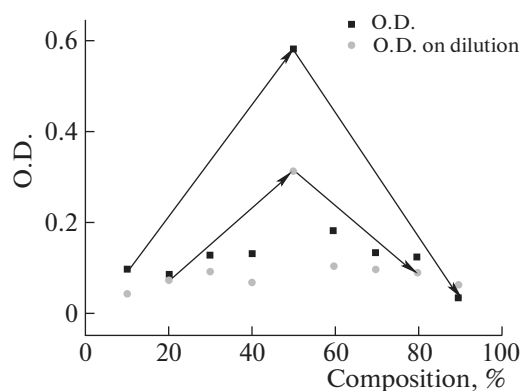


Fig. 2. The variation of O.D. with % composition for system Cr(II)–Ligand 2.

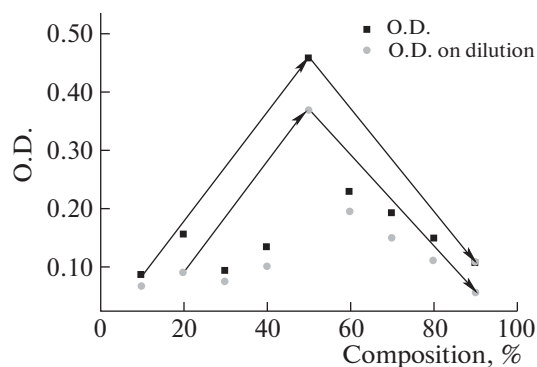


Fig. 3. The variation of O.D. with % composition for system Sr(II)–Ligand 2.

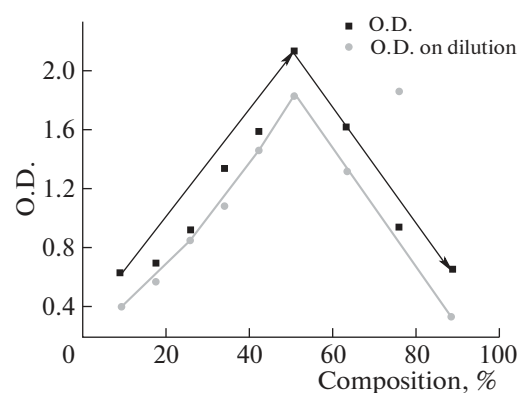


Fig. 4. The variation of O.D. with % composition for system Cr(II)–Ligand 3.

formation of coordinate bond with Cr(II) ion, this is the reason behind its higher stability constant. On the other hand, ligand 2 and 3 both have free $-\text{COOH}$ group which is easily available for formation of coordinate bond with metals. Furthermore, they shows greater stability constant value for Sr(II) complexes

than Cr(II). This may be attributed to the high reactivity of the strontium being alkaline earth metal. Furthermore, for ligand 4, the highest value of stability constant observed for Cr(II) complexes, this is attributed the presence of $-\text{OH}$ group in the structure and small ionic radius of Cr(II) ion than Sr(II) ion.

The curves constructed between the values of optical density and percentage composition of metal ion. The variation of O.D. with % composition for different systems given in Figs. 1–7.

Table 1. Conditional stability constants of complexes

System	$K \times 10^3$	$\log K$
Cr(II)–Ligand 1	0.933	2.829
Cr(II)–Ligand 2	0.3845	2.584
Sr(II)–Ligand 2	0.6338	2.801
Cr(II)–Ligand 3	0.745	2.872
Sr(II)–Ligand 3	0.838	2.923
Cr(II)–Ligand 4	1.04	3.107
Sr(II)–Ligand 4	0.199	2.298

ORDER OF STABILITY CONSTANTS

Cr(II)–Ligand 4 > Cr(II)–Ligand 1 > Sr(II)–Ligand 3 > Cr(II)–Ligand 3 > Sr(II)–Ligand 2 > Cr(II)–Ligand 2 > Sr(II)–Ligand 4.

CONCLUSIONS

In the present study, we have reported spectrophotometric investigation of stability constant of complexes of the novel Quinazoline and Dihydropyridine derivatives with Cr(II) and Sr(II) metal ions. The for-

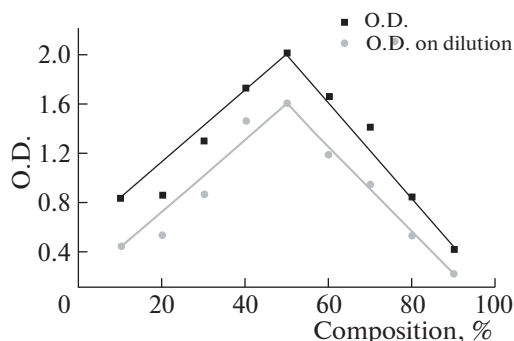


Fig. 5. The variation of O.D. with % composition for systems Sr(II)–Ligand 3.

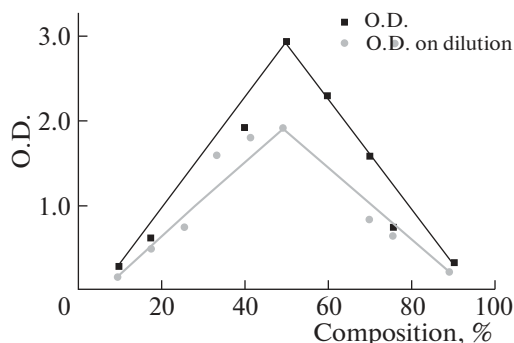


Fig. 6. The variation of O.D. with % composition for systems Cr(II)–Ligand 4.

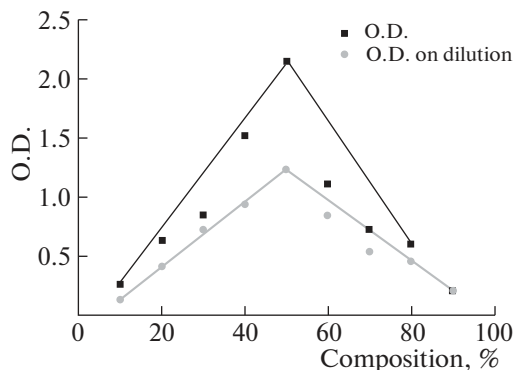


Fig. 7. The variation of O.D. with % composition for systems Sr(II)–Ligand 4.

mation of complexes (1 : 1) studied by Job's variation method. The spectrophotometric study shows the existence of intermolecular interaction between the solute and metal ion solution and the measured condi-

tional stability constant concluded that the complex formation tendency of ligands different with different metal ions. Stability constant of complexes depends upon the structure of ligand and ionic radius of the metal ion. The values of conditional stability constants of Sr(II) complexes are greater than the corresponding Cr(II) complexes. The obtained stability constants are in good agreement with the structure of ligand and reactivity pattern of metal ion.

REFERENCES

1. D. He, M. Wang, S. Zhao, Y. Shu, H. Zeng, C. Xiao, and Y. Liu, *Fitoterapia* (2017). doi 10.1016/j.fitote.2017.05.001
2. D. Kumar and S. Kumar Jain, *Curr. Med. Chem.* **23**, 4338 (2016).
3. A. A. Altaf, A. Shahzad, Z. Gul, N. Rasool, A. Badshah, B. Lal, and E. Khan, *J. Drug. Des. Med. Chem.* **1**, 1 (2015). doi 10.11648/j.jddmc.20150101.11
4. R. Ravichandran, M. Rajendran, and D. Devapiriam, *Food Chem.* **146**, 472 (2014). doi 10.1016/j.foodchem.2013.09.080
5. N. Singh and A. Ahmad, *J. Mol. Struct.* **1074**, 408 (2014). doi 10.1016/j.molstruc.2014.05.076
6. J.-i. Itoh, T. Yotsuyanagi, and K. Aomura, *Anal. Chim. Acta* **76**, 471 (1975). doi 10.1016/S0003-2670(01)85423-4
7. S. A. Tirmizi, F. H. Wattoo, M. H. S. Wattoo, S. Sarwar, A. N. Memon, and A. B. Ghangro, *Arab. J. Chem.* **5**, 309 (2012). doi 10.1016/j.arabjc.2010.09.009
8. M. R. Maurya and N. Bharti, *Trans. Met. Chem.* **24**, 389 (1999). doi 10.1023/A:1006942231677
9. A. Hassan, *Phosphor., Sulfur, Silicon Relat. Elem.* **106**, 55 (1995). doi 10.1080/10426509508027889
10. S. D. Bajaj, O. A. Mahodaya, P. V. Tekade, V. B. Patil, and S. D. Kukade, *Russ. J. Gen. Chem.* **87**, 546 (2017). doi 10.1134/S1070363217030264
11. K. P. Rakesh, H. M. Manukumar, and D. Channe Gowda, *Bioorg., Med. Chem. Lett.* **25**, 1072 (2015). doi 10.1016/j.bmcl.2015.01.010
12. R. Gürkan, N. Altunay, and N. Gürkan, *J. Iran. Chem. Soc.* **1**, 17 (2017). doi 10.1007/s13738-017-1053-9
13. K. R. Gould and C. W. Vosburgh, *J. Am. Chem. Soc.* **64**, 1630 (1942). doi 10.1021/ja01259a044

 PHYSICAL CHEMISTRY
 OF SOLUTIONS

Ultrasonic Studies on Molecular Interactions of *N*-Phthaloylglycine in Protic and Aprotic Solvents at 303–318 K¹

Pradip Tekade^{a,*}, Bhagyashri Tale^{a,**}, and Sonal Bajaj^{a,***}

^aDepartment of Chemistry, Jankidevi Bajaj College of Science, Jamnalal Bajaj Marg, Civil Lines, Wardha, India

*e-mail: pradiptekade@gmail.com

**e-mail: bhagyashritale@gmail.com

***e-mail: sonu1star@gmail.com

Received September 4, 2017

Abstract—Ultrasonic studies of (1,3-dioxo-1,3-dihydro-2*H*-isoindol-2-yl)acetic acid (*N*-phthaloylglycine) in polar and non polar solvent of various concentrations and temperatures 303–318 K are carried out. Ethyl alcohol and DMSO selected as polar and non-polar solvents respectively. Density and ultrasonic velocity measured. Different thermo-acoustical parameters viz. adiabatic compressibility, intermolecular free length, acoustic impedance, surface tension, Rao's constant, molar volume, wada's constant calculated with the help of these data using standard formulae. These data are used in understanding the molecular interactions in mixtures.

Keywords: adiabatic compressibility, intermolecular free length, acoustic impedance, surface tension, Rao's constant, molar volume, Wada's constant

DOI: 10.1134/S0036024418130228

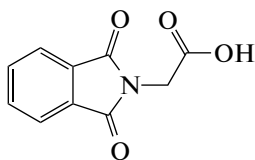
INTRODUCTION

Ultrasonic velocity measurements are used in understanding the molecular interactions in liquids. As a part of ongoing endeavor, we have reported the ultrasonic studies on molecular interactions [1, 3]. Similarly, Kukade et al. [2], Kharat [4], Pal et al. [5], Tamura et al. [6], Iqbal [7], Bonsen [8], and Borthakur et al. [9] reported molecular interaction using acoustical study.

Literature survey reveals that the *N*-phthaloyl compounds have a wide range of applications. Very few references proposed the study of various ultrasonic properties of *N*-phthaloyl derivaives. So, it is the topic of interest to study the thermo acoustical properties of titled compounds by ultrasonic interferometer.

EXPERIMENTAL

Structure of (1,3-dioxo-1,3-dihydro-2*H*-isoindol-2-yl)acetic acid (*N*-phthaloylglycine/NPT-GL):



Digital ultrasonic pulse echo velocity meter (Vi Microsystems Pvt. Ltd., Chennai-96, model no. VCT 70) used to measure the ultrasonic velocity.

From ultrasonic velocity and density data, various acoustic parameters are calculated using following formulae:

ultrasonic velocity

$$v, \text{ms}^{-1} = f\lambda,$$

where f is frequency of ultrasonic waves, λ is wave length;

adiabatic compressibility

$$\kappa, \text{kg}^{-1} \text{ms}^2 = 1/v^2\rho,$$

where v is ultrasonic velocity, ρ is density of the solution;

acoustic impedance

$$Z, \text{kg m}^{-2} \text{s}^{-1} = v\rho,$$

where v is ultrasonic velocity, ρ is density of the solution;

free length

$$L_r, \text{m} = K/v\rho^{1/2},$$

where v is ultrasonic velocity, ρ is density, K (Jacobson temperature dependent constant) = $(93.875 + 0.345T) \times 10^{-8}$;

¹ The article is published in the original.

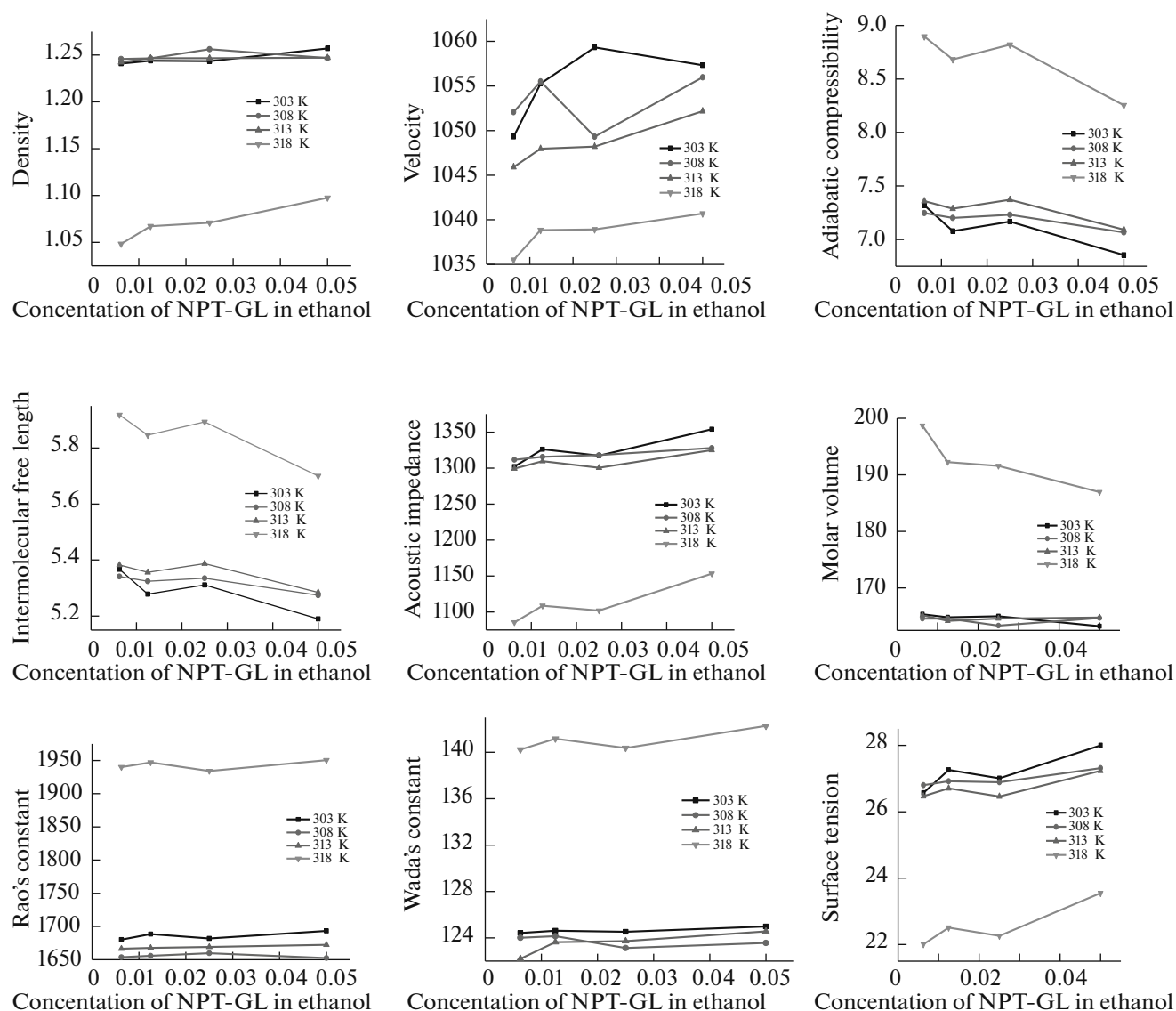


Fig. 1. Variation of density, velocity, adiabatic compressibility, intermolecular free length, acoustic impedance, molar volume, Rao's constant, Wada's constant, surface tension at various temperature and concentration for NPT-GL in ethanol.

Rao's constant

$$R = M/\rho v^{1/3},$$

where ρ is density, v is molar volume and M is molecular weight;

surface tension (S)

$$v = (S/6.3 \times 10^{-4} \rho)^{2/3};$$

molar volume (it is the ratio of density and molecular weight)

$$V_m = \frac{\rho}{M};$$

Wada's constant

$$W = (M\beta^{-1/7})/\rho,$$

where ρ is density, β is adiabatic compressibility, and M is molecular weight.

FTIR spectrum recorded on Bruker Alpha FTIR spectrometer (Germany) at Department of Chemistry, Jankidevi Bajaj College of Science, Wardha.

RESULTS AND DISCUSSION

The ultrasonic velocity of solution of NPT-GL increases with increase in concentration and decreases with increase in temperature in both solvents (Figs. 1 and 2). This denotes strong interaction at lower concentrations. The increasing value of velocity with increase in concentration also indicates solute-solvent interaction and it is more in ethanol. Moreover,

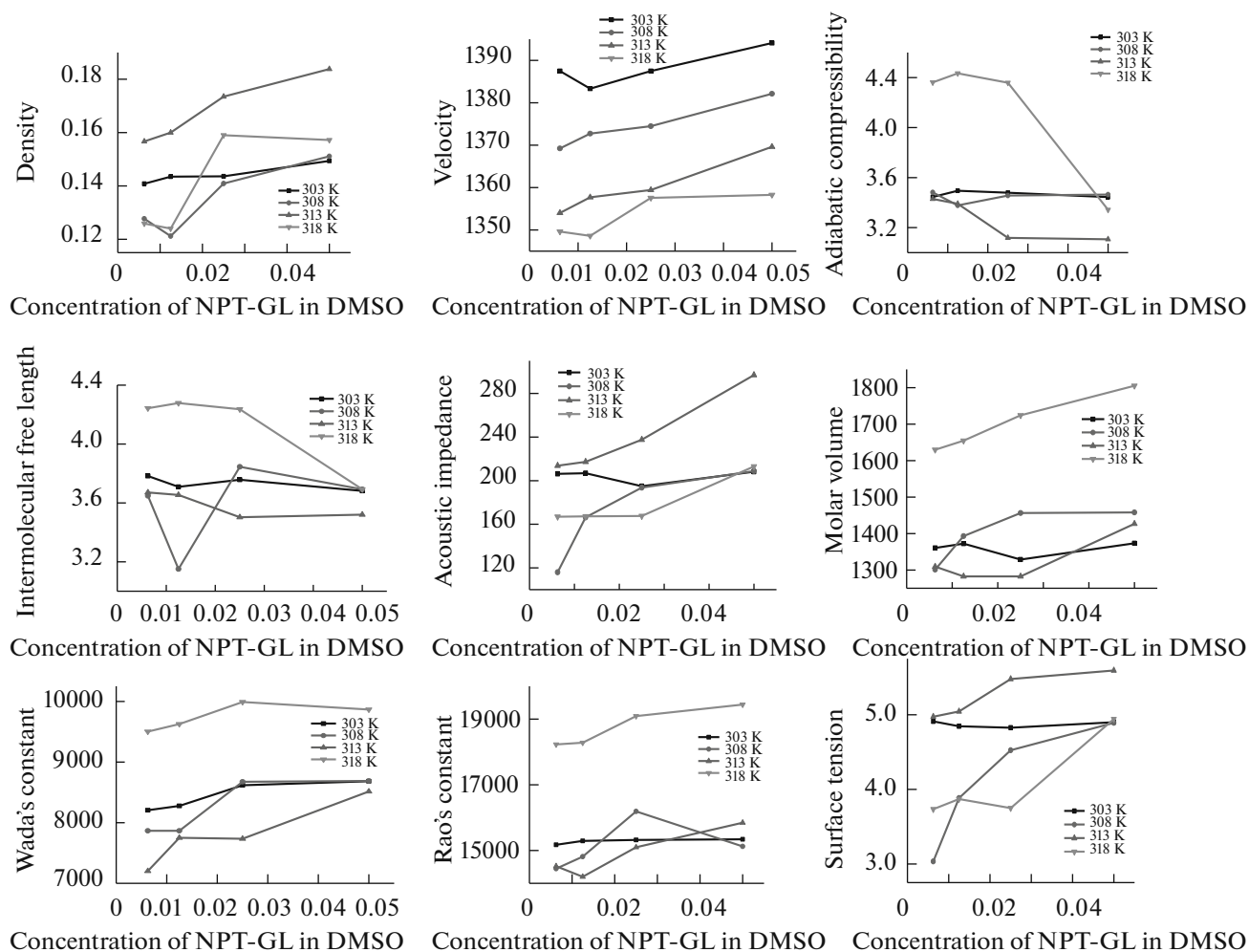


Fig. 2. Variation of density, velocity, adiabatic compressibility, intermolecular free length, acoustic impedance, molar volume, Rao's constant, Wada's constant, surface tension at various temperature and concentration for NPT-GL in DMSO.

the increase in ultrasonic velocity indicates the possibility of H-bond formation among solute and solvent. It also indicates greater association between solute and solvent.

The increasing value of density of NPT-GL solution with concentration indicates strong attraction between solute and solvent molecules. The decrease in values of density with increase in temperature indicates decrease in intermolecular forces.

The adiabatic compressibility of NPT-GL solution shows exactly the reverse trend of velocity. The adiabatic compressibility decreases with increase in concentration indicates strong solute solvent interaction as well as associating tendency of solute and solvent molecules. The decrease in adiabatic compressibility is due to the fact that solute molecules ionized in dilute solutions. These ions get surrounded in solution by a layer of solvent molecules, firmly bounded and oriented towards the ions. The orientation of solvent molecules around the ions is because of influence of

the electrostatic field of ions, which lowers the compressibility of the solution, i.e., the solutions become difficult to compress. Adiabatic compressibility (β) decreases because (i) an increase in the number of incompressible species, (ii) structural changes in solution. This happens due to the association taking place between the molecules.

Free length is the average distance between the surfaces of two adjacent molecules, also known as intermolecular free length. The decrease in intermolecular free length with increasing concentration indicates increase in intermolecular forces with the addition of solute. The decrease in free length with increase in concentration is indication of significant interaction between solute and solvent molecules. Intermolecular free length decreases with increasing concentration indicates enhanced molecular association. As concentration increases, number of ions or particles increase in a given volume which leads to

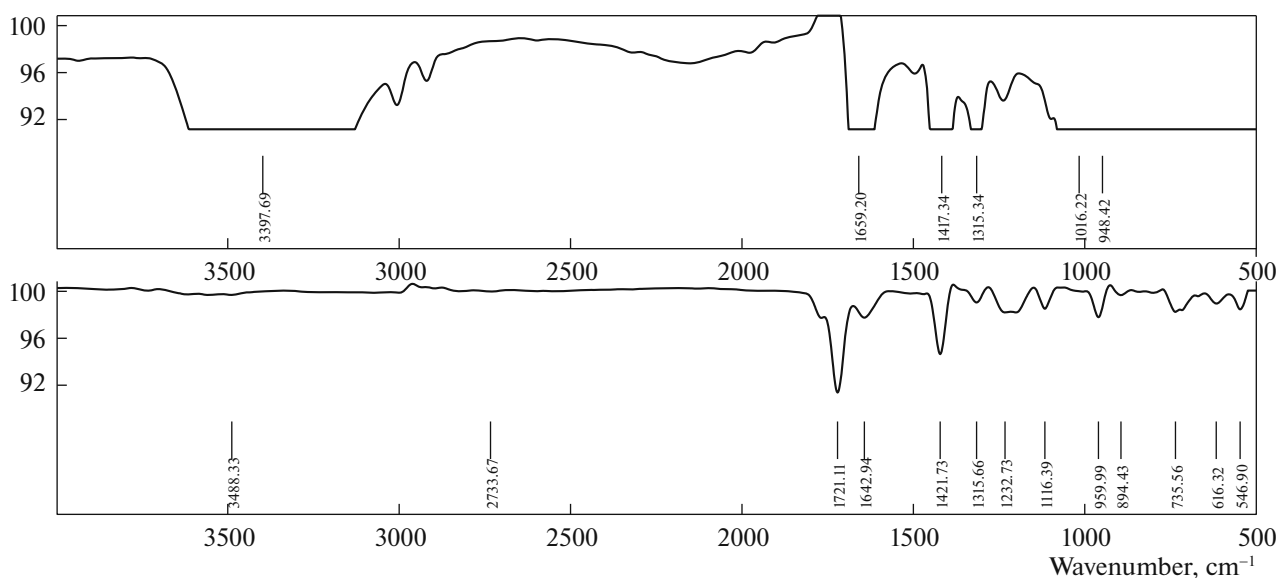


Fig. 3. Stacked structure of FT-IR spectrum of NPT-GL and solution of NPT-GL in DMSO.

decrease in the gap (intermolecular free length) between two species.

When an acoustic wave travels in a medium, pressure from particle to particle varies. The ratio of the instantaneous pressure excess at any particle of the medium and the instantaneous velocity of that particle is an acoustic impedance of the medium. The increase in impedance values in polar as well as non polar solvent also indicates effective solute-solvent interactions. Acoustic impedance values also increases with increasing concentration.

Positive values of molal volume in both solvents indicate the interaction between the solute and solvent molecules due to increase in pressure and cohesive energy of the system because of strong interaction. The apparent molal volume is positive at all concentrations and temperature which supports strong ion-ion interaction occurring in solution.

The molar sound velocity (Rao's constant) and molar compressibility (Wada's constant) increased

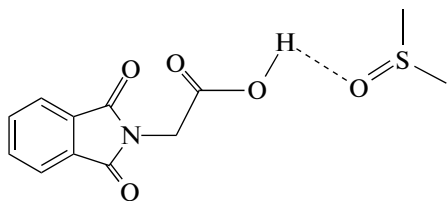


Fig. 4. Formation of hydrogen bonding between solute and dimethyl sulfoxide.

with temperature in both solvents. This variation confirms the change in molecular interactions.

The values of surface tension also increases with increase in concentration and temperatures in both the solvents.

Interaction of solute with DMSO is higher than that with ethanol, since values of acoustical parameters are more in case of DMSO except density, adiabatic compressibility, intermolecular free length, acoustic impedance and surface tension.

FTIR Spectral Analysis

Results of ultrasonic velocity and density measurement supported by FTIR spectral analysis. The change in transmittance and shift in frequency of the representative peaks -OH and other functional groups present in the compounds in FTIR spectra gives information about the complex formation between solute and solvent by molecular interaction. Here solute i.e., NPTGL has hydroxyl functional group and solvent has hydroxyl/carbonyl functional group. So hydrogen bonding between solute and solvent is possible as shown in Figs. 3–6. In IR spectra, when solute dissolved in solvent (ethanol/DMSO) then value of its IR absorption frequency is found to be different from the IR absorption frequency of pure solute. Alteration in value of frequency in presence of solvents indicates hydrogen bonding between solute and solvent.

The FTIR spectrum shows the frequency shift from 3488.33 cm^{-1} (enol form of solute) to 3397.69 cm^{-1} (solute in ethanol). Figure 5 clearly indicates the fre-

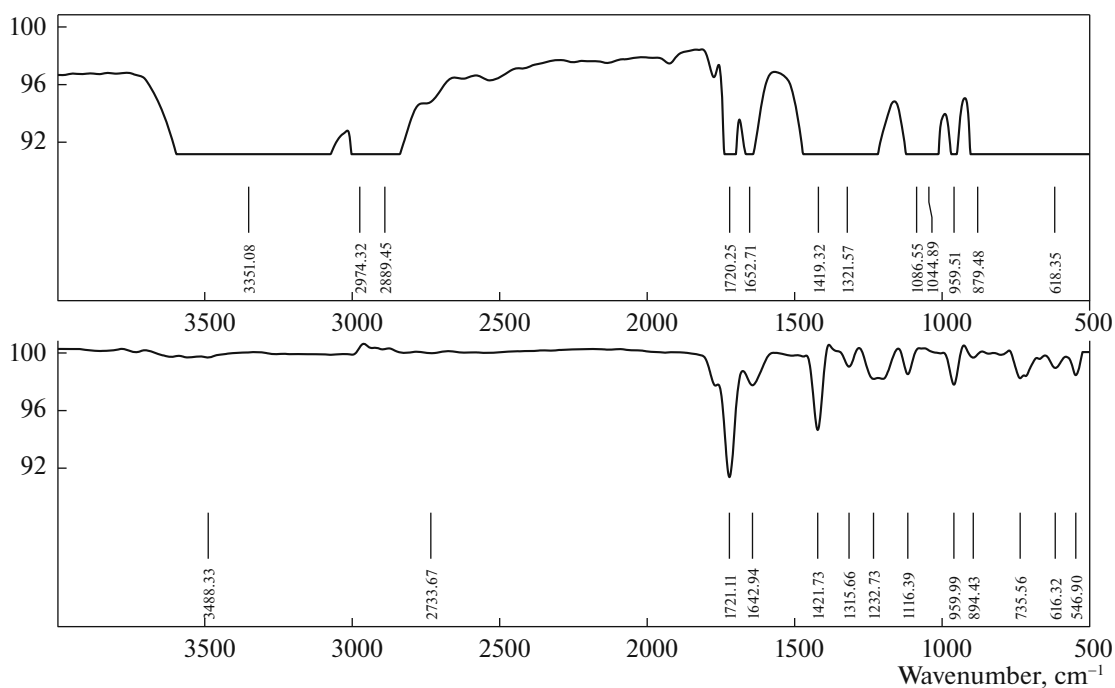


Fig. 5. Stacked structure of FT-IR spectrum of NPT-GL and solution of NPT-GL in EtOH.

quency shifts from 3488.33 cm^{-1} (solute–enol form) to 3351.08 cm^{-1} (solute + solvent ethanol) for —O—H stretching.

Although, other electronegative atoms i.e., oxygen and nitrogen are there in the structure of the solute, which are also available for hydrogen bonding with the hydrogen atom in —O—H group of ethanol. It is seen from the FTIR spectrum of binary mixture that shift in frequency of —OH group is more pronounced as that of other groups. Therefore, it can be concluded that the —OH group involved in hydrogen bonding. On the basis of the above observation, the proposed structure of binary mixture showing hydrogen bonding is shown in the Fig. 6.

CONCLUSION

The interaction between the molecules of liquids takes place due to various types of forces such as

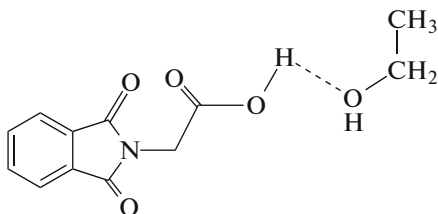


Fig. 6. Formation of hydrogen bonding between solute and ethanol.

charge transfer, hydrogen bonding, dipole–dipole and dipole–induced dipole interactions etc. We have measured density and ultrasonic velocity of *N*-phthaloyl amino acid analogue at various concentration as well as temperature and acoustical parameters such as adiabatic compressibility, intermolecular free length, Rao's constant, acoustic impedance, surface tension, molar volume, and Wada's constant calculated from the experimental velocity and density measurements. Thus the variation of various parameters with temperature and concentration indicates the molecular interaction is taking place in the liquid mixtures.

The acoustical and thermodynamic parameters calculated from measured properties suggest the strong molecular interaction within solute and solvent. All values of acoustical parameters are strongly correlated with each other. The solute–solute molecular association occurs due to dipole–dipole interaction and the polar nature of various molecular species in the mixture. The solute–solvent association occurs due to slightly polar solute and polar/nonpolar nature of the solvent. The association in this mixture is due to hydrogen bonding in the binary liquid mixtures. An analysis of these values indicates strong intermolecular interaction which may be due to hydrogen bond, dipole–dipole, hyperconjugation and charge transfer. The concept of intermolecular interaction explained on the basis of variation of acoustical parameters. Thus the interaction of solute with DMSO is more than that of ethanol.

REFERENCES

1. P. Tekade, S. Lohakare, S. Bajaj, and R. Naik, *Russ. J. Phys. Chem. A* **89**, 2105 (2015). doi 10.1134/S0036024415110187
2. S. D. Kukade, S. K. Singh, R. R. Naik, and S. V. Bawankar, *J. Mol. Liq.* **222**, 225 (2016). <https://doi.org/10.1016/j.molliq.2016.07.059>.
3. R. R. Naik, S. V. Bawankar, P. V. Tekade, and O. A. Mahodaya, *Russ. J. Phys. Chem. A* **89**, 152 (2015). doi 10.1134/S0036024415010227
4. S. J. Kharat, *J. Mol. Liq.* **140**, 10 (2008). <https://doi.org/10.1016/j.molliq.2007.12.006>.
5. A. Pal and S. Kumar, *J. Mol. Liq.* **121**, 148 (2005). <https://doi.org/10.1016/j.molliq.2004.12.003>.
6. K. Tamura, M. Maekawa, and T. Yasunaga, *J. Phys. Chem.* **81**, 2122 (1977). doi 10.1021/j100537a017
7. M. Iqbal and R. E. Verrall, *Canad. J. Chem.* **67**, 727 (1989). <https://doi.org/10.1139/v89-111>.
8. A. Bensen, W. Knoche, W. Berger, K. Giese, and S. Petrucci, *Ber. Bunsenges. Phys. Chem.* **82**, 678 (1978). doi 10.1002/bbpc.19780820703
9. A. Borthakur and R. Zana, *J. Phys. Chem.* **91**, 5957 (1987). doi 10.1021/j100307a029



Enhancement of photovoltaic performance of polyaniline/graphene composite-based dye-sensitized solar cells by adding TiO₂ nanoparticles

Kailash Nemade^{a,*}, Priyanka Dudhe^b, Pradip Tekade^b

^a Department of Physics, Indira Mahavidyalaya, Kalamb 445 401, India

^b Department of Chemistry, Jankidevi Bajaj College of Science, Wardha 442 001, India

ARTICLE INFO

Keywords:

Photovoltaic
Polyaniline
Graphene
TiO₂

ABSTRACT

Polyaniline (PANI)-graphene composites and polyaniline-graphene/TiO₂ composites were prepared by ex-situ approach. Systematic investigation was carried out to explore photovoltaic (PV) properties of PANi-graphene and PANi-graphene/TiO₂ composite. The prepared composites were characterized using X-ray diffraction (XRD), Scanning Electron Microscope (SEM), Raman Spectroscopy and Ultraviolet–Visible (UV–Vis) Spectroscopy. The PV properties of dye-sensitized solar cells (DSSCs) prepared composites investigated by assembling materials in ITO/PANi-graphene/Al and ITO/PANi-graphene/TiO₂/Al architecture. Different PV parameters such as short circuit current, open circuit voltage, fill factor and power conversion efficiency were determined from the (Current-Voltage) IV characteristics of PV cell. The 15 wt% PANi loaded graphene composite based PV cell shows optimized power conversion efficiency of the order 6.47%. The main accomplishment of present work is that efficiency associated with 15 wt% PANi loaded graphene composite, improved further by addition of TiO₂ nanoparticles. The composite system between PANi-graphene/TiO₂ for 1 wt% of TiO₂ nanoparticles shows optimized power conversion efficiency of the order 8.63%.

1. Introduction

Global demand of energy rising gradually, due to heavy industrialization and urbanization. Developed countries have huge demands of energy while demand is going on increasing in developing countries. The International Energy Agency states that energy needs are projected to expand by 55% till 2030 [1]. But unfortunately, the complete demand of energy is satisfied through non-renewable energy sources such as coal, petroleum, and natural gas. The exploitation of non-renewable energy sources results in range of adverse effects like air and water pollution, damage to public health, global warming and unnecessary atmospheric changes. Key solution for this issue is to use renewable energy sources such as hydropower, geothermal, wind and solar energy instead of non-renewable energy sources. Among these renewable energy sources, solar energy is best option due to outstanding characteristics such as the most abundant, inexhaustible and clean of all the renewable energy resources till date.

Across the globe researchers takes great interest in identification of alternative materials to silicon. The downside associated with silicon-based photovoltaic (PV) cell technology is their manufacturing requires costly ultra-high-purity silicon. Also, this process of manufacturing of PV cell results in significant carbon emission. Organic materials are

considered as close competitive and alternative to the standard silicon-based PV cell technology. The main causes behind the development of organic PV cell technology are less expensive, thinner, more flexible, and amenable to a wide range of lighting conditions. Another interesting reason is low material consumption results in a high absorption coefficient [2]. Some other advantages of organic PV cells are low specific weight, mechanical flexibility, tunable material properties and high transparency [3].

During literature survey on organic PV materials, we come across three efficient materials which exhibits outstanding PV properties. These three materials are polyaniline, graphene and TiO₂ nanoparticles. Among the conducting polymers such as polyaniline (PANI), polypyrrole (PPy) and polythiophene (PTh), PANi has been extensively studied by researchers.

Conducting polymer is the class of materials, which is fit for photovoltaic application and device fabrication. This is because of outstanding characteristics such as intrinsically stable photoexcitation with visible light, high photon harvesting efficiency, tunable band gap engineering on the entire visible spectral range and large charge generation when mixed with electron acceptor materials [4].

PANi display good electron conducting behaviors, interesting redox behavior, high environmental stability and controllable electrical and

* Corresponding author.

E-mail address: krnemade@gmail.com (K. Nemade).

<https://doi.org/10.1016/j.solidstatedsciences.2018.07.009>

Received 9 May 2018; Received in revised form 14 July 2018; Accepted 16 July 2018

Available online 17 July 2018

1293-2558/ © 2018 Elsevier Masson SAS. All rights reserved.

optical properties [5–7]. All these outstanding features of PANi attributed to the delocalized π -electron structure. The optical absorption coefficient of organic molecules specially in case of PANi is very high. Therefore, large amount of light can be trap by an insignificant amount of materials [8].

Graphene possesses a substantial number of wonderful optical and electronic properties, such as zero band-gap, semi-conducting with a high carrier mobility and high optical transparency, which generally not observed in other materials [9]. It is well accepted principle for organic PV cells that optimization of both charge transport and optical properties are necessary for good performance.

Out of many semiconducting metal oxides, TiO_2 has some attractive features for PV cell application. TiO_2 nanomaterial suitable for PV cell application due to its high chemical and optical stability, non-toxicity, low cost, corrosion resistance and ease of synthesis [10,11]. Many reports show that graphene- TiO_2 nanocomposites possess superior photovoltaic properties than pristine TiO_2 [12].

The composite preparation using organic and inorganic constituent's results in improved electronic properties. It is well known principle of materials science that in synergetic state, physical and chemical properties of most of the composite improves. Therefore, in this section it is analyzed using some reports on PV properties of PANi-Metal Oxide composite. The addition of metal oxides impurity in PANi enhance the PV properties and increase the efficiency of solar cells.

Ameen et al. fabricated TiO_2 /PANi and dye absorbed TiO_2 /PANi electrodes by plasma polymerization for solar cells application. The results of the study indicate that dye absorbed TiO_2 /PANi electrode based DSSCs have high charge carrier transportation between the TiO_2 and PANi layer. This rapid charge transportation in dye absorbed TiO_2 /PANi electrode improves the performance of solar cell than the TiO_2 /PANi electrode [13]. Shen et al. architecture PV cell with layers ITO/nano-crystalline TiO_2 /PANi/Aluminum. This shows largest open voltage of 0.397 V and short current density of $65.9 \mu\text{A}/\text{cm}^2$ under simulated solar radiation. Using current-voltage characteristics, the formation of p-n junction between nano-crystalline TiO_2 and PANi interface is also verified [14]. Yang et al. synthesized grafted aniline on amino-benzoate monolayer to adsorbed TiO_2 nanocrystal to fabricate a uniform core/shell structured TiO_2 /PANi nanocomposite. The DSSC fabricated with an electrode of TiO_2 /PANi film have considerably high short circuit current density of $0.19 \text{ mA}/\text{cm}^2$ and an open circuit voltage of 0.35 V [15]. Zhu et al. adopted the two-step process to prepared PANi hybridized ZnO photoanode on FTO substrate. The results of the study show that light-conversion efficiency of PANi hybridized ZnO nanograin improves by 60% than pure ZnO nanograin photoanode [16]. Momeni et al. studied the dye-sensitized solar cell based on TiO_2 nanotube arrays. In this work, TiO_2 nanotubes were prepared by two different approaches namely one-step and two-step process. This work concludes that TiO_2 nanotubes prepared using two-step process shows higher efficiency [17]. Bahramian et al. prepared in situ PANi-based counter electrode and coral-like TiO_2 to assemble DSSC with transparent PANi films as counter electrode. This bifacial DSSC have power conversion efficiency of 8.22%, which is assigned to excellent light scattering by the coral-like TiO_2 and high specific surface area of PANi nanofibers [18]. Duan et al. fabricated the DSSC with PANi incorporated TiO_2 anodes, PANi counter electrodes, and iodide doped PANi solid-state electrolytes. The results of the study show that DSSC with proper assembly process and iodide dosage provides good PV performances with power conversion efficiency of 3.1% [19].

The humankind has been gifted by many brilliant materials by nature, one of those is Graphene. Graphene possess noticeable enigmatic optical and electronic properties such as zero band gap, high carrier mobility, high optical transparency. The synergetic phase of graphene with PANi, also results in efficient PV materials. Some reports on PANi-Graphene composite have been reviewed in this section.

Wang et al. prepared graphene/PANi nanocomposite by polymerization of aniline monomer in situ method. In DSSC, graphene/

PANi nanocomposite deposited on FTO, which gives power conversion efficiency of 6.09% compared to 6.88% of efficiency for PV cell with expensive Pt counter electrode under similar experimental conditions [20]. Liu et al. designed DSSC by coating a nanocomposite thin film of graphene/PANi on FTO glass by electro-polymerization method. In comparison, graphene/PANi based electrode has power conversion efficiency of 7.17%, which is close to 7.24% of a DSSC with a Pt counter electrode. This study shows that graphene/PANi electrode has potential to replace conventional Pt counter electrode in DSSC [21]. Dinari et al. designed the Pt free DSSC using PANi-Graphene quantum dots by in situ electrochemical polymerization on FTO coated glass. The synergistic effect between PANi and graphene quantum dots provides higher electrochemical catalytic activity which resulted into improved PV performance with power conversion efficiency of 1.6% [22].

Loryueng et al. fabricated DSSCs with counter electrode based on PANi-graphene hybrid material. The counter electrode was prepared by depositing material on FTO by drop casting method. The PANi/graphene hybrid counter electrode exhibits superior PV performance with open circuit voltage of 0.57 V, Short Circuit Current of $5.15 \text{ mA}/\text{cm}^2$, fill factor of 0.40 and power conversion efficiency of 1.16% which results in improved PV performance than DSSC based on Pt electrode [23]. Yang et al. synthesized multilayer counter electrodes from positively charged PANi-graphene complex and negatively charged platinum nanoparticles with different number of layers and different concentration of graphene in PANi-graphene complex. This work concludes that the electron migration from graphene to PANi helped in good charge transfer. This multilayer interface based DSSC has power conversion efficiency of 7.45%. This work also pointed that multi-interfacial counter electrodes are suitable for robust DSSC [24].

During literature survey, it is observed that PANi, TiO_2 nanoparticles and Graphene have much potential to improve their PV properties. The necessity of development of new kinds of PV materials with improved power conversion efficiencies is being touched by different research groups across the globe. Therefore, the problem is identified on the basis of following remarks:

- During study, it is observed that concentration of impurity in composite has play crucial role. Therefore, in this work it planned to investigate optimized composition of PV material based on PANi and graphene.
- In second step, after successful finding of optimized composition, another impurity that is TiO_2 used for further enhancement of PV properties of PANi-graphene composite.

Therefore, the objectives of present work are to prepare and optimized PV properties of PANi-graphene composite. Then prepare and optimized TiO_2 nanoparticles loaded PANi-graphene composite for PV application.

2. Experimentation

2.1. Preparation of materials

2.1.1. Preparation of PANi

In the present work, PANi was synthesized by using chemical oxidative method. In this method, ammonium persulfate was used as an oxidizing agent. All chemicals required for the preparation of PANi procured from SD fine, India of AR grade and used without further purification. In the process of preparation of PANi, following steps were executed,

- During the synthesis of PANi, one condition is imposed on molar ratio between ammonium persulfate to aniline monomer should not exceed the ratio ≤ 1.15 . The reason behind this condition is to obtain high conductivity and yield [25].
- With this condition, both aniline monomer and ammonium

persulfate dissolve separately in aqueous (100 ml) medium.

- Subsequent to this step, the solution of aniline monomer was added in ammonium persulfate solution in dropwise manner under magnetic stirring.
- The greenish-black precipitate was observed in beaker with increase in temperature.
- This precipitate was kept for overnight (24 h) for good quality polymerization.
- On next day, precipitate was washed three times with distilled water to remove un-reacted contents in product.
- The obtained product was dried at 50 °C and used for further process.

2.1.2. Preparation of PANi/Graphene composites

The *ex-situ* approach was adopted for the preparation of PANi/Graphene composite. The graphene required for the composite preparation was prepared by previously reported method [26]. The weight % (wt.%) stoichiometry was adopted for the preparation of composites. The wt.% stoichiometry was calculated using relation (Eq. (3.1)),

$$\text{wt. \%} = \frac{A}{(A + B)} \times 100 \quad (3.1)$$

where A and B are constituents of composite.

In our case, the content of PANi in composite was varied for 5–20 wt % by an interval of 5 wt%. In this way, four samples were obtained. During preparation of composite, both constituents of composite was added in 25 ml acetone under magnetic stirring at room temperature.

2.1.3. Preparation of PANi/graphene-TiO₂ composites

PANi/Graphene-TiO₂ composites was also prepared by *ex-situ* approach. In this process, TiO₂ was directly procured from SD fine, India of high purity. This TiO₂ was probe sonicated using sonicator (PCI, 750-F, PCI Analytics Pvt Ltd). This process of probe sonication, splits the TiO₂ particles up to the nano-dimensions. As-obtained TiO₂ nanoparticles, was used for the preparation of composites. By adopting wt.% stoichiometry, four samples of PANi/Graphene-TiO₂ composites were prepared by varying content of TiO₂ nanoparticles in composite from 0.5 to 2 wt% by an interval of 0.5 wt%. The optimized stoichiometry between PANi and graphene were used further for addition of TiO₂ nanoparticles, to improve PV properties. Here also, acetone was used as an organic media for the preparation of composites. For dye sensitization process, Ru-based N719 dye was used by preparing media of 0.25 mM ethanolic solution of dye N719.

2.2. Fabrication of photovoltaic cell

The doctor blade technique was used to fabricate the PV cells. During this process, the composites was sandwiched between cleaned ITO plate as transparent electrode and Aluminum electrode. The aluminum foil was used as metallic electrode for the PV cell. ITO plate (Dimension: 25 mm × 25 mm) used in this work was procured from Techinstro (ITO-SE-011), India. With the help of temporary binder (based on 3% ethyl cellulose and 97% butyl digol), composite was deposited on ITO electrode and then Aluminum electrode was deposited. This fabricated cell allows to dry at 40 °C for 3 h for evaporation of volatile organic compounds. The thickness of deposited layer controlled by thickness of transparency used during doctor blade technique. In this way, PV cells were fabricated for further study. The side face of fabricated PV cell is depicted in Fig. 1.

2.3. Measurements of photovoltaic characteristics

The current-voltage (IV) characteristics of PV cell collected under incandescent light bulb of power 0.2956 Watt/m². The separation between incandescent light source and PV cell was about 15 cm. The important diode parameters like open circuit voltage (V_{OC}), short

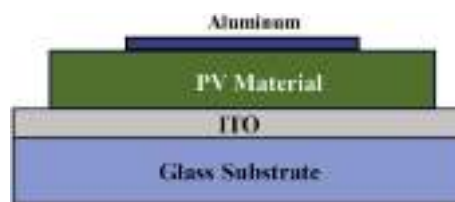


Fig. 1. Side face of fabricated PV cell.

circuit current (I_{SC}), fill factor (FF), and power conversion efficiency (η) were measured under these conditions, which reproduced without any considerable deviation. The FF of PV cell computed using relation Eq. [1] [27]:

$$FF = \frac{I_{MAX} \times V_{MAX}}{I_{SC} \times V_{OC}} \quad (1)$$

Whereas, power conversion efficiency (%η) of PV cell estimated using the relation Eq. [2]. [28],

$$\% \eta = \left(\frac{I_{SC} \times V_{OC} \times FF}{P_{in}} \right) \times 100 \quad (2)$$

The FF and %η are the crucial parameters for any PV cell. On the basis of these parameters, it is possible to discriminate any PV cell and its performance.

3. Results and discussion

3.1. Materials characterization and PV properties of PANi/Graphene

3.1.1. XRD analysis

Fig. 2 (a) shows the XRD pattern of pure PANi synthesized by chemical oxidative method. The XRD pattern of pure PANi comprises only one broad peak around 26°, which indicates the poor crystallinity phase of PANi. This broad peak is also assigned to the scattering from the PANi chains at inter planar spacing [29]. Fig. 2 (b) depicts XRD pattern of graphene, which has well structural, and phase purity. The XRD of graphene possesses two signature peaks at 26.3° (002) and 44.2° (100). The peak at 2θ = 26.3° indicates well organized structure of graphene with an interlayer spacing of 0.339 nm. This layer spacing is

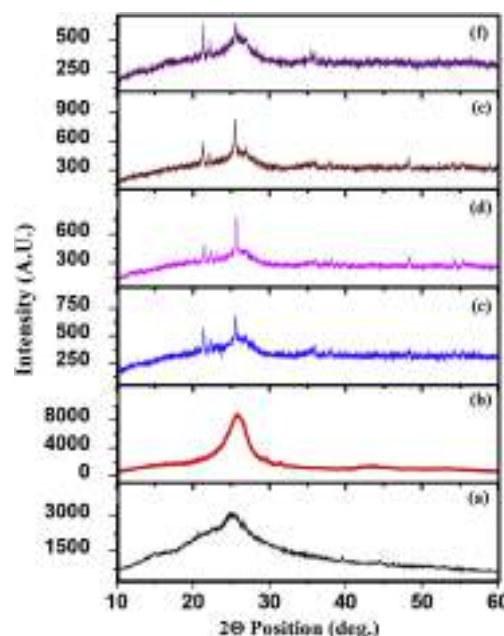


Fig. 2. XRD pattern of pure (a) PANi, (b) graphene and (c) 5 wt%, (d) 10 wt%, (e) 15 wt%, (f) 20 wt% PANi loaded graphene composites.

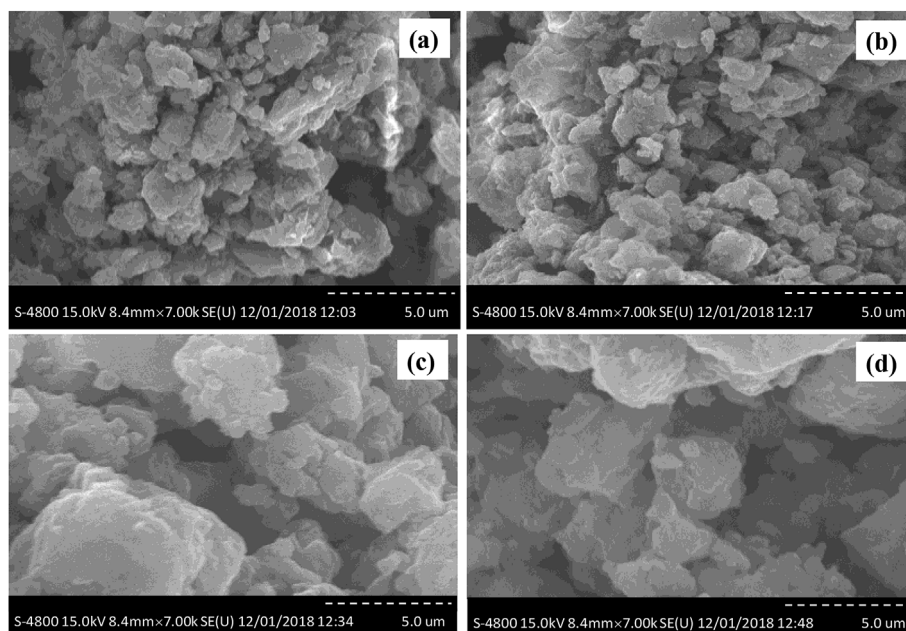


Fig. 3. SEM images of (a) 5 wt%, (b) 10 wt%, (c) 15 wt% and (d) 20 wt% PANi loaded graphene composites.

in agreement with spacing in graphite. The broad peak at $2\theta = 44.2^\circ$ is attributed to presence of some defects [30]. Fig. 2 (c, d, e and f) shows the XRD pattern of 5 wt%, 10 wt%, 15 wt% and 20 wt% PANi loaded graphene composites, respectively. XRD pattern shows that with an increase in PANi content in composites, noisy behavior of pattern increases. This indicates that crystalline nature of composites decreases. Sharp peaks appear between 20 and 26° is attributed to the presence of smaller crystalline regimes in composites. The decrease in peak height intensity of composites than graphene and PANi, justify the formation of composites.

3.1.2. Morphology study

Fig. 3 shows the SEM images of (a) 5 wt%, (b) 10 wt%, (c) 15 wt% and (d) 20 wt% PANi loaded graphene composites prepared by ex-situ approach. In all cases, graphene sheets are homogeneously dispersed in PANi. At fixed resolution, one thing is observed from SEM images that agglomeration phenomenon increases with wt.% of PANi. All composite samples have irregular shape.

3.1.3. Raman Spectroscopy

Fig. 4 depicts the Raman spectra of 15 wt% PANi loaded graphene composite, which is optimized sample in PV study. The C–N stretching vibration from benzenoid structure appears through band 1548 cm^{-1} . The semi-benzenoid polaronic band of C–N⁺ appears at 1318 cm^{-1} and plane bending vibration of CH is appears at 1200 cm^{-1} . The Raman spectrum comprises clear band D (1325 cm^{-1}) [31], G (1598 cm^{-1}),

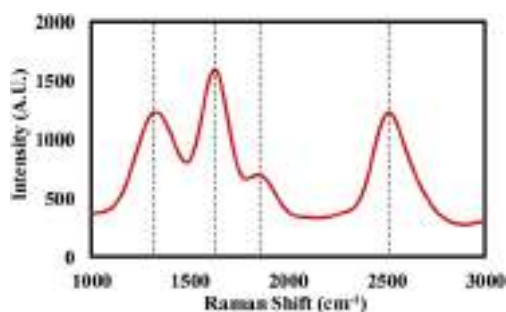


Fig. 4. Raman spectrum of 15 wt% PANi loaded graphene composite.

and 2D (2695 cm^{-1}), which are signature band of graphene [32–34]. The shift in band position is observed, which is attributed to the structural changes in resultant composite. The quinoid rings in the PANi have a similar atomic structure with the C6 rings of graphene. This situation in both constituents allow for a strong π - π stacking interaction and beneficial for electronic transmission [35].

3.1.4. Optical properties

In PV technology, optical properties of PV materials play crucial role. Therefore, in our case it is studied using UV-VIS spectroscopy. In PV cell technology, both types of band gap materials that is low-band gap and high-band gap materials have their own importance. Therefore, by combining appropriate materials to obtain band gap which efficiently used available solar radiations is necessary. This is necessary, if the band gap is very small than incident photon energy, then considerable photon energy converted in heat energy, which raise the temperature of PV materials. On other hand, if the band gap is very large, it restricts the transition between valance band to conduction band [36].

Fig. 5 shows the UV-VIS spectrum of 5 wt%, 10 wt%, 15 wt% and 20 wt% PANi loaded graphene composites. From plot, it is clearly

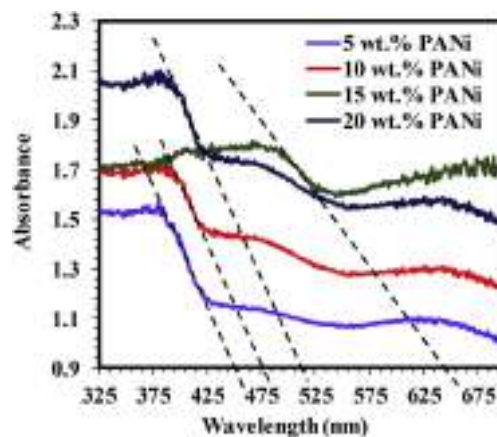


Fig. 5. UV-VIS spectrum of 5 wt%, 10 wt%, 15 wt% and 20 wt% PANi loaded graphene composites.

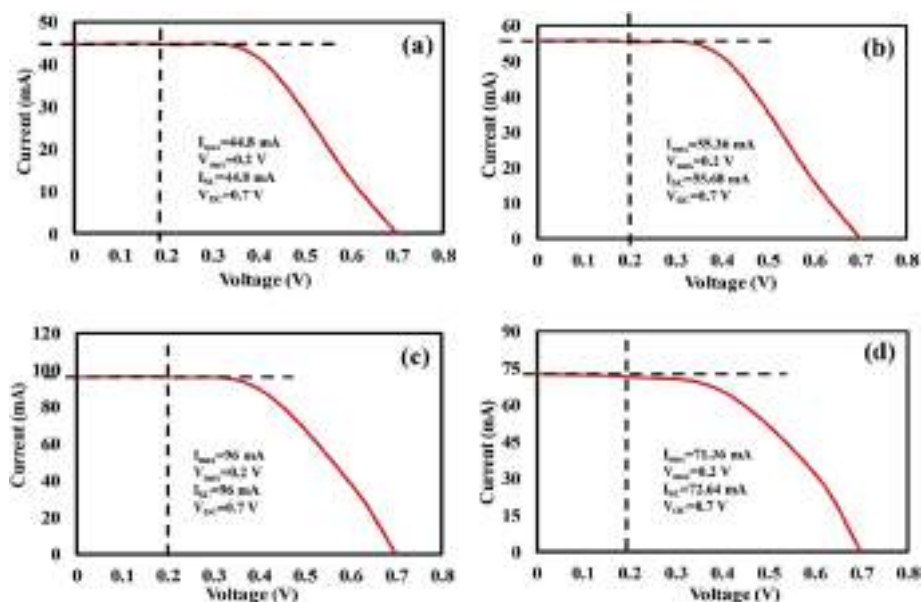


Fig. 6. PV response of (a) 5 wt%, (b) 10 wt%, (c) 15 wt% and (d) 15 wt% PANi loaded graphene composite.

observed that the samples 5 wt%, 10 wt% and 20 wt% PANi loaded graphene composites have absorption tail at lower wavelength than 15 wt% PANi loaded graphene composites. The band gap values for as-prepared composite samples (estimated using frequency-wavelength relation) ranges between 2.73 and 1.92 eV. The lowest value of band gap is associated with 15 wt% PANi loaded graphene composite.

3.1.5. PV performance

Fig. 6 shows the PV response of (a) 5 wt%, (b) 10 wt%, (c) 15 wt% and (d) 15 wt% PANi loaded graphene composite based DSSCs. All diode parameters like I_{\max} , V_{\max} , I_{SC} , V_{OC} , FF and $\% \eta$ are provided in Table 1. Among all PV cells, the response of 15 wt% PANi loaded graphene composite has highest power conversion efficiency of order 6.479% (FF = 0.285). The highest power conversion efficiency was attributed to lower band gap value (1.92 eV) of 15 wt% PANi loaded graphene composite. All samples have stable diode parameters and reproducible results.

Fig. 7 shows the variation of FF and $\% \eta$ as a function wt.% of PANi in composite. Plot shows that 15 wt% PANi loaded graphene composite has highest power conversion efficiency. The possible reason for highest power conversion efficiency may be

Table 1

PV parameters of TiO₂ nanoparticles loaded PANi-graphene composites and PANi loaded graphene composites.

TiO ₂ nanoparticles loaded PANi-graphene composite						
Wt.% of TiO ₂ nanoparticles	I_{\max} (mA)	V_{\max} (V)	I_{SC} (mA)	V_{OC} (V)	FF	$\% \eta$
0.5 wt%	95.17	0.2	95.23	0.8	0.2499	6.43
1 wt%	127.71	0.2	127.79	0.8	0.2498	8.63
1.5 wt%	106.59	0.2	106.65	0.8	0.2498	7.21
2.0 wt%	105.73	0.2	105.8	0.8	0.2498	7.15
PANi loaded graphene composite						
Wt.% of PANi	I_{\max} (mA)	V_{\max} (V)	I_{SC} (mA)	V_{OC} (V)	FF	$\% \eta$
5 wt%	44.8	0.2	44.8	0.7	0.285	3.068
10 wt%	55.36	0.2	55.68	0.7	0.284	3.741
15 wt%	96	0.2	96	0.7	0.285	6.479
20 wt%	71.36	0.2	72.64	0.7	0.280	4.816

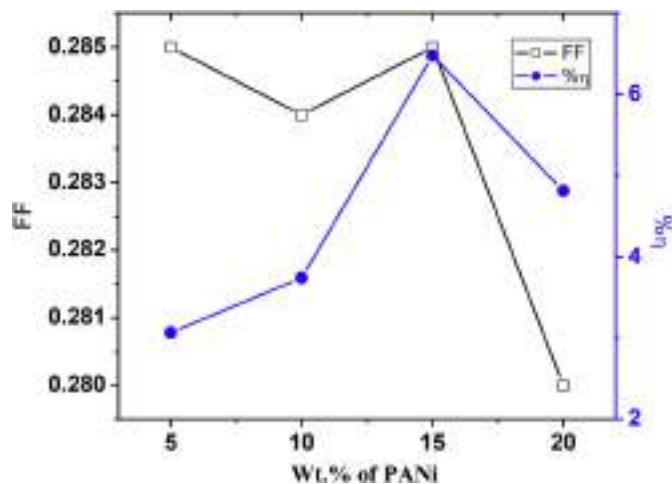


Fig. 7. Variation of FF and $\% \eta$ as a function wt.% of PANi in composite.

- the homogeneous presence of PANi and graphene in composite, can reduce the interfacial resistance between the graphene and the PANi. This homogeneity in composite results in better electron transfer.
- The presence of high electrical conductive graphene in composite and agglomerated nature of composite reduce inter-domain resistance.
- Lower band gap (1.92 eV) value of 15 wt% PANi loaded graphene composite.

3.2. Improvement in PV performance by addition of TiO₂ nanoparticles

3.2.1. XRD analysis

Fig. 8 (a) shows the XRD pattern of anatase phase TiO₂ nanoparticles. The strong signature peaks at 25° and 48° confirms the anatase phase. All remaining peaks position and marginal intensity data are in good agreement with standard spectrum (JCPDS card No. 84–1286) [37]. The average crystallite size of TiO₂ nanoparticles was estimated using Scherrer equation [38], $D = (K\lambda / \beta \cos\theta)$, where D is average crystallite size (nm), k is a shapes factor (K = 0.89), λ is the wavelength of X-ray source equals 1.540 Å, β is the full width at half maxima, and θ is the diffraction peak angle. The average crystallite size of TiO₂

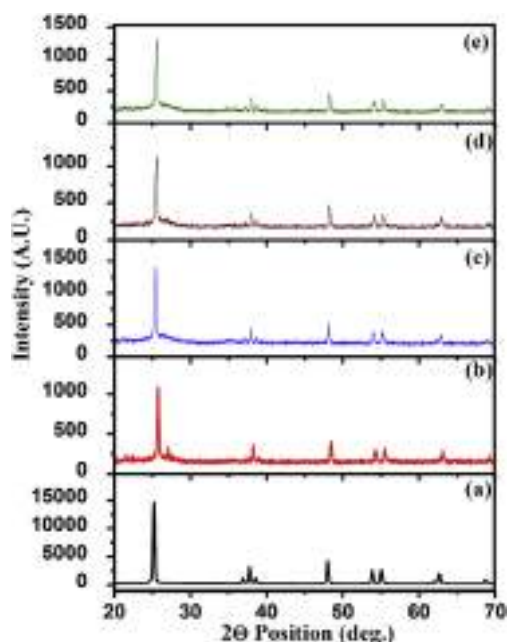


Fig. 8. XRD pattern of pure (a) TiO₂ nanoparticles and (b) 0.5 wt%, (c) 1 wt%, (d) 1.5 wt% and (e) 2 wt% TiO₂ nanoparticles loaded PANi-graphene composites.

nanoparticles was found to be 51.27 nm. Fig. 8 (b, c, d and e) depicts the XRD pattern of 0.5 wt%, 1 wt%, 1.5 wt% and 2 wt% TiO₂ nanoparticles loaded PANi-graphene composites, respectively. The addition of TiO₂ nanoparticles in PANi-graphene composites results in interesting results. The XRD pattern clearly shows the composite exhibits the crystalline phase with shape peaks. As discussed in section 4.1.1, the PANi-graphene composites have amorphous phase, which was diminish by addition of TiO₂ nanoparticles.

3.2.2. Morphology study

Fig. 9 represents the SEM images of (a) 0.5 wt%, (b) 1 wt%, (c) 1.5 wt% and (d) 2 wt% TiO₂ nanoparticles loaded PANi-graphene composites. Here also, TiO₂ nanoparticles nicely dispersed in PANi-

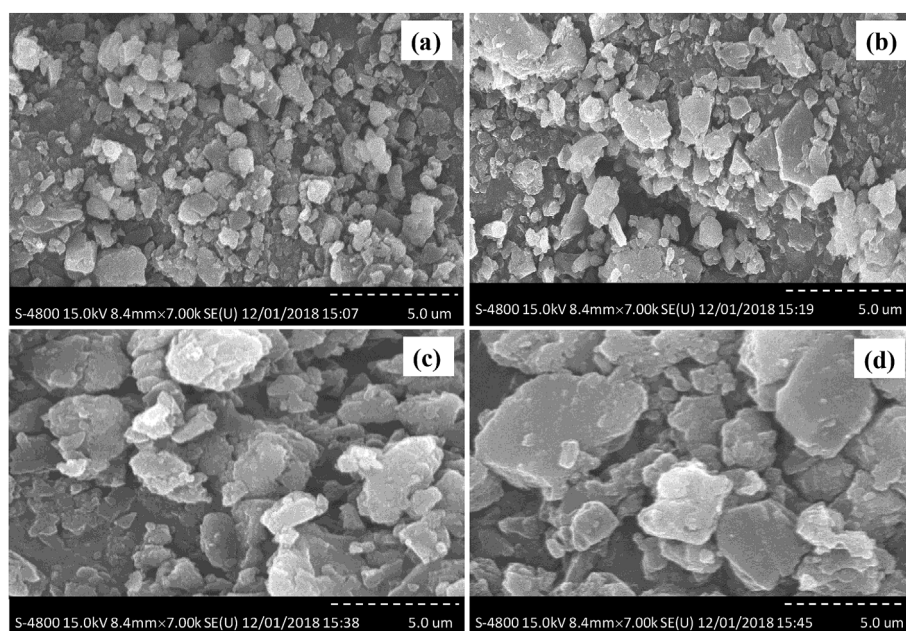


Fig. 9. SEM images of (a) 0.5 wt%, (b) 1 wt%, (c) 1.5 wt% and (d) 2 wt% TiO₂ nanoparticles loaded PANi-graphene composites.

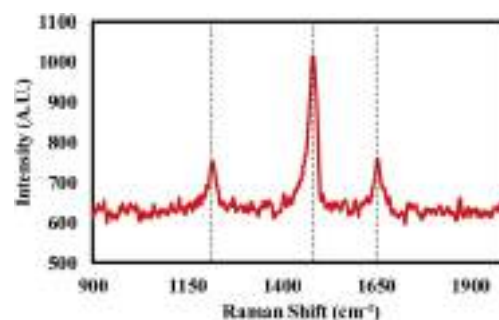


Fig. 10. Raman spectrum of 1 wt% TiO₂ nanoparticles loaded PANi-graphene composite.

graphene composites. The addition of TiO₂ in PANi-graphene results in improvement of crystallinity. In all SEM images, well defined crystalline boundaries are observed. The crystallinity of all composite samples reflects also from XRD analysis. The irregular particle size distribution observed in all regions of SEM.

3.2.3. Raman Spectroscopy

Fig. 10 shows the Raman spectrum of 1 wt% TiO₂ loaded PANi-Graphene composite. This spectrum also comprises the C–N stretching vibration from benzenoid, which appears around 1548 cm⁻¹. Similarly, semi-benzenoid polaronic band of C–N⁺ appears around 1318 cm⁻¹ and plane bending vibration of C–H is appears around 1200 cm⁻¹. No significant peaks were associated with TiO₂ nanoparticles in spectrum.

3.2.4. Optical properties

Fig. 11 shows the UV-VIS spectrum of 0.5 wt%, 1 wt%, 1.5 wt% and 2 wt% TiO₂ nanoparticles loaded PANi-graphene composites. From the plot, it is clear that absorption tail of 1 wt% TiO₂ nanoparticles loaded PANi-graphene composite has higher value than other three samples. The band gap values of 0.5 wt%, 1 wt%, 1.5 wt% and 2 wt% TiO₂ nanoparticles loaded PANi-graphene composites ranges between 3.02 and 2.53 eV. The lowest value of band gap is associated with 1 wt% TiO₂ nanoparticles loaded PANi-graphene composite.

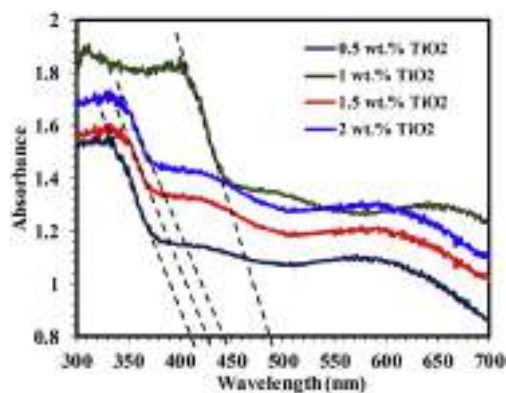


Fig. 11. UV-VIS spectrum of 0.5 wt%, 1 wt%, 1.5 wt% and 2 wt% TiO₂ nanoparticles loaded PANi-graphene composites.

3.2.5. PV performance

Fig. 12 shows the PV response of (a) 0.5 wt%, (b) 1 wt%, (c) 1.5 wt% and (d) 2 wt% TiO₂ nanoparticles loaded PANi-graphene composites based DSSCs and all diode parameters listed in Table 1. In PANi-graphene/TiO₂ composite, stable diode parameters observed. From Table 1, it is observed that 1 wt% TiO₂ nanoparticles loaded PANi-graphene composite has highest power conversion efficiency. The highest power conversion efficiency was attributed to good optical properties and lower band gap (2.53 eV) value.

Fig. 13 depicts the variation of FF and % η as a function wt.% of TiO₂ nanoparticles in PANi-graphene composites. The highest power conversion efficiency was associated with 1 wt% of TiO₂ nanoparticles in PANi-graphene composite. The possible reasons for the highest power conversion are,

- The addition of TiO₂ nanoparticles in PANi-graphene composite, results in increase of both photocurrent density and open circuit voltage.
- The presence of graphene sheets in composite reduces charge recombination and increasing open circuit voltage as a result of high electron [39,40].

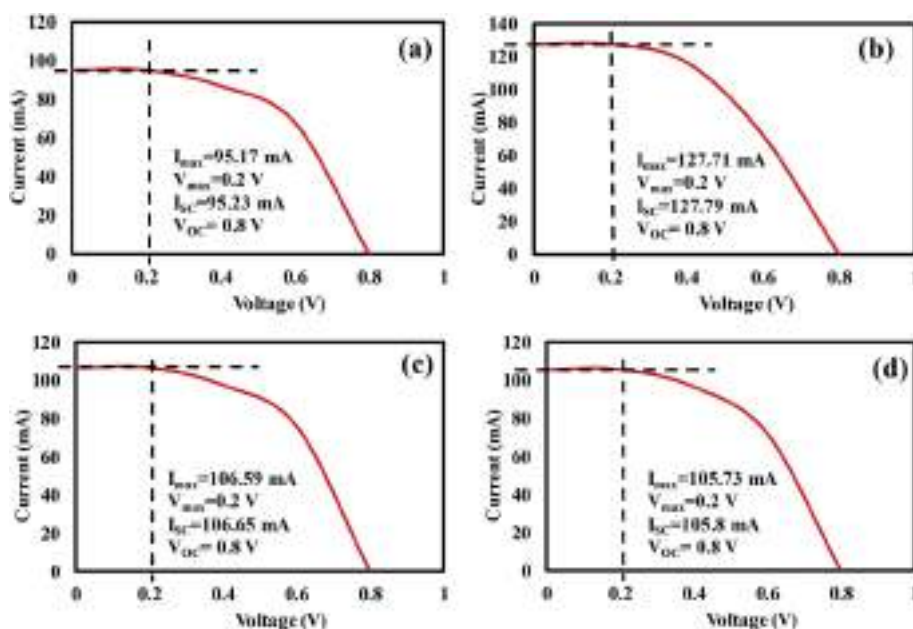


Fig. 12. PV response of (a) 0.5 wt%, (b) 1 wt%, (c) 1.5 wt% and (d) 2 wt% TiO₂ nanoparticles loaded PANi-graphene composites.

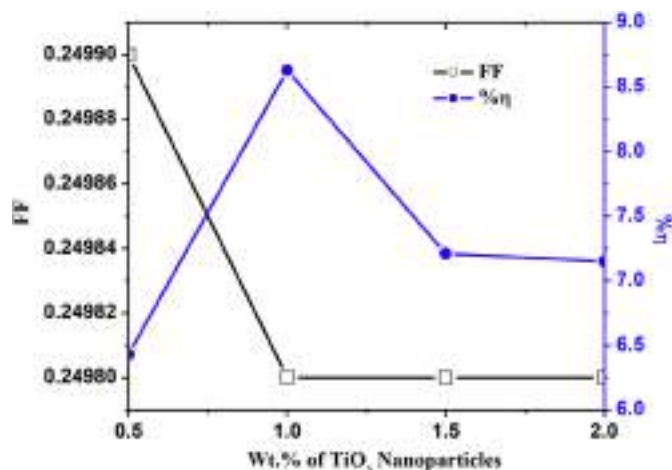


Fig. 13. Variation of FF and % η as a function wt.% of TiO₂ nanoparticles in composites.

4. Conclusions

During the study, two material systems that is PANi-graphene composite and PANi-graphene/TiO₂ composites based DSSCs were successfully prepared by ex-situ approach. The structural, morphological and optical study of both systems were carried out to understand physical properties of materials. To analyze the PV performance of PANi-graphene composite and PANi-Graphene/TiO₂ composites, PV cells were fabricated using doctor bleed technique in architecture ITO/PV materials/Aluminum.

The PANi required for composite preparation was synthesized by using chemical oxidative route successfully. During composite preparation wt.% of PANi varied in graphene, to analyze effect of PANi on PV properties of composite. In this study, 15 wt% PANi loaded graphene composite shows optimized power conversion efficiency of order 6.47% with I_{sc} = 96 mA. The highest power conversion efficiency of this sample attributed to reduction in the interfacial resistance between the graphene and the PANi, lower inter-domain resistance and lower band gap of 15 wt% PANi loaded graphene composite than other samples.

In order to improve further the power conversion efficiency of 15 wt % PANi loaded graphene composite, TiO₂ nanoparticles were added in this composite. To obtain again optimized sample with outstanding PV properties, the content of TiO₂ nanoparticles were varied with 0.5–2 wt % by an interval of 0.5 wt%. In this study, 1 wt% TiO₂ nanoparticles loaded PANi-graphene composite shows optimized PV properties. The power conversion efficiency was successfully improved and its value was found to be 8.63%. This is the main accomplishment of present work. In this complete, it is also observed that diode parameters have stable value.

In the concluding remark of this work, it is underlined that concentration of impurity in composite play very important role. Similarly, band gap engineering is also necessary to fabricate more efficient PV cells.

Data availability

The datasets generated during the current study are available from the corresponding author on reasonable request.

Acknowledgements

Authors are very much thankful to Dr. S.K. Omanwar, Head, Department of Physics, Sant Gadge Baba Amravati University, Amravati for providing the facility of Probe Sonicator. Authors are also grateful to Dr. Om Mahodaya, Principal, Jankidevi Bajaj College of Science, Wardha for providing necessary facilities for this work.

Appendix A. Supplementary data

Supplementary data related to this article can be found at <https://doi.org/10.1016/j.solidstatedciences.2018.07.009>.

References

- [1] <https://www.bbc.co.uk/education/guides/zpmmmp3/revision>.
- [2] Y. Liu, X. Wan, F. Wang, J. Zhou, G. Long, J. Tian, J. You, Y. Yang, Y. Chen, *Advanced Energy Materials* 1 (2011) 771–775.
- [3] G. Dennler, M.C. Scharber, C.J. Brabec, *Adv. Mater.* 21 (2009) 1323–1338.
- [4] H.S. Nalwa, *Handbook of Organic Conductive Molecules and Polymers*, John Wiley & Sons, Chichester, UK, 1997.
- [5] E.W. Paul, A.J. Ricco, M.S. Wrighton, *J. Phys. Chem.* 89 (1985) 1441–1447.
- [6] C.R. Kagan, D.B. Mitzi, C.D. Dimitrakopoulos, *Science* 286 (1999) 945–947.
- [7] S.A. Chen, Y. Fang, *Synth. Met.* 60 (1993) 215–222.
- [8] L.D. Pulfrey, *Photovoltaic Power Generation*, Van Nostrand Reinhold Co., New York, 1978.
- [9] H.K. Bisoyi, S. Kumar, *Liq. Cryst.* 38 (2011) 1427–1449.
- [10] O. Carp, C.L. Huisman, A. Reller, *Prog. Solid State Chem.* 32 (2004) 33–177.
- [11] D. Dambournet, I. Belharouak, K. Amine, *Chem. Mater.* 22 (2010) 1173–1179.
- [12] E. Singh, H.S. Nalwa, *Sci. Adv. Mater.* 7 (2015) 1863–1912.
- [13] S. Ameen, M.S. Akhtar, G. Kim, Y.S. Kim, O. Yang, H. Shin, *J. Alloy. Comp.* 487 (2009) 382–386.
- [14] L. Shen, W. Guo, H. Xue, Z. Liu, J. Zhou, C. Liu, W. Chen, *Proceedings of the 3rd IEEE Int. Conf. on Nano/Micro Engineered and Molecular Systems*, January 6–9, (2008) (Sanya, China).
- [15] S. Yang, Y. Ishikawa, H. Itoh, Q. Feng, *J. Colloid Interface Sci.* 356 (2011) 734–740.
- [16] S. Zhu, W. Wei, X. Chen, M. Jiang, Z. Zhou, *J. Solid State Chem.* 190 (2012) 174–179.
- [17] M.M. Momeni, M.G. Hosseini, *J. Mater. Sci., Mater. Electron* 25 (2014) 5027–5034.
- [18] A. Bahramian, D. Vashae, *Sol. Energy Mater. Sol. Cells* 143 (2015) 284–295.
- [19] Y. Duan, Y. Chen, Q. Tang, Z. Zhao, M. Hou, R. Li, B. He, L. Yu, P. Yang, Z. Zhang, *J. Power Sources* 284 (2015) 178–185.
- [20] G. Wang, S. Zhuo, W. Xing, *Mater. Lett.* 69 (2012) 27–29.
- [21] C. Liu, K. Huang, P. Chung, C. Wang, C. Chen, R. Vittal, C. Wu, W. Chiu, K. Ho, *J. Power Sources* 217 (2012) 152–157.
- [22] M. Dinari, M.M. Momeni, M. Goudarzirad, *J. Mater. Sci.* 51 (2016) 2964–2971.
- [23] V. Loryuenyong, S. Yaotrakoo, P. Prathumted, J. Lertsiri, A. Buasri, *Micro & Nano Lett.* 11 (2016) 77–80.
- [24] P. Yang, J. Duan, D. Liu, Q. Tang, B. He, *Electrochim. Acta* 173 (2015) 331–337.
- [25] A.A. Syed, M.K. Dinesan, *Talanta* 38 (1991) 815–837.
- [26] K.R. Nemade, S.A. Waghuley, *J. Electron. Mater.* 42 (2013) 2857–2866.
- [27] T. Salmi, M. Bouzguenda, A. Gastli, A. Masmoudi, *Int. J. Renew. Energy Resour.* 2 (2012) 213–219.
- [28] M. Seifi, A. Soh, N. Izzrib, A. Wahab, M.K.B. Hassan, *International Journal of Electrical, Robotics, Electronics Communication Engineering* 7 (2013) 97–103.
- [29] W. Feng, E. Sun, W.A. Fujii, H.C. Niihara, K. Yoshino, *Bull. Chem. Soc. Jpn.* 73 (2000) 2627–2632.
- [30] Y. Wu, B. Wang, Y. Ma, Y. Huang, N. Li, F. Zhang, Y. Chen, *Nano Research* 3 (2010) 661–669.
- [31] A. Ferrari, J. Robertson, *Phys. Rev. B* 61 (2000) 14095–14099.
- [32] L. Cancado, M. Pimenta, B. Neves, M. Dantas, A. Jorio, *Phys. Rev. Lett.* 93 (2004) 247401–247405.
- [33] A.C. Ferrari, *Solid State Commun.* 143 (2007) 47–57.
- [34] A.C. Ferrari, J. Robertson, *Phys. Rev. B* 61 (2000) 14095–14107.
- [35] R. Wang, Y. Wang, C. Xu, J. Sun, L. Gao, *RSC Adv.* 3 (2013) 1194–1200.
- [36] <https://www.e-education.psu.edu/eme812/node/534>.
- [37] K. Thamaphat, P. Limsuwan, B. Ngotawornchai, J. Kasetsart, *Nat. Sci.* 42 (2008) 357–361.
- [38] K.R. Nemade, S.A. Waghuley, *AIP Conference Series* 1536 (2013) 1258–1259.
- [39] L. Yang, W.W.F. Leung, *Adv. Mater.* 25 (2013) 1792–1795.
- [40] A. Kongkanand, R.M. Dominguez, P.V. Kamat, *Nano Lett.* 7 (2007) 676–680.



Research paper

Strengthening of photovoltaic and supercapacitive properties of graphene oxide-polyaniline composite by dispersion of α -Al₂O₃ nanoparticles

Kailash Nemade^{a,*}, Pradip Tekade^b, Priyanka Dudhe^b^a Department of Physics, Indira Mahavidyalaya, Kalamb 445 401, India^b Department of Chemistry, Jankidevi Bajaj College of Science, Wardha 442 001, India

ARTICLE INFO

Article history:

Received 3 May 2018

In final form 8 July 2018

Available online 10 July 2018

Keywords:

Graphene oxide

Polyaniline

Photovoltaic

Supercapacitive properties

ABSTRACT

It is demonstrated that the dispersion of α -Al₂O₃ nanoparticles in graphene oxide (GO)-polyaniline (PANi) composite results in significant enhancement of photovoltaic and supercapacitive properties. In order to improve PV and SC properties of GO-PANi composite, 0.5 wt% of α -Al₂O₃ nanoparticles were added in composite. Both PV and SC properties of composites becomes strengthen by addition of 0.5 wt% of α -Al₂O₃ nanoparticles. The GO-PANi/ α -Al₂O₃ composite shows power conversion efficiency (η) 9.31%, which is significantly higher than pure α -Al₂O₃ nanoparticles and GO-PANi composite. The GO-PANi/ α -Al₂O₃ composite achieve considerable specific capacitance of the order 715.5 Fg⁻¹ at scan rate of 2 mV s⁻¹.

© 2018 Elsevier B.V. All rights reserved.

1. Introduction

The widespread use of inorganic photovoltaic cell is still limited because of complications in modification of band gap of inorganic materials and high processing costs [1]. Different approaches using organic or polymer materials such as conducting polymer, graphene and metal oxides have received considerable attention because of their low cost, light weight and flexibility [2]. Whereas supercapacitor is a new class of device, which comes under the category of energy storage devices, and fulfill the technological gap between conventional capacitor and battery. Supercapacitor has some outstanding features like power density, rapid store/release of energy, good charge/discharge life cycles, and Eco friendliness. For supercapacitor application, carbon nanomaterials such as carbon nanotubes and graphene are extensively used, due to their high specific surface area and good electrical conductivity [3].

The use of carbon nanostructures with the conducting polymer is also investigated as supercapacitive material extensively. Yu et al investigated the polyaniline/graphene composite as electrode material for supercapacitors. The electrochemical capacitance of composite has value 596.2 Fg⁻¹ and after 1500 cycles at a current density of 2 Ag⁻¹, only 16.3% drop in the initial capacitance is observed [4]. Wang et al synthesized PANi with different mor-

phologies and combined with graphene to use as electrode materials of supercapacitors. The result of the study shows that sheet-like Graphene/PANi composites can deliver specific capacitances of 532.3–304.9 Fg⁻¹ at scan rates of 2–50 mV/s [5]. Wu et al prepared the Polyaniline/graphene hydrogel composites for supercapacitor application with macroscopically phase-separated structure, which exhibits the high specific capacitance and excellent rate performance. This work concludes the PANi is mainly outside the graphene hydrogel matrix, can enhance the rate performance of the composites [6]. Cong et al prepared the graphene-PANi paper and employed for the supercapacitor application. The composite paper has considerable specific capacitance (763 Fg⁻¹) and good cycling stability [7]. Moussa et al reviewed comprehensively the recent developments in polyaniline/graphene nanocomposites as supercapacitor electrodes. This work underlined the polyaniline/graphene nanocomposites have great potential in electrochemical energy storage applications, especially supercapacitors [8]. Theophile et al reported the successful preparation of Poly(vinyl alcohol)-graphene oxide and Poly(vinyl alcohol)-reduced graphene oxide composite for supercapacitor application. The results of the study indicates that Poly(vinyl alcohol)-reduced graphene oxide composite (190 Fg⁻¹) deliver good supercapacitive properties than Poly(vinyl alcohol)-graphene oxide (13 Fg⁻¹) composite [9]. Loeblein et al a novel material having oxidized-three-dimensional-graphene, with a band gap of 0.2 eV. This material found suitable for electrode application in dye-sensitized solar cells where electrode has stringent work-function requirements [10]. Li et al successfully

* Corresponding author.

E-mail address: knemade@gmail.com (K. Nemade).

fabricated the PANi nanotubes-based supercapacitors having maximum areal capacitance of 237.5 mF cm^{-2} (scan rate = 10 mVs^{-1}) with maximum energy density of $24.31 \text{ mW h cm}^{-2}$ (power density = 2.74 mW cm^{-2}). Under bending condition, supercapacitor shows excellent performance. After 2000 cycles, the capacitor maintains 95.2% of the initial capacitive value [11].

Feng et al prepared the graphene/polyaniline nanocomposites by using one-step hydrothermal method. The graphene/PANi nanowire composites exhibit the excellent electrochemical properties having specific capacitance 724.6 F/g higher than the graphene/PANi nanocomposite (602.5 F/g). This study demonstrated that morphology of materials also plays key role in optimization of electrochemical properties [12]. Zhou et al reported the effect of morphology on electrochemical properties using materials system nanoflake-like and nanobelt-like $\alpha\text{-MoO}_3$ /graphene nanocomposites. The results of the investigation demonstrated that $\alpha\text{-MoO}_3$ nanoflakes/graphene exhibited better supercapacitive (up to 360 Fg^{-1}) performances than $\alpha\text{-MoO}_3$ nanobelts/graphene [13].

In the light of above discussion, we planned to investigate the photovoltaic and primary electrochemical properties of $\alpha\text{-Al}_2\text{O}_3$ /PANi-GO composite. In this work, we studied the PV cell properties such as fill factor and power conversion efficiency and supercapacitive properties such, cyclic voltammetry (CV) curve, areal capacitance and cycle stability performance of composite materials. The main accomplishment of present work is that we achieved considerable value of power conversion efficiency and specific capacitance for $\alpha\text{-Al}_2\text{O}_3$ /PANi-GO composite.

2. Experimental

2.1. Materials preparation and characterization

In the present study, all AR-grade (SD Fine, India) chemicals were used for the preparation materials without further purification. The chemical oxidative polymerization was adopted for the

preparation of Polyaniline (PANi). The method of preparation of PANi is reported previously [14]. In this process, aniline monomer and ammonium persulphate were used with molar ratio 1:1 M for preparation of PANi in aqueous media. The addition of aniline monomer in oxidant under constant magnetic stirring results in dark greenish precipitated. As obtained precipitated was washed two times with distilled water and dried in oven for overnight. The fine powder of PANi was used for the preparation of composites. The graphene oxide (GO) used in this work was prepared by previously reported method [15]. The ex-situ approach was adopted for the preparation of composites. The GO loaded PANi composite was prepared by taking equal wt.% of both contents. Whereas, $\alpha\text{-Al}_2\text{O}_3$ loaded-GO/PANi composite was prepared by taking 0.5 wt% concentration of $\alpha\text{-Al}_2\text{O}_3$ nanoparticles. Both the composites prepared in organic media (Acetone).

The X-ray diffraction (XRD) patterns of as-prepared materials were recorded on Rigaku Miniflex-II using $\text{CuK}\alpha$ radiation ($\lambda = 1.54 \text{ \AA}$). The morphology of samples was investigated using scanning electron microscope (SEM) images obtained from JEOL JSM-7500F.

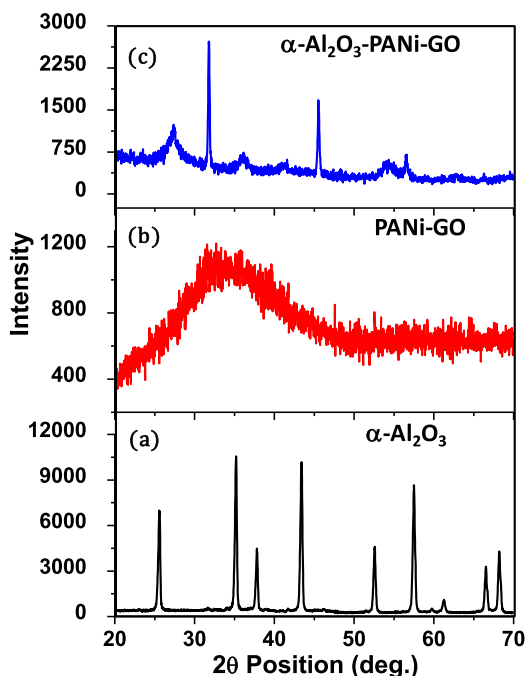


Fig. 1. XRD pattern of $\alpha\text{-Al}_2\text{O}_3$ nanoparticle, PANi-GO and $\alpha\text{-Al}_2\text{O}_3$ /PANi-GO composite.



Fig. 2. FE-SEM images of $\alpha\text{-Al}_2\text{O}_3$, PANi-GO and $\alpha\text{-Al}_2\text{O}_3$ /PANi-GO composite.

2.2. Supercapacitive study

Electrochemical measurements such as cyclic voltammetry (CV), areal capacitance and capacitance retention analysis were carried out using three-electrode cell systems (CHI 660 D, CH Instruments). As-prepared materials were used as the working electrode, platinum wire as counter electrode and Ag/AgCl as the reference electrode.

2.3. Photovoltaic (PV) study

PV cell required for testing was prepared by doctor blade technique. During the fabrication of PV cell, indium tin oxide (ITO) coated glass plate were used as transparent electrode and aluminum as metallic electrode. The photovoltaic properties of as-fabricated PV cell such as fill factor (FF) and power conversion efficiency ($\% \eta$) confirmed by measuring short circuit current (I_{sc}), open circuit voltage (V_{oc}) and I_{max} and V_{max} from IV characteristics of PV cells.

3. Results and discussion

3.1. Characterization of materials

Fig. 1(a) shows the XRD pattern of α -Al₂O₃ nanoparticles, which is in good agreement with PDF Card No-01-081-1667. No other peaks for impurities were detected in pattern. The average crystallite size was computed by considering all prominent diffraction peaks using the Debye-Scherrer equation, which found to be 37.3 nm [16]. Fig. 1(b) depicts the XRD pattern of PANi-GO composite. The XRD pattern shows noisy behavior of diffraction peaks, which confirms the composite exhibited amorphous nature. In addition to this composite comprises broad

hump between 2θ -range 20–30°. Fig. 1(c) shows the XRD pattern of α -Al₂O₃ nanoparticles loaded PANi-GO composite. Pattern clearly indicates the presence of signature peaks of α -Al₂O₃ and GO. This indicates the nice incorporation of α -Al₂O₃ in PANi-GO composite.

Fig. 2 represents the SEM images of α -Al₂O₃, PANi-GO and α -Al₂O₃/PANi-GO composite. SEM image of α -Al₂O₃ shows the nanoparticles have irregular shape with well separated boundaries. The average crystallite size estimated using XRD analysis is in good agreement with SEM study. The SEM images of PANi-GO and α -Al₂O₃/PANi-GO composite have almost identical morphology like petals or sheets structure.

3.2. PV study of materials

Fig. 3(a–c) shows IV characteristics of PV cell fabricated using the active PV material, α -Al₂O₃, PANi-GO and α -Al₂O₃/PANi-GO composite respectively and the PV parameters reflected by materials are listed in Table 1. From results, it is concluded that α -Al₂O₃ loaded PANi-GO composite achieve higher short circuit current (I_{sc}) than pure α -Al₂O₃ and PANi-GO. This might be attributed to the good dispersion of α -Al₂O₃ in PANi-GO composite and good charge-transfer process within composite, which is evident in the higher value of I_{sc} [17]. There is a significant enhancement in

Table 1
PV parameters of α -Al₂O₃, PANi-GO and α -Al₂O₃/PANi-GO composite.

Material	I_{max} (mA)	V_{max} (V)	I_{sc} (mA)	V_{oc} (V)	FF	$\% \eta$
α -Al ₂ O ₃	23.8	0.2	23.8	0.7	0.285	1.61
PANi-GO	86	0.2	86	0.7	0.285	5.81
α -Al ₂ O ₃ /PANi-GO	137.7	0.2	137.7	0.8	0.25	9.31

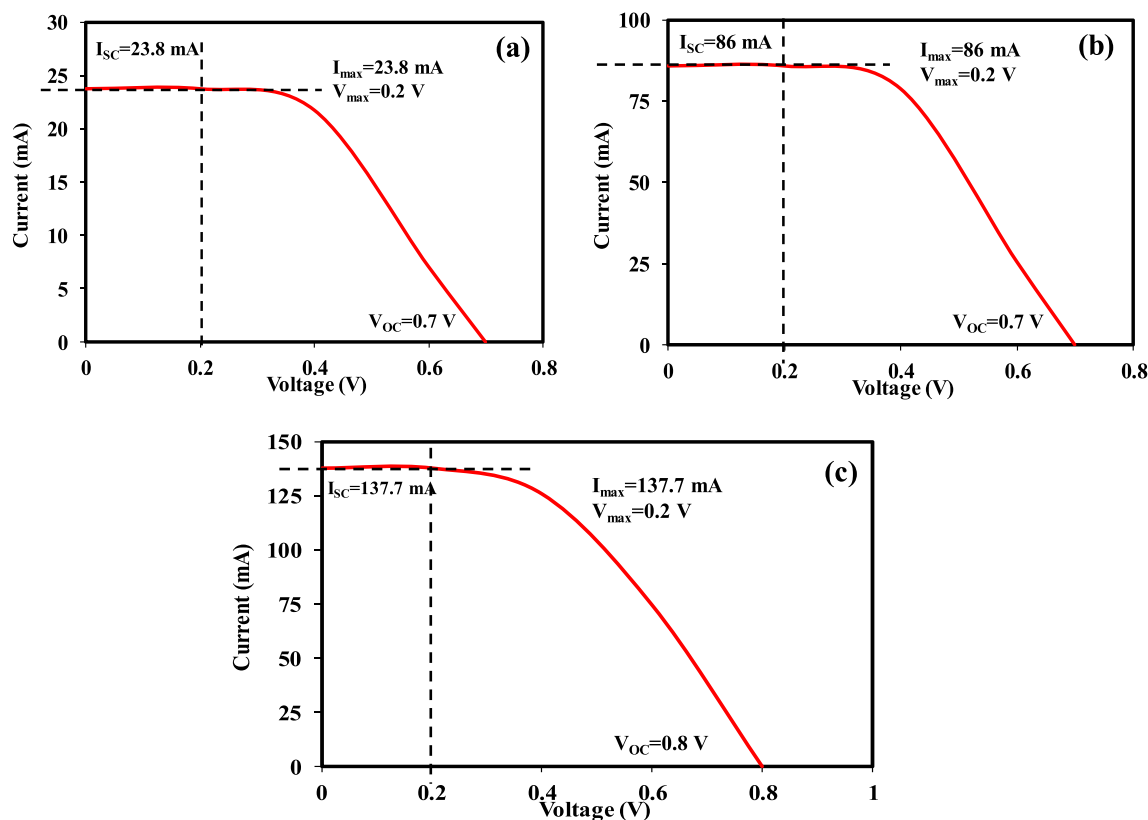


Fig. 3. PV response of (a) α -Al₂O₃, (b) PANi-GO (c) α -Al₂O₃/PANi-GO composite.

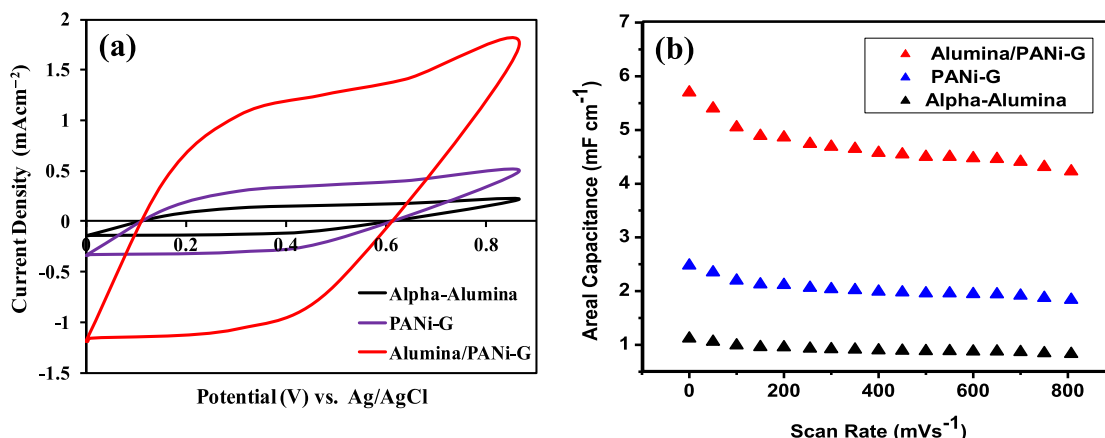


Fig. 4. (a) CV curves and (b) Areal capacitance as a function of scan rate of the α -Al₂O₃, PANi-GO and α -Al₂O₃/PANi-GO recorded at a scan rate of 2 mV s⁻¹.

% η resulted due to the addition of α -Al₂O₃ in PANi-GO composite. The highest value of % η is 9.31% for α -Al₂O₃/PANi-GO composite, whereas % η is 5.81% for PANi-GO composite and 1.61% for α -Al₂O₃.

3.3. Supercapacitive study of materials

Fig. 3a shows the cyclic voltammetric (CV) curves of α -Al₂O₃, PANi-GO and α -Al₂O₃/PANi-GO recorded at a scan rate of 2 mV s⁻¹. The CV curves clearly shows the α -Al₂O₃/PANi-GO composite have superior supercapacitive properties over pristine α -Al₂O₃, PANi-GO composite. The superior supercapacitive properties of

α -Al₂O₃/PANi-GO composite can be attributed to oxidation/reduction of surface hydroxyl groups [18]. Specific capacitance has been estimated using the relation (Eq. (1)) [19],

$$C_s = \frac{I}{m \times \nu} (\text{Fg}^{-1}) \quad (1)$$

where I is the average current during anodic and cathodic scan (A), m is the mass of the electrode (g) and ν is the scan rate (V). In our case, the highest value of specific capacitance was found to be 715.5 Fg⁻¹ at a scan rate of 2 mV s⁻¹ for α -Al₂O₃/PANi-GO composite.

Fig. 3b shows the variation of calculated areal capacitance of the α -Al₂O₃, PANi-GO and α -Al₂O₃/PANi-GO composite as a function of scan rate. Here also plot clearly depicts that α -Al₂O₃/PANi-GO composite has several fold higher capacitance over the pristine α -Al₂O₃, PANi-GO composite. The significant enhancement in electrochemical performance was attributed to two main processes occurring in the composite. First is that composite possesses improved carrier density, which results in good electrical conductivity. Second is the increase of density of hydroxyl groups on α -Al₂O₃/PANi-GO composite [20]. The absence of redox peak indicates that capacitance was mainly contributed by non-faradaic redox reactions.

As shown in Fig. 4, the capacitance drops in pristine α -Al₂O₃ and PANi-GO composite is significantly more than α -Al₂O₃/PANi-GO composite. The α -Al₂O₃/PANi-GO composite electrode exhibits an excellent long-term stability with 95.83% capacitance retention after 7000 cycles. The good capacitance ability of α -Al₂O₃/PANi-GO composite is ascribed to enhanced electrical conductivity and highly stable surface redox reaction [21] (see Fig. 5).

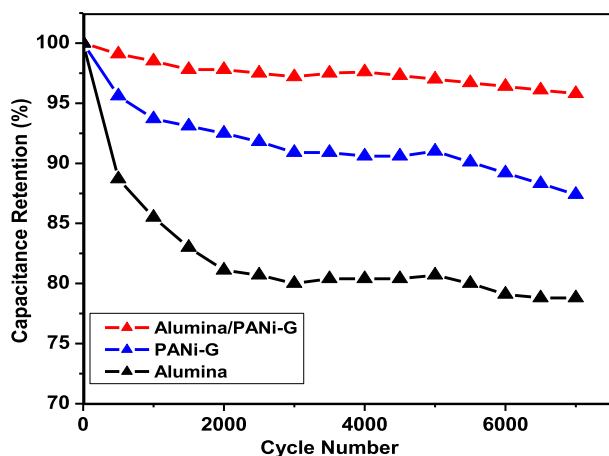


Fig. 5. Cycle performance of the α -Al₂O₃, PANi-GO and α -Al₂O₃/PANi-GO composite measured at a scan rate of 2 mV s⁻¹ for 7000 cycles.

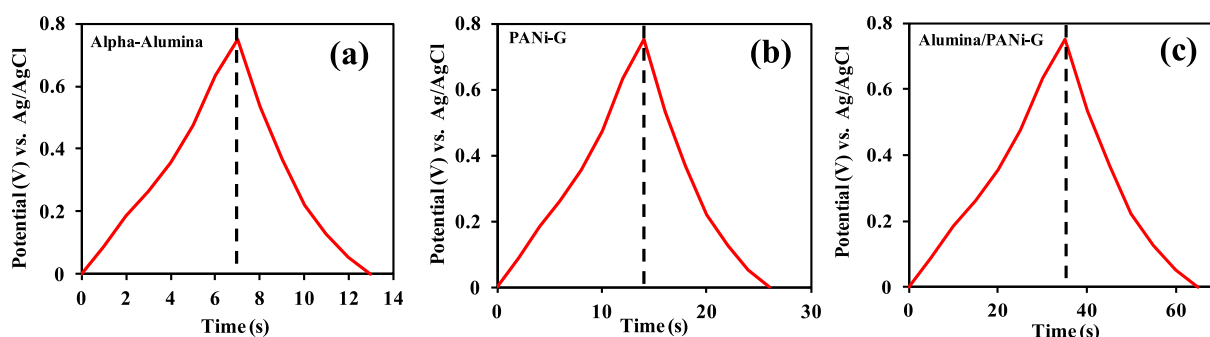


Fig. 6. Galvanostatic charge/discharge curves of the (a) α -Al₂O₃, (b) PANi-GO and (c) Al₂O₃/PANi-GO collected at a current density of 10 μ Acm⁻².

Electrochemical study of α - Al_2O_3 , PANi-GO and Al_2O_3 /PANi-GO samples were extended by measuring charge/discharge measurements. Fig. 6(a–c) shows the galvanostatic charge/discharge (GCD) curves of α - Al_2O_3 , PANi-GO and Al_2O_3 /PANi-GO samples, respectively. The GCD curves of Al_2O_3 /PANi-GO sample is nearly symmetric and significantly lengthy than α - Al_2O_3 and PANi-GO. This indicates capacitive properties of Al_2O_3 /PANi-GO sample superior than α - Al_2O_3 and PANi-GO. Improved performance of Al_2O_3 /PANi-GO attributed to synergetic state between α - Al_2O_3 and PANi-GO.

4. Conclusions

In summary, we have successfully demonstrated that the photovoltaic and supercapacitive performance of GO-PANi/ α - Al_2O_3 composite is superior over the α - Al_2O_3 and PANi-GO composite. GO-PANi/ α - Al_2O_3 composite based PV cell shows significant power conversion efficiency of the order of 9.31%, which much higher than α - Al_2O_3 and PANi-GO composite. The GO-PANi/ α - Al_2O_3 composite exhibits the considerable specific capacitance of the order 715.5 Fg^{-1} . The GO-PANi/ α - Al_2O_3 composite retain 95.83% capacitance after 7000 cycles, which shows the good cycling stability of composites. The GCD characteristics of Al_2O_3 /PANi-GO sample improved due to synergetic effect between α - Al_2O_3 and PANi-GO composite. At present work is underway for the optimization of the electrochemical performance GO-PANi/ α - Al_2O_3 composite.

Acknowledgment

The authors appreciate the help of Dr. S.K. Omanwar Head, Department of Physics, Sant Gadge Baba Amravati University, Amravati for providing necessary facilities for the work.

References

- [1] R.M. Swanson, *Progress in Photovoltaic: Res. Appl. (Special Issue)* 14 (2006) 443–453.
- [2] N.S. Sariciftci, S.S. Sun, *Organic Photovoltaics: Mechanism, Materials, and Devices*, Taylor & Francis, New York, 2005.
- [3] M.F. El-Kady, V. Strong, S. Dubin, R.B. Kaner, Laser scribing of high-performance and flexible graphene-based electrochemical capacitors, *Science* 335 (2012) 1326–1330.
- [4] T. Yu, P. Zhu, Y. Xiong, H. Chen, S. Kang, H. Luo, S. Guan, Synthesis of microspherical polyaniline/graphene composites and their application in supercapacitors, *Electrochim. Acta* 222 (2016) 12–19.
- [5] R. Wang, M. Han, Q. Zhao, Z. Ren, X. Guo, C. Xu, N. Hu, L. Lu, Hydrothermal synthesis of nanostructured graphene/polyaniline composites as high-capacitance electrode materials for supercapacitors, *Scientific Reports* 7 (2017), Article number: 44562.
- [6] J. Wu, Q. Zhang, A. Zhou, Z. Huang, H. Bai, L. Li, Phase-separated polyaniline/graphene composite electrodes for high-rate electrochemical supercapacitors, *Adv. Mater.* 28 (2016) 10211–10216.
- [7] H. Cong, X. Ren, P. Wang, S. Yu, Flexible graphene–polyaniline composite paper for high-performance supercapacitor, *Energy Environ. Sci.* 6 (2013) 1185–1191.
- [8] M. Moussa, M. El-Kady, Z. Zhao, P. Majewski, J. Ma, Recent progress and performance evaluation for polyaniline/graphene nanocomposites as supercapacitor electrodes, *Nanotechnology* 27 (2016) 395201.
- [9] N. Theophile, H.K. Jeong, Electrochemical properties of poly(vinyl alcohol) and graphene oxide composite for supercapacitor applications, *Chem. Phys. Lett.* 669 (2017) 125–129.
- [10] M. Loeblein, A. Bruno, G.C. Loh, A. Bolkere, C. Saguy, L. Antila, S.H. Tsang, E.H.T. Teo, Investigation of electronic band structure and charge transfer mechanism of oxidized three-dimensional graphene as metal-free anodes material for dye sensitized solar cell application, *Chem. Phys. Lett.* 685 (2017) 442–450.
- [11] H. Li, J. Song, L. Wang, X. Feng, R. Liu, W. Zeng, Z. Huang, Y. Ma, L. Wang, Flexible all-solid-state supercapacitors based on polyaniline orderly nanotubes array, *Nanoscale* 9 (2017) 193–200.
- [12] X. Feng, N. Chen, J. Zhou, Y. Li, Z. Huang, L. Zhang, Y. Ma, L. Wang, X. Yan, Facile synthesis of shape-controlled graphene–polyaniline composites for high performance supercapacitor electrode materials, *New J. Chem.* 39 (2015) 2261–2268.
- [13] J. Zhou, J. Song, H. Li, X. Feng, Z. Huang, S. Chen, Y. Ma, L. Wang, X. Yan, The synthesis of shape-controlled α - MoO_3 /graphene nanocomposites for high performance supercapacitors, *New J. Chem.* 39 (2015) 8780–8786.
- [14] K.R. Nemade, Chemically synthesized Sn doped polyaniline hydrochloride for carbon dioxide gas sensing, *Sensors Transducers* 135 (2011) 110–117.
- [15] K.R. Nemade, S.A. Waghuley, Chemiresistive gas sensing by few-layered graphene, *J. Electron. Mater.* 42 (2013) 2857–2866.
- [16] K.R. Nemade, S.A. Waghuley, Preparation of MnO₂ immobilized graphene nanocomposite by solid state diffusion route for LPG sensing, *J. Lumin.* 153 (2014) 194–197.
- [17] B. He, Q. Tang, M. Wang, H. Chen, S. Yuan, Robust polyaniline-graphene complex counter electrodes for efficient dye-sensitized solar cells, *ACS Appl. Mater. Interfaces* 6 (2014) 8230–8236.
- [18] D. Choi, G.E. Blomgren, P.N. Kumta, Fast and reversible surface redox reaction in nanocrystalline vanadium nitride supercapacitors, *Adv. Mater.* 18 (2006) 1178–1182.
- [19] B. Sethuraman, K.K. Purushothaman, G. Muralidharan, Synthesis of mesh-like $\text{Fe}_2\text{O}_3/\text{C}$ nanocomposite via greener route for high performance supercapacitors, *RSC Adv.* 4 (2014) 4631–4636.
- [20] X. Lu, G. Wang, T. Zhai, M. Yu, J. Gan, Y. Tong, Y. Li, Hydrogenated TiO_2 nanotube arrays for supercapacitors, *Nano Lett.* 12 (2012) 1690–1696.
- [21] M. Kaempgen, C.K. Chan, J. Ma, Y. Cui, G. Gruner, Printable thin film supercapacitors using single-walled carbon nanotubes, *Nano Lett.* 9 (2009) 1872–1876.

In Vitro Study of Interactions of Carboxamide Derivatives of Amino Acid with BSA: Ultrasonic Interferometer

Shrikant Bandupant Thakare, Pradip Vitthalrao Tekade*, Ajay Madhukarrao Pisuddes

Department of Chemistry, Jankidevi Bajaj College of Science, Jamnalal Bajaj Marg, Civil lines, Wardha-442001-M.S. India.

Article history: Received: 14 January 2018; revised: 02 June 2018; accepted: 06 June 2018. Available online: 30 June 2018. DOI: <http://dx.doi.org/10.17807/orbital.v10i5.1161>

Abstract:

In this paper we account the interaction of the Carboxamide derivatives of amino acid viz 2-[[2-(cyclohexycarbamoyl) benzoyl] amino] propanoic acid (**2CMPA**), 2-Benzamido acetic acid 2-cyclohexyl carboxamide (**2BA2C**), 2-[[2-(cyclohexylcarbamoyl) benzoyl] amino]-3-methylbutanoic acid (**2CA3MBA**), 2-benzamido-4-methylpentanoic acid-2-cyclohexyl carboxamide (**2-BMCA**) and 2-[[2-(cyclohexycarbamoyl) benzoyl] amino]-4-(methylsulfanyl) butanoic acid (**2CA4MBA**) with protein Bovine serum albumin (BSA) using ultrasonic interferometer technique. Ultrasonic velocity for complex solution of different compounds of carboxamide derivatives of amino acid with BSA has been measured at their different composition using ultrasonic interferometer. Difference in the ultrasonic velocity at different compositions of complex is measure of binding of the compounds with BSA. Binding effect at various pH viz. 3, 4 and 5 shows that compounds bound to the BSA more significantly at acidic pH and association constant decreases with increase in pH value. Scatchard analysis gives the values of association constants (K_f) for all the compounds at pH 3, 4 and 5 respectively.

Keywords: ultrasonic interferometer; bovine serum albumin; carboxamide; association constant; scatchard analysis

1. Introduction

Binding of drug to plasma protein is one of the efficient biological characteristics of that drug. There are various proteins which show affinity for the drugs depending on their nature. There are various plasma protein such as Human serum albumin (HSA) and Bovine serum albumin Alpha acid glycoprotein (AGP) and Lipoprotein etc which shows affinity towards the drugs. These proteins perform various functions out of that drug binding and their transportation is an important one.

BSA is the moiety with large molecular weight ($M_r = 66,500$) contains 583 amino acids. As BSA is a major protein in blood, any change in level of BSA produces effect on transportation of drug. BSA is alkaline having 7-8 pH range [1] hence it shows the affinity for acidic drugs. There are various forces which are responsible for binding

of drug to plasma protein viz. hydrogen bonding, vander wall forces, electrostatic attraction etc.

Binding study of various drugs with plasma proteins has been done such as the effect of binding on specific site of BSA for ciprofloxacin and captopril drugs in presence of specific site probe studied using equilibrium dialysis [2]. The protein-protein and protein-ligand interactions involved in retinol transport studied in plasma [3]. Interaction of drugs like i-bruprofen & naproxen shows successive binding to protein [4]. Effect of arsenic on binding of protein with warfarin and acetaminophen observed [5]. Crystal structure analysis of binding of warfarin to BSA also studied [6]. NMR Spectroscopic approach reveals metabolic diversity of human blood plasma associated with protein drug interaction [7].

Effect of arsenic on binding of paracetamol

*Corresponding author. E-mail: pradiptekade@gmail.com

with BSA was studied using equilibrium dialysis method [8]. Thin layer chromatography technique used for the study of protein binding interaction of daspone and pyrimethamine [9]. Structure based approach for discovering protein–ligand binding affinity and drug designing from serum albumin model systems studied using NMR technique [10]. Affinity and specificity of ciprofloxacin-BSA interaction determined by fluorescence spectrophotometry [11]. Mass spectrometry based tools used to investigate protein-ligand interactions for drug discovery [12]. Interaction of propranolol with glycoprotein deliberated using micro liquid-liquid interface [13]. Comparative study of various techniques for drug-protein binding gives informative knowledge [14]. Study of interaction of the bioactive component Jatrorrhizine to HSA shows significant change in secondary structure of HSA [15]. Interactions of HSA with chlorogenic acid and ferulic acid observed [16]. Study of binding of atrazine and 2, 4-D with HSA show partial unfolding [17]. Effect of binding of mitoxantrone with HSA was

successfully observed using FT-IR spectroscopy [18]. Quercetin and amantadine successfully binds with egg albumin which form new complex [19].

In this paper we report the simple and useful ultrasonic interferometer technique for the study of interaction of carboxamide derivatives of amino acid with BSA. The compounds synthesized are biologically active and shows pharmaceutically importance due to its antibacterial activity [20]. The binding affinity of these compounds with BSA measured using ultrasonic interferometer and effect of pH on binding affinity also measured by acoustical properties.

2. Results and Discussion

The carboxamide derivatives of amino acids were synthesized using known method [20] and characterized by spectral techniques viz. IR, NMR and Mass spectrometry (**Fig. 1**).

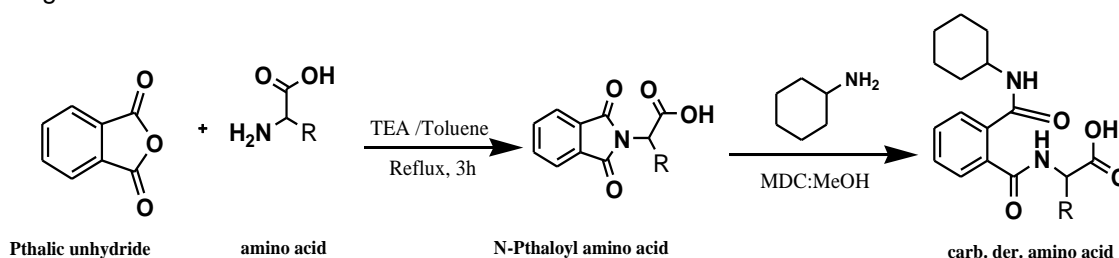


Figure 1. Scheme for synthesis of carboxamide derivatives of amino acids. Where, R= H, -CH₃, -CH-(CH₃)₂, -CH₂-CH-(CH₃)₂, -CH₂-CH₂-S-CH₃. 2-Benzamido-4-methylpentanoic acid-2-cyclohexyl carboxamide (**2-BMCA**), 2-[[2-(cyclohexylcarbonyl) benzoyl] amino]-4-(methylsulfanyl) butanoic acid (**2CA4MBA**), 2-[[2-(cyclohexylcarbonyl) benzoyl] amino]-3-methylbutanoic acid(**2CA3MBA**), 2-[[2-(cyclohexylcarbonyl) benzoyl] amino] propanoic acid(**2CMPA**), and 2-Benzamido acetic acid 2-cyclohexyl carboxamide (**2BA2C**).

Experimental observations

50 μ M solution of BSA and 0.01M solution of compounds are prepared using acetate buffer solution of pH 3, 4 and 5. Complex solution of BSA and compounds were taken in a cell of 1MHz frequency of ultrasonic interferometer at various compositions viz. 9:1, 8:2, 7:3, 6:4, 5:5, 4:6 and ultrasonic velocity recorded for them. The values of ultrasonic velocities complex solutions of compounds 2CA3MBA, 2CA4MBA, 2BMCA, 2BA2C, 2CMPA with BSA are recorded at pH 3, 4 and 5 which are shown in **Table 1**, **2** and **3**, respectively.

Measurement of ultrasonic velocity at varying composition of BSA and compounds at pH 3, 4 and 5 gives the value of association constant (K_i) which is calculated from Scatchard graph. The value of association constant (K_i) for complex solutions of the compounds at pH 3, 4 and 5 are: **2CA3MBA** 0.5035, 0.5023 and 0.5021, for **2CA4MBA** 0.5052, 0.5038 and 0.5032, for **2BMCA** 0.5036, 0.5024 and 0.5023 for **2BA2C** 0.5042, 0.5024 and 0.5022 and for **2CMPA** 0.5041, 0.5023 and 0.5017, respectively. **Fig. 2** shows graph of ultrasonic velocity vs Percent ligand fraction and specific binding vs percent ligand fraction for all the compounds at pH 3. **Fig.**

3 and Fig. 4 shows graph of ultrasonic velocity vs Percent ligand fraction and graph of Specific binding vs Percent ligand fraction for all the compounds at pH 4 and 5.

Table 1. Ultrasonic velocities for compounds at pH 3.

Composition of BSA-Compounds	Ultrasonic velocity at pH 3				
	2CA3MBA	2CA4MBA	2BMCA	2BA2C	2CMPA
10:0	1484.700	1484.687	1485.870	1485.270	1485.270
9:1	1512.260	1510.860	1506.260	1508.529	1507.870
8:2	1519.870	1511.370	1509.870	1509.189	1508.529
7:3	1520.260	1516.260	1510.260	1509.580	1509.580
6:4	1518.920	1518.920	1508.920	1510.512	1509.850
5:5	1519.870	1519.670	1510.870	1509.870	1510.570
4:6	1520.870	1519.870	1510.870	1510.512	1508.529

Table 2. Ultrasonic velocities for compounds at pH 4.

Composition of BSA-Compounds	Ultrasonic velocity at pH 4				
	2CA3MBA	2CA4MBA	2BMCA	2BA2C	2CMPA
10:0	1492.860	1494.260	1494.260	1495.877	1495.877
9:1	1514.870	1509.270	1504.870	1508.280	1508.529
8:2	1518.928	1513.728	1508.928	1509.870	1509.129
7:3	1521.260	1513.260	1511.260	1511.211	1509.850
6:4	1522.860	1514.727	1511.860	1512.529	1510.512
5:5	1519.870	1515.540	1509.870	1510.870	1510.850
4:6	1518.684	1515.884	1510.684	1511.684	1510.512

Table 3. Ultrasonic velocities for compounds at pH 5.

Composition of BSA-Compounds	Ultrasonic velocity at pH 5				
	2CA3MBA	2CA4MBA	2BMCA	2BA2C	2CMPA
10:0	1495.207	1495.707	1498.327	1497.247	1497.280
9:1	1519.260	1511.260	1509.260	1509.260	1506.529
8:2	1522.870	1512.189	1513.870	1513.163	1507.824
7:3	1522.698	1512.698	1512.698	1513.827	1508.590
6:4	1524.260	1514.512	1514.260	1513.499	1509.120
5:5	1525.870	1516.260	1514.860	1513.836	1509.590
4:6	1525.260	1515.860	1513.870	1513.512	1509.870

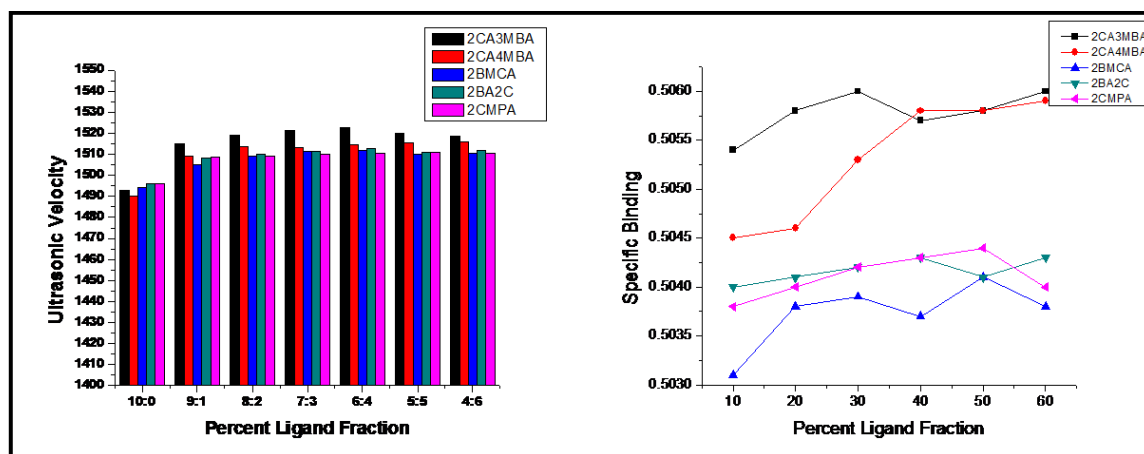


Figure 2. Graph of Ultrasonic velocity and Specific binding Vs Percent ligand fraction at pH 3 for carboxamide derivatives of amino acid.

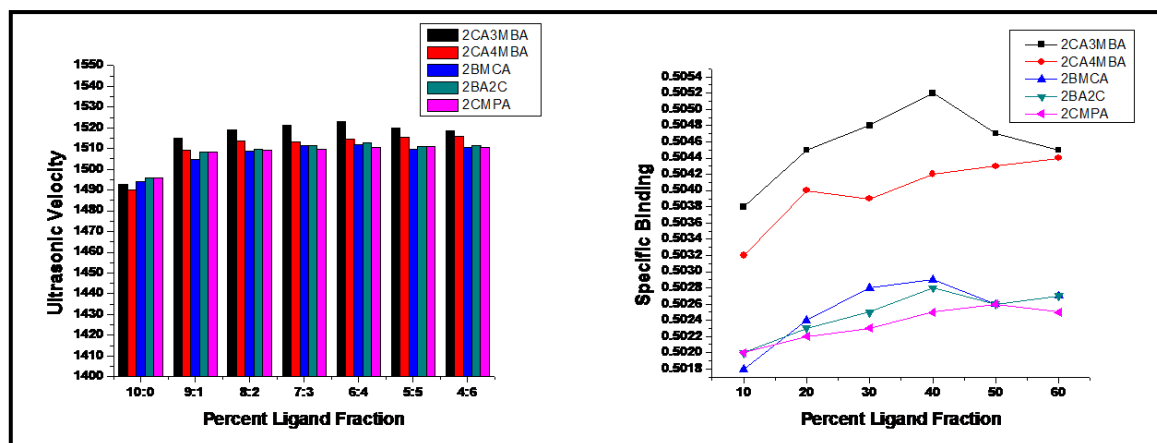


Figure 3. Graph of Ultrasonic velocity and Specific binding Vs Percent ligand fraction at pH 4 for carboxamide derivatives of amino acid.

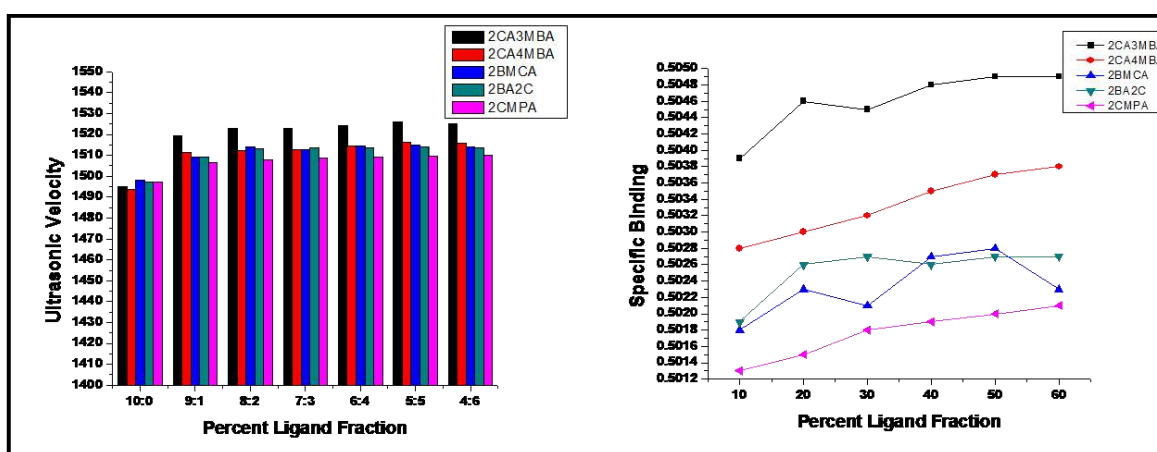


Figure 4. Graph of Ultrasonic velocity and Specific binding Vs Percent ligand fraction at pH 5 for carboxamide derivatives of amino acid.

3. Material and Methods

Synthesis

For the synthesis of the compounds all the chemicals used were of A.R. grade of Merck India Limited make and purchased from commercial suppliers. The purity of the synthesized compound was as certain by thin layer chromatography on silica gel G in petroleum ether and ethyl acetate (7:3) mixture, melting point was recorded using digital melting point apparatus Equiptronics (EQ 730). ^1H NMR spectra of the compound were recorded in CDCl_3 on NMR instrument (500MHz) using TMS as an internal standard from SAIF, CDRI Lucknow.

For measurement of binding, digital ultrasonic echo pulse velocity meter (Vi Microsystem Ltd. India), BSA ($M_r = 66,500$) (Chemsworth chemical Ltd. India), 0.1M sodium acetate buffer solution of 3, 4 and 5 (± 0.05) pH was used.

Measurement of binding affinity

Ultrasonic interferometer was set up at 1MHz frequency range and appropriate cell of the frequency used. BSA solution of $50\mu\text{M}$ concentration in aqueous phase using acetate buffer of pH range 3,4 and 5 prepared and ultrasonic velocity of these solutions were calculated in lack of compounds. Secondly the solution of compounds of 0.01M concentration prepared using buffer solution of varying pH 3, 4 and 5. Mixture of solution of BSA and compounds at pH 3 in different composition viz. 9:1, 8:2, 7:3, 6:4, 5:5, 4:6 prepared and used to measure ultrasonic velocities. Similarly, ultrasonic velocities for same composition of BSA and compound at 4 and 5 pH were also recorded. *Scatchards plot* used for measurement of specific binding of compounds with BSA at different composition and from which the value of association constant are calculated.

4. Conclusions

Carboxamide derivatives of amino acids shows antibacterial activity hence they considered as pharmaceutically active compounds. For drug showing pharmaceutical activity, it is a significant aspect to see their affinity towards plasma protein. The interaction of these amino acid derivatives observed with bovine serum albumin (BSA) under the condition of varying pH and temperature using the ultrasonic interferometer technique. After interaction between BSA-carboxamide derivatives of amino acid, different association constant values at different pH obtained. It is observed that the value of the association constant decreases with an increase in the pH value for all the compounds 2CMPA, 2BA2C, 2CA3MBA, 2-BMCA and 2CA4MBA at pH 3, 4, and 5 respectively. It means the order of the association constant for all the compounds at pH 3, 4, and 5 is $3 > 4 > 5$.

But the order of the association constant varies for compounds at varying pH values is slightly different. At pH 3 the sequential order of the association constant for compounds is $2CA4MBA > 2BA2C > 2CMPA > 2BMCA > 2CA3MBA$.

At pH 4 the order of the association constant for compounds is $2CA4MBA > 2BA2C > 2BMCA > 2CMPA > 2CA3MBA$.

At pH 5 the sequence order of the association constant for compounds is $2CA4MBA > 2BMCA > 2BA2C > 2CA3MBA > 2CMPA$.

So, there is slight variation observed for compounds while considering the effect of each pH separately on each drug. At all the pH the value of the association constant is highest for compound 2CA4MBA which is may be due to long alkyl chain having sulphur atom sandwiched in it, sulphur increases the activity of compound

References and Notes

- [1] Putnam, F. W. *New York: Academic Press*, 1975, 141.
- [2] Mahbulal, A.; Reza, N. *Biol. Sci.* **2004**, 7, 79.
- [3] Raz, A.; Shiratori, T.; Goodman, D. S. *Biol. Chem.* **1970**, 245, 1903.
- [4] Rahman, M. *Pharm. Sci.* **2005**, 18, 43.
- [5] Alam, A.; Riaz, U. *J. Pharmacol.* **2008**, 3, 49.
- [6] Petitpas, I.; et.al. *Biol. Chem.* **2001**, 276, 22804. [\[Crossref\]](#)
- [7] Yuangyuan.; et.al. *Anal. Chem.* **2013**, 85, 8601.
- [8] Riaz, U.; Nadia, S.; et.al. *Int. Curr. Pharm. J.* **2012**, 1, 361.
- [9] Ahmad, R. A.; Roggers, H. J. *BCJP* **1980**, 10, 519.
- [10] Fielding, L.; Rutherford, S.; Fletcher, D. *Magnetic Res. Chem.* **2012**, 43, 463. [\[Crossref\]](#)
- [11] Yan H. J.; Zhang, Y.; Liu Y. *The Protein Journal* **2010**, 29, 234. [\[Crossref\]](#)
- [12] Pacholarz, K.; Garlish R.A.; et.al. *Chem. Soc. Rev.*, **2012**, 41, 4335. [\[Crossref\]](#)
- [13] Lopes, P.; Katakya, R. *Anal. chem.* **2012**, 84, 229. [\[Crossref\]](#)
- [14] Busch, M. H.; Carles, L. B. et. al. *J. Chromatogr.* **1997**, 777, 311. [\[Crossref\]](#)
- [15] Juan, K.; Yuan L.; et.al. *Biochim. Biophys. Acta* **2004**, 1674, 205.
- [16] Ying, Li.; Wenying, He.; et.al. *Biochim. Biophys. Acta* **2005**, 1722, 15.
- [17] Purcell, M.; Malonga, H.; et.al. *Biochim. Biophys. Acta* **2001**, 1548, 129. [\[Crossref\]](#)
- [18] Khanna, S.; Islama, B.; et.al. *Eur. J. Pharm. Sci.* **2008**, 35, 371. [\[Crossref\]](#)
- [19] Bakkialakshmi, S.; Barani, V. *J. Pharm., Chem. Biol. Sci.* **2013**, 3, 559.
- [20] Pande, S.; Utale, P.; Tekade, P.; et.al. *Pharm. Chem. J.* **2014**, 48, 29. [\[Crossref\]](#)